Charge Transport in Single Molecular Junctions at the Solid/Liquid Interface

DATASET · MAY 2015

3 AUTHORS, INCLUDING:

Artem Mishchenko

The University of Manchester

61 PUBLICATIONS **2,361** CITATIONS

Charge Transport in Single Molecular Junctions at the Solid/Liquid Interface

Chen Li, Artem Mishchenko, and Thomas Wandlowski

Abstract Charge transport characteristics in metal–metal nanocontacts and single molecular junctions were studied at electrified solid–liquid interfaces employing a scanning tunneling microscope-based break junction technique, in combination with macroscopic electrochemical methods, in non-conducting solvents and in an electrochemical environment. We aim to demonstrate recent attempts in developing fundamental relationships between molecular structure, charge transport characteristics, and nanoscale electrochemical concepts. After an introduction and brief description of the experimental methodology, a case study on the electrical and mechanical properties of gold atomic contacts in aqueous electrolytes is presented. In experiments with alkanedithiol and α,ω-biphenyldithiol molecular junctions the role of sulfur–gold couplings and molecular conformation, such as gauche defects in alkyl chains and the torsion angle between two phenyl rings, are addressed. The combination with quantum chemistry calculations enabled a detailed molecular-level understanding of the electronic structure and transport characteristics of both systems. Employing the concept of "electrolyte gating" to $4,4'$-bipyridine and redox-active molecules, such as perylene bisimide derivatives, the construction of "active" symmetric and asymmetric molecular junctions with transistor- and diode-like behavior upon polarization in an electrochemical environment will be demonstrated. The latter experimental data could be represented quantitatively by the Kutznetsov/Ulstrup model, assuming a two-step electron transfer with partial vibration relaxation. Finally, we show that (individual) surface-immobilized gold clusters within the quantum-confined size range exhibit features of locally addressable multistate electronic switching upon electrolyte gating, which appears to be reminiscent of a sequential charging through several redox

C. Li, A. Mishchenko, and T. Wandlowski (✉)
Institute of Chemistry and Biochemistry, University of Berne, Freiestrasse 3,
3012 Berne, Switzerland
e-mail: chen.li@dcb.unibe.ch; artem.mishchenko@iac.unibe.ch; thomas.wandlowski@dcb.unibe.ch

states. The examples addressed here demonstrate the uniqueness and capabilities of
an electrochemical approach for the fundamental understanding and for potential
applications in nano- and molecular electronics.

Keywords Break junction · Charge transport · Electrolyte gate · Metal
nanocluster · Molecular junction · Scanning tunneling microscopy · Scanning
tunneling spectroscopy

Contents

1 Introduction

The idea of developing a single molecule-based electronics was first proposed by Aviram and Ratner [1], which is nowadays termed *Molecular Electronics* [2, 3]. The molecule-based approach bears several unique opportunities: (1) custom-design of nanoscale units, (2) self-organization and recognition properties of molecular building blocks, and (3) implementation of localized functions such rectification, switching or amplification [4–16]. The ability to measure and control charge transport through (single-) molecule junctions is of considerable fundamental interest, and represents a key step towards the development of a molecule-based electronics.

The following fundamental aspects represent some of the key challenges in attempts to understand charge transport in (single-) molecule junctions in more detail:

1. How does a metal electrode behave at an atomic scale?
2. How does one reliably "wire" a single molecule to macroscopic leads?
3. What role does the contact between an electrode and a molecule play?
4. What is the relation between molecular structure and charge transport characteristics, and what is the mechanism of charge transport in such configurations?
5. How could one control/tune electron transport through single molecules?

Molecular junctions represent model configurations, in which a voltage bias, as imposed by an outside source, triggers an electric current between two electrodes and a single embedded molecule, which reflects the electronic characteristics of the molecular junctions (Fig. 1).

Three challenges must be overcome to realize such a configuration: (1) fabrication of atomically sharp electrodes, (2) creation of a molecule-sized gap between the enclosed electrodes, and (3) a reliable embedding of the molecule into the gap. The former two were realized in various experimental approaches [17–23]. These
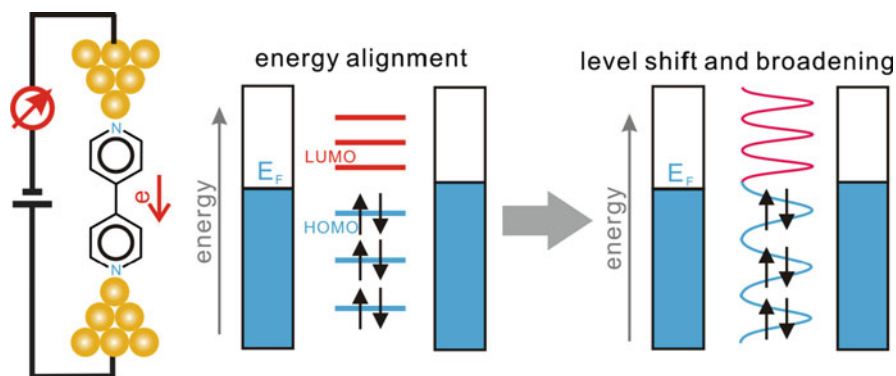

Fig. 1 Schematics of a typical "metal–molecule–metal" junction and energy level alignment

include scanning probe microscopies (SPM), scanning tunneling microscopy (STM) [24–27], conductive-probe atomic force microscopy (CP-AFM) [28–30], scanning tunneling spectroscopy (STS) [31–34]), nanoparticle (NP)-assisted junctions [35, 36], mechanical [37–41] and electromigration [42, 43] break junctions, crossed wires [44], nanopores [45], mercury drop electrodes [46], etc.

"Wiring" molecules to metal electrodes relies on the formation of specific chemical bonds. This is typically accomplished by modifying the core of the target molecules with "sticky" anchoring groups ("alligator clips" [47]) on both sides. In addition to the most prevalent thiol group (–SH), many other functional groups have been explored to establish a well-defined electronic coupling between molecular wires and metal contacts. These include amine (–NH$_2$) [48, 49], pyridine [32, 50, 51], isocyanide (–NC) [52], nitrile (–CN) [53, 54], isothiocyanate (–NCS) [55], selenol [56–58], carboxylic acid (–COOH) [59, 60], dimethyl phosphine (–P(CH$_3$)$_2$) [61], methyl sulfide (–SCH$_3$) [61], carbodithionate [62], *N,N'*-dimethyl amine [49], and fullerene [63] anchors. The different linker groups possess different coupling strengths and contact geometries, which affect considerably the charge transport characteristics of the various molecular junctions. For instance, covalent Au–S bonds exhibit strong geometry-dependent coupling properties [64, 65] while amine linkers were shown to prefer exclusively binding to undercoordinated gold atoms [66]. Complementary to the concept of covalent bonds, several groups recently demonstrated the formation of stable and conducting molecular junctions based on non-covalent intermolecular interactions. For example, Wu et al. for the first time verified the formation of an oligophenylene ethynylene (OPE) junction based on π–π interactions between adjacent molecular rods [67]. Chang et al. measured the tunneling conductance of hydrogen-bonded DNA bases [68].

Molecular wires, the "simplest" molecular targets, have attracted particularly high attention during the past decade. One may distinguish between two classes: (1) σ-bonded aliphatic molecules and (2) π-bonded aromatic molecules [9, 10]. α,ω-Alkanedithiols [28, 29, 64], oligophenylene vinylenes (OPV), and OPE rods [30, 35, 69] attached to gold electrodes or nanoclusters are prominent examples. Compared to the saturated aliphatic molecular wires, π-conjugated wires are more conducting. Experimental and theoretical studies have demonstrated that the conductances decrease exponentially with molecular length, indicating an electron tunneling model as the dominant electron transport mechanism. However, with increasing molecular length a transition from transport through tunneling to an activated ("hopping") mechanism was demonstrated. A recent example was published by Frisbie et al., who investigated π-conjugated molecular wires with a length of up to 7 nm [70]. Studies with substituted α,ω-alkane derivatives by Huggins [71], with various biphenyl and benzene derivatives by Venkataraman [72, 73], Haiss [74], and us [75, 76], as well as recent experiments reported by Tao on substituted tetraphenyl rods [77], clearly illustrated the huge potential of chemical control, e.g., the effect of electron-donating or -withdrawing substituents, molecular conformations, or anchoring groups on the conductance signature of single-molecule junctions at "solid/liquid" interfaces. However, there is still a

considerable lack in understanding the basic relationships between molecular structure and conductance properties.

Complementary to "passive" molecular wires, several groups carried out proof-of-concept experiments on "active" solid-state "metal–molecule–metal" junctions, for instance with redox centers under ex-situ (ambient) and ultra-high vacuum (UHV) cryogenic conditions. They discovered various phenomena mimicking fundamental functions of silicon-based electronics, such as rectification [78, 79], negative differential resistance (NDR) [45, 80, 81], amplification [41, 42], and switching and memory characteristics [16, 82–86]. The experimental investigations are currently accompanied by powerful theoretical and computational approaches to interpret molecular signatures in these transport junctions. The realization of these functions requires external stimuli (temperature, applied potential, light, magnetic field, etc.) to modulate charge transport in a controlled way [42, 87–89]. Additional challenges appear upon introduction of a gate, i.e., the extension of two-terminal molecular junctions into three-terminal configurations. Working in an electrochemical environment offers the particular opportunity of introducing the concept of "electrolyte gating" [90–93]. The electrochemical approach is unique, as the measured current represents both the electrical contact to the external circuit and the functional state of the wired molecules or nanoclusters.

In the following sections we shall present selected examples of our own recent work on charge transport with tailored molecules and clusters at *electrified* "solid/liquid" interfaces. We will introduce in Sect. 2 a scanning tunneling microscope-based break junction (STM-BJ) technique and the concept of "Electrochemical Gating." Case studies on the electrical and mechanical properties of gold atomic contacts in an electrochemical environment will be discussed in Sect. 3. Sections 4 and 5 will focus on charge transport studies with α,ω-alkanedithiols and biphenyl-type molecular wires in non-polar organic solvents. The role of orientation gating upon application of an electrochemical gate field will be discussed with 4,4′-bipyridine as an example in Sect. 6. In Sect. 7 we will focus on single redox-active molecular nanojunctions in an electrochemical environment, as illustrated by perylene bisimide-type molecules bound either to one (asymmetric configuration) or to two (symmetrical configuration) adjacent electrodes. These molecular studies will be complemented with an example of quantized double-layer charging of gold nanoparticles. The chapter will end with Conclusions and Outlook.

2 Methodology

Experimental approaches for investigating charge transport characteristics in "metal–molecule–metal" junctions should fulfil the following requirements: (1) providing robust and reproducible contacts between the bridged molecule(s) and the outside world, (2) identification of molecular signatures, and (3) access to tuning molecular electronic signatures by external stimuli under well-defined conditions.

In the following we will focus on three "molecular electronics test beds" as developed and employed for applications at electrified "solid/liquid" interfaces: (1) STM and STS, (2) assemblies based on horizontal nanogap electrodes, and (3) mechanically-controlled break junction experiments. For a more detailed description of the methods we refer to several excellent reviews published recently [16–22]. We will also address specific aspects of "electrolyte gating" and of data analysis.

2.1 Scanning Probe Microscope

The power of STM for measuring electronic properties of single molecules lies in the combination of high-resolution imaging (STM) and spatially resolved current-sensing spectroscopy (STS). The latter is capable of providing the local density of states (LDOS) with atomic spatial resolution [94]. In an asymmetric tunneling junction "metal tip–molecule–conducting substrate," the resulting "apparent height" images contain coupled information on both the electronic and topological properties (true height). As an example, a conjugated molecule may appear higher than a non-conjugated one of the same geometric dimensions. Experiments at cryogenic temperatures and under UHV demonstrated access to well-resolved signatures in the differential conductance and vibrational excitations [95, 96], and enabled a wide range of manipulations with single atoms and molecules [97]. Studies under ambient conditions require the immobilization of the target molecules. This is accomplished by either matrix-isolation experiments, where the "active" molecule is inserted into an inert matrix of alkanethiols [98–100], the formation of highly ordered self-assembled monolayers [31, 101–105] or the chemical anchoring of the "active" molecules onto appropriate substrates [106–108]. These studies provide access to exploring electrical phenomena such as NDR, dielectric break-down, switching and diode-like responses at room temperature, and in solution from monolayers down to the level of a few and even single molecules and clusters embedded in nanoscale tunneling junctions [34, 109, 110]. All three approaches have also been applied to electrochemical systems with target molecules immobilized at "solid/liquid" interfaces [111, 112].

Tao et al. [32] pioneered a technique based on the formation of single molecular junctions between the tip of an STM and a metal substrate. The method was adapted by other groups, modified and applied to a large number of molecular conductance studies at (electrified) "solid/liquid" interfaces [33, 113–119]. For details we refer to Sect. 2.3.

Frisbie et al. [120] and Lindsay et al. [28] introduced CP-AFM for conductance measurements in (single) molecular junctions. CP-AFM allows precise control of the AFM probe, employing the feedback of the force signal and the simultaneous acquisition of the molecular current response. In order to achieve a better electric contact between the conducting AFM tip and the target molecules of interest, Cui et al. proposed contacting bifunctionalized target molecules embedded in inert

alkanethiol-based matrices with metal nanoclusters. While the first attempt with cluster diameters ~1.5 nm led to artifacts due to Coulomb blockade, Lindsay et al. demonstrated later that larger gold nanoclusters (~4–5 nm diameter) provided direct access to clearly resolved molecular conductance signatures [121]. The cluster approach was also applied under electrochemical conditions [122]. In particular, Albrecht et al. resolved, for the first time, the intrinsic multistate switching of a single, monolayer-protected gold Au_{147} cluster through electrochemical gating [123].

2.2 Nanoscale Electrodes and Gaps

Conceptually perhaps the simplest method for wiring molecules in metallic junctions is the fabrication of constant-size metallic gaps with nanometer separation. The fabrication of electrodes with defined molecular-sized separation is technically challenging, but can be achieved by electron-beam lithography [124]. To trap molecules into the nanofabricated gap, as well as to tune gap dimensions, one uses electromigration [42], electrochemical dissolution or deposition strategies [125], molecular recognition and click-chemistry, employing acceptor-modified electrodes [126–128].

Due to the inherent size difference between nanofabricated gaps (>10 nm) and small organic molecules (~1 nm), many groups propose bridging these gaps by intermediate-size objects, such as carbon nanotubes [129, 130], nanoparticles [24, 35, 36, 131, 132], or oligomer strands [133]. For example, the Nuckolls group demonstrated how individual molecules can be trapped within a single-wall carbon nanotube, which was locally cut by oxidative etching [129, 130]. The nanotube itself is connected to two large nanofabricated metallic electrodes. Dadosh et al. have demonstrated that short dithiolates can connect with pairs of gold nanoparticles, giving rise to large particle–molecule–particle dumbbells, which could be successfully trapped and electrically addressed in larger gaps formed between two metallic leads [35].

2.3 Break Junction

The formation of molecule-sized gaps between electrodes embedding a few or even a single molecule comprises a major challenge. Gold appears to be one of the most suitable contact materials for application at electrified solid/liquid interfaces for several reasons: (1) it is malleable and ductile, (2) it forms covalent bonds with a large number of functional groups, (3) it could form atomically sharp contacts upon breaking a "simple" wire, and (4) it shows a rather large range of ideal polarizability in many electrolytes. Furthermore, using a piezoelectric transducer or other mechanical actuators (stepper motor, etc.) enables the formation of well-defined
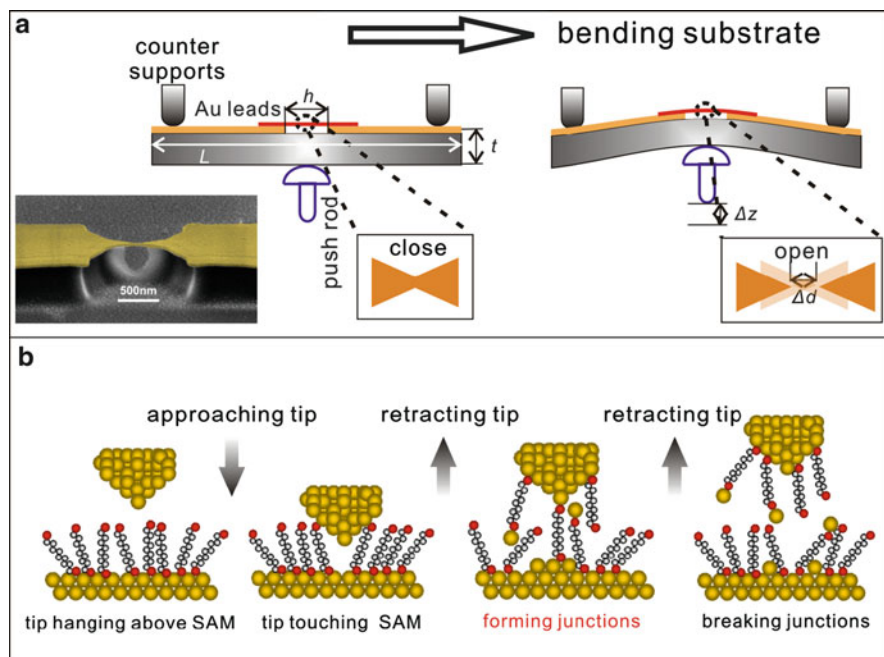
Fig. 2 (**a**) Schematic representation of a mechanically controlled break junction (MCBJ). The *inset* shows the SEM image of a nanofabricated gold bridge [40]. (**b**) Principle of an STM-based break junction experiment (STM-BJ)

gaps between two adjacent electrodes with high stability and sub-Ångstrom precision. These reasons led to the development of the so-called "break junction" techniques. We shall introduce next the two main types of break junction approaches: (1) mechanically controllable break junction (MCBJ) and (2) STM-based break junction (STM-BJ), (see Fig. 2).

2.3.1 Mechanically Controllable Break Junction

The basic working principle of an MCBJ is as follows. A flexible substrate is connected by two fixed beams on top and one pushing rod on the bottom. A mechanical actuator, such as a piezoelectric transducer or stepper motor, drives the pushing rod (moveable beam) to bend a substrate, leading to an elongation and subsequently the breaking of the metallic bridge on the substrate. The metallic bridge can be manually created by notching a metal wire [134], or by using micro-respective nanofabrication techniques [135] (see the inset of Fig. 2a). Applying a small bias voltage may lead to bridging the freshly created gap by bifunctional target molecules just after breaking of the metallic connection. Subsequently, (single) molecular junctions are formed. The reduction factor for the displacement

Δd of the notched wire or of a microfabricated metallic bridge with respect to the movement Δz of the pushing rod is $\Delta d/\Delta z = 1:100$ or $1:10^5$, respectively. This ensures a precise control of the gap width down to sub-nanometer dimensions, leading to a highly stable configuration.

The MCBJ technique was first introduced by Moreland et al. for studying the tunneling characteristics of Josephson junctions [136]. Müller et al. employed the approach to create metal quantum point contacts. These authors demonstrated in their studies conductance quantization phenomena [137]. The first (single) molecular junction employing an MCBJ set-up was reported by Reed et al., who measured the conductance of benzene-1,4-dithiol molecules (BDT) embedded between gold leads [37]. These authors used a BDT-coated gold wire before notching it under ambient conditions. Reichert et al. showed a superior stability of current–voltage characteristics measured with an MCBJ set-up under UHV conditions in a cryogenic environment [39]. Schönenberger et al. applied the MCBJ-approach to tunneling and conductance studies at solid/liquid interfaces [40, 138] and, rather recently, demonstrated a first application under electrochemical conditions [139].

2.3.2 Scanning Tunneling Microscopy Based Break Junction

Similar to the MCBJ technique, an STM configuration may also realize a break junction geometry. Different from the MCBJ, where two identical electrodes approach each other to form a *horizontal* molecular junction, the STM tip approaches and withdraws from the substrate in a vertical geometry. The STM-BJ was first applied to characterize electrical properties of metal nanocontacts [140]. Xu et al. extended the approach to form and to study single-molecule junctions [32]. The following sequence of steps was applied (see Fig. 2b). (1) The STM tip was driven to the initial position under feedback control by setting the appropriate tunneling conditions in a solution containing the target-molecule as solute. (2) Subsequently, the STM feedback was switched off, and the tip was moved by a piezoelectric transducer towards the adsorbate-modified substrate at constant x-y position, until a preset upper limit of the current (typically 1–20 μA for 0.1 V bias voltage) was reached. (3) After a short waiting time, long enough to form molecular junctions, the tip is pulled away from the substrate at a controlled rate. The current–distance curves are recorded while the tip is being retracted. The breaking of the previously formed molecular (single) junctions is indicated by abrupt steps following plateau-like regions of conductance.

In the present work, we applied two different strategies. (1) "Hard touch": the upper limit of the current is chosen to be higher than the quantum conductance. (i.e., the tip is gently driven into the substrate.) This strategy ensures "in situ" the fresh preparation of atomically-sharp electrodes before molecular junctions are being formed [32, 59, 76]. (2) "Gentle touch": this strategy avoids physical contact between tip and substrate, and thus keeps intact both the organic adlayer and the atomically flat substrate surface [33, 64].

Compared to the MCBJ, the STM-BJ has some unique advantages. (1) The STM-BJ facilitates a faster formation/breaking process, and gives access to a larger amount of data, thus yielding statistically more reliable data. (2) Due to the relative maturity of the STM technique, the approach can be directly applied to studies in solution [32], and even under electrochemical conditions [33, 34, 141]. (3) The STM configuration also enables the direct monitoring of the substrate surface before, during and after the transport measurements, leading to a superior structure control of the junctions. (4) The STM tip can be positioned precisely on the target area of an adsorbate-modified substrate, i.e., selectivity and flexibility in two dimensions (2D) during the measurements. A major drawback of the STM-BJ approach under ambient conditions and in solution is its limited stability as compared to the MCBJ approach.

Comparing the existing BJ techniques and their particular applications for studies at the solid/liquid interface, we emphasize the following concerns. (1) All technical realizations involve a fully "dynamic" process, in particular when comparing them to nano-fabricated chip assemblies. As a consequence, the lifetime of a molecular junction is often too short to be readily characterized by I–V measurement, local spectroscopy, and other structure-sensitive techniques. (2) The target molecules are always under tensile or compressive stress during the stretching process, which may lead to variations of the electronic properties of the respective molecular junctions. (3) When stretching the junctions, the microscopic geometry of the enclosing electrodes can vary from measurement to measurement, causing large variations of the interfacial geometric and electronic structure of the respective junctions.

2.3.3 Statistical Analysis

The formation and breaking of atomic contacts in BJ experiments is indicated by the existence of characteristic plateaus separated by steps in current–distance (i-Δz) traces with currents of the order of a few microamperes for typical bias voltages between 0.02 V and 0.30 V. In the case of molecular junctions one can observe additional plateaus and steps in the i-Δz traces, rather than a purely exponentially decaying tunneling current, or a sudden drop. However, they appear at significantly smaller currents, as compared to those in atomic metal contacts. The shape of individual traces varies considerably, due to variations in the structure of the nanojunctions, as well as because of mechanical instabilities of the assembly. The determination of most probable junction conductances, plateau lengths, stability, dynamics, etc., require the statistical analysis of a large number of individual curves recorded experimentally under a wide range of conditions, as well as their comparison with electronic structure and transport model calculations (simulations).

While initial attempts of quantification of i-Δz traces obtained in (single) molecule conductance studies suffered from rather poorly defined data selection strategies and limited current ranges [64, 116], most of the leading groups in the field focus now on the construction of all-data point conductance and plateau length

histograms from a large number of individual traces (often >1,000), recorded in a wide current range, to evaluate the most probable junction characteristics. Linear histograms are based on the splitting of individual experimental traces into many equal-current respective conductance intervals (bins) and counting the number of data points in each interval. The statistical analysis of a complete experiment is based on adding up a large number of single-curve histograms. The most frequently observed conductance values appear as characteristic peaks in the conductance histograms.

An alternative strategy is based on the all-data point analysis on a logarithmic scale [40, 48]. This approach is equivalent to the construction of a linear histogram with a logarithmically increasing bin width. This analysis has two advantages. (1) The logarithmic-scale representation enables the direct visualization of experimental data in a wide current range, from several hundreds of microamps down to a few picoamps, covering the range of breaking of metal–metal contacts down to the molecular junctions and down to the tunneling regime. (2) The logarithmic representation also enables a straightforward distinction between molecular junction-related features and background [40, 54].

Complementary strategies for the statistical analysis of the experimental traces are based on *plateau data-point* histograms, *plateau count* histograms, and *two-dimensional (2D) conductance–distance* histograms [54]. The first two methods lead to the identifications of the plateaus in the conductance traces. A plateau is defined as a series of consecutive data points limited by two "abrupt changes," allowing a certain scatter in the current, which are found by computing the first derivative of the respective single traces. The number of data-points of the identified plateaus is subsequently collected to build the plateau data-point conductance histogram. Alternatively, in the plateau-count histogram each selected plateau adds one count to the histogram.

The extension of the data analysis to 2D histograms provides correlations between three variables, such as conductance, plateau length, and their probabilities, and therefore may lead to a wealth of additional information, as compared to 1D histograms. However, this is currently not yet fully exploited. Two examples of 2D histograms are the 2D conductance–distance histogram and the 2D covariance conductance histogram [54].

The 2D conductance–distance histogram shows the logarithm of the experimentally obtained conductance in units of G_0 plotted vs distance [54, 63, 142]. The distance axis is normalized with respect to the atomic contact rupture, to align the experimental traces to a common point. Examples are $z = 0$ at $G = 0.7\ G_0$ [54]. Individual conductance–distance traces obtained in this manner are binned in 2D space (usually $1,000 \times 1,000$ bins), and then all individual 2D histograms are added together. The result represents statistically significant conductance–distance trends.

The covariance analysis was inspired by work of Halbritter et al. [143]. The covariance provides a measure of the strength of a correlation between different parts of the 1D logarithmic conductance histograms. In other words, the covariance analysis enables evaluating whether different parts of a histogram are correlated to

each other. The covariance is zero if the variations of counts in two different bins are independent. The covariance is positive if they are correlated, and negative if they are anti-correlated.

2.4 Electrolyte Gating

The addressing of nanoelectronic assemblies "metal–molecule (nanocluster)–metal" with device-like functions, such as rectifiers, switches, or transistors requires a source and a drain, and one or more localized electronic levels. The roles of source and drain (both as working electrodes WE1 and WE2) may be represented by the tip of an STM, combined with an appropriate substrate or, alternatively, a pair of nanoelectrodes; see Fig. 3.

Working in an electrochemical environment, such as an electrified solid/liquid interface, has the advantage that two potential differences can be controlled individually: the bias voltage, E_{bias}, between two working electrodes (WE1 and WE2) and the potential drop between each individual working electrode and the reference electrode (RE). The latter acts as an "electrochemical gate" and modulates the tunneling current between source (WE2) and drain (WE1) [144, 145]. The idea of an "electrochemical gate" to control charge transport in molecular electronics was introduced by Wrighton [90], Meulenkamp [91], Schönenberger [92], and McEuen [93], and further developed by Tao [31, 141, 146], Ulstrup et al. [144, 145, 147], Lindsay [113], Haiss et al. [33], Vanmaekelbergh [148], Mao [149], and us [34, 110, 150]. The effective "gate–molecule" distance is determined by the double layer thickness at the "electrode/electrolyte" interface, which is typically of the order of a few solvated ions. The "electrolyte gating" ensures a strong coupling, due to low contact resistances, thin adjacent double-layers (<1 nm) and the high mobility of the charge carriers (ions). The magnitude of the field in the electrochemical double layer (EDL) is close to the gate field required to modulate
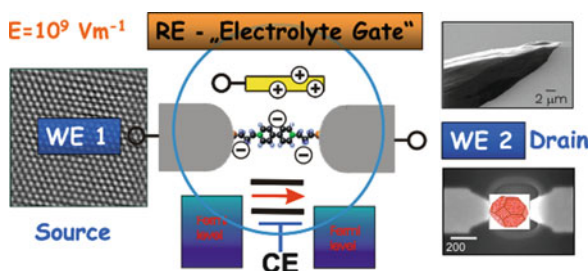
Fig. 3 Principle of "electrolyte gating." Tuning of the Fermi levels of WE1 and WE2 relative to the molecular levels enables measuring of current (i)–voltage (E) characteristics i vs ($E_{WE1}-E_{WE2}$) at fixed E_{WE1} or E_{WE2}, i vs E_{WE1} or E_{WE2} at fixed bias $E_{bias} = (E_{WE1}-E_{WE2})$ as well as barrier height profiles i vs distance z of tailored molecular junctions in a vertical SPM-based configuration respective horizontal nanoelectrode assembly

significantly the current through a molecule-sized nanostructure, according to first-principle calculation by di Ventra et al. [151, 152]. The electrochemical approach is powerful, as the measured current represents both electrical contact to the external circuit and the functional state of the nanostructures (single molecule, nanocluster).

Redox molecules are particularly interesting for an electrochemical approach, because they offer addressable (functional) energy states in an electrochemically accessible potential window, which can be tuned upon polarization between oxidized and reduced states. The difference in the junction conductance of the oxidized and the reduced forms of redox molecules may span several orders of magnitude. Examples of functional molecules used in these studies include porphyrins [31, 153], viologens [33, 34, 110, 114, 154, 155], aniline and thiophene oligomers [113, 146, 156, 157], metal–organic terpyridine complexes [46, 158–163], carotenes [164], nitro derivatives of OPE (OPV) [165, 166], ferrocene [150, 167, 168], perylene tetracarboxylic bisimide [141, 169, 170], tetrathia-fulvalenes [155], fullerene derivatives [171], redox-active proteins [109, 172–174], and hydroxyquinones [175].

Employing an electrochemical surface-science-based strategy provides direct access to explore the properties of "metal–metal" atomic contacts (i.e., electrodes) as well as functional molecules and/or nanocluster under conditions of a strongly coupled gate field. The approach offers unique opportunities to develop a nanoscale electrochemistry, and to contribute to the better understanding of the basic knowledge on gating inorganic–organic hybrid nanostructures upon polarization in a well-controlled environment.

3 Electron Transport Through Gold Atomic Contacts in an Electrochemical Environment

3.1 Introduction

Landauer proposed in 1957 the first mesoscopic theoretical approach to charge transport [176]. Transport is treated as a scattering problem, ignoring initially all inelastic interactions. Phase coherence is assumed to be preserved within the entire conductor. Transport properties, such as the electrical conductance, are intimately related to the transmission probability for an electron to cross the system. Landauer considered the current as a consequence of the injection of electrons at one end of a sample, and the probability of the electrons reaching the other end. The total conductance is determined by the sum of all current-carrying eigenmodes and their transmission probability, which leads to the Landauer formula of a 1D system:

$$G = \frac{2e^2}{h} \sum_{n=1}^{N} T_n,$$

(1)

where e is the electron charge, h is Plank's constant, and N is the number of channels with the transmission probability T_n.

In the case of a three-dimensional (3D) conductor, a more general formulation using a finite bias with a series of modes is given by

$$G = \frac{2e^2}{h} \sum_{i,j}^{N} T_{ij}, \tag{2}$$

where T_{ij} is the probability that an electron transmits from the ith mode of the left electrode to the jth mode at the right electrode. The quantum unit of the conductance G_0 is defined by

$$G_0 = \frac{2e^2}{h} \approx 77.5 \ \mu S \approx (12.9 \ k\Omega)^{-1}. \tag{3}$$

For an ideal conductor, no scattering occurs, and the transmission is given by $T = 1$. The quantum of conductance G_0 is obtained, indicating a maximum conductance. In other words, a perfect single-channel conductor between two electrodes has a finite, non-zero resistance. The exact interpretation of this result was provided by Imry [177], who associated the finite resistance with resistance arising at the interface between leads and the electrodes.

Systematic studies of I–V curves [178] and conductance histograms [134] of atomic contacts of different metals being characterized by different chemical valence states, supported by theoretical simulations [179], lead to the following discovery. The number of conducting channels of monatomic metal contacts is determined by the number of available valence orbitals [180]. In the case of gold, the conduction channel is only a single 6 s channel with an almost perfect transmission possibility. Thus, it possesses a total quantum conductance, which is quantized in units of G_0 (i.e., $G = N \cdot G_0$). These characteristics made gold an archetypal candidate to investigate properties of metal atomic contacts. Other s-metals such as Cu, Ag [181, 182], and the free electron metals Li, Na, K [183], exhibit a dominant conductance peak at 1 G_0, or slightly below that, in the respective conductance histograms. Metals like Al [184], Pb, Pt, Pd, Ir, Rh [185, 186], as well as magnetic metals, such as Fe, Co, Ni [187], do not have conductances with integer multiples of the quantum unit. For example, the first conductance peak for Nb was reported to be rather broad, in the range of 2.3–2.5 G_0 while Pt shows a pronounced feature at 1.6 G_0 in the conductance histogram.

The fabrication and characterization of atomic metal contacts have been based mainly on electro-deposition/dissolution [182] and break junction techniques (see review [134] and literatures cited therein). In particular, gold nanocontacts have been studied in great detail, due to the chemical inertness of the material, the malleability and ductility of gold. The processes of formation, evolution, and breaking of gold atomic contacts leads to step-like features in the current–distance curves [188, 189]. The abrupt changes in the current (conductance) response were

attributed to sudden alternations of the atomic arrangement (i.e., plastic deformation), while the plateaus were assigned to relatively stable atomic configurations (i.e., elastic deformation) [190–192]. The plateau regions, often characterized by integers of the quantum conductance unit G_0 (e.g., 1 G_0, 2 G_0 and 3 G_0), represent specific atomic configurations, which are currently interpreted as one, two or three atoms bridging the gap between the enclosing metal leads. Other parameters, such as plateau length and the scattering level, are determined by the mechanical properties of the respective atomic configurations. We also note that a certain variation in each individual conductance trace can be found, due to a rather poor control of the structural arrangement during the elongation of the contacts.

In addition to the study of bare (clean) metal atomic contacts, adsorbates were explored, due to the unique reactivity properties of nanoscale junctions [193]. For example, a large Au surface is known to be completely inert to H_2, while single gold contacts form a strong chemical bond with H_2 [194]. Current experimental (ex situ and in situ, e.g., in solution) and theoretical studies on adsorbates could be separated into three groups: (1) small and inert gaseous molecules; examples are H_2 [194–196], O_2 [197, 198], CO [199], and H_2O [200]; (2) organic molecules [192, 201, 202]; (3) inorganic anions [203]. Molecular species can interact rather *strongly* with atomic contacts, which may lead to dissociation and local reactions [204]. The incorporation of molecules into atomic contacts often enhances the stability of metal atomic configurations, and significantly decreases the transmission probability of electrons through contacts, causing the appearance of additional fractional conductance peaks at $G \ll G_0$ in the conductance histograms.

To date, most experiments with Au atomic contacts have been carried out at cryogenic temperatures or at room temperature in UHV, at ambient conditions in the gas phase, or in solution. Very few studies were reported in an electrochemical environment [205–208]. Electrochemical polarization offers the unique opportunity of *tuning* both the electrical and the mechanical properties of the respective atomic contacts by variation of the electrode potential. The electrodes could be "charged" and the *local* concentration of adsorbates at the atomic contacts can be varied in a rather controlled matter.

In the following we present an experimental study of gold atomic contacts formed in various aqueous electrolytes under electrochemical potential control. We will focus in particular on the electrical and mechanical properties of the electrochemical nanojunctions, as well as on their interplay in the presence/absence of various adsorbates (e.g., H_2, ClO_4^-, SO_4^{2-}, Cl^-, Br^-, and I^-) [209, 210].

3.2   Gold Atomic Contacts in 0.1 M H_2SO_4: A Case Study

3.2.1   Characterization of Au(111) in H_2SO_4 Solution

Figure 4 shows a typical cyclic voltammogram (CV) and the corresponding in situ STM images of an Au(111) electrode in 0.1 M H_2SO_4. The CV (red) as recorded in the bias range -0.35 V $< E_S <$ 1.35 V, reveals the characteristic oxidation peaks
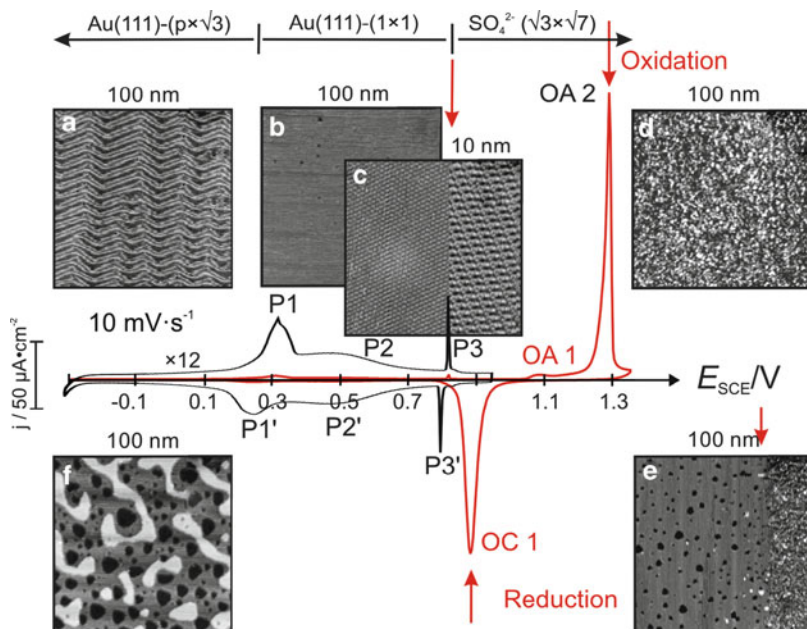
Fig. 4 Cyclic voltammograms (CV) of an Au(111) electrode in 0.05 M H_2SO_4 (*red*), scan rate 10 mV s^{-1}. The *black curve* represents the trace as recorded in the double layer region (current scale magnified by factor 12). The *red curve* extends the potential excursion into the surface oxidation/reduction potential region. The in situ STM images represent surface structures at different potentials: (**a**) thermally reconstructed Au(111)-(p × √3) surface, $E_S = -0.20$ V; (**b**) Au (111)-(1×1) surface after lifting of the reconstruction; (**c**) transition between a disordered and the ordered (√3 × √7)$R19.1^0$ sulfate adlayer; (**d**) oxidized gold surface; (**e**) reduction of the oxidized gold surface during a negative-going potential scan; (**f**) gold surface with monatomic deep holes obtained after ten successive ox/red cycles

OA1 and OA2, attributed to the oxidation of step and terrace sites, respectively, the corresponding reduction peak OC1, and the onset of hydrogen evolution at the most negative potentials. The black trace in Fig. 4 represents the double-layer region, with three pairs of peaks (note the change in the current scale!). The pair of peaks labeled P1/P1' corresponds to the lifting/formation of the Au(111)−(22 × √3) reconstruction, which is close to the potential of zero charge (PZC) [211]. Figure 4a shows an STM image of the thermally reconstructed Au(111)−(p × √3) surface with the characteristic zig-zag pattern. The broad peak P2/P2' marks the potential region of disordered SO_4^{2-} adsorption. Adsorbed anions are rather mobile in this region. Figure 4b represents the unreconstructed Au (111)−(1 × 1) surface. The reversible sharp peaks P3/P3' indicate the transition between the disordered and the ordered ((√3 × √7)$R19.1^0$) SO_4^{2-} overlayers, as illustrated in Fig. 4c [212, 213].

In consequence, we distinguish between the following characteristic potential regions: (1) hydrogen evolution at very negative potentials, (2) negatively charged gold surface with adsorbed, rather weakly hydrogen-bonded water [214], (3)

positively charged gold electrode with (hydrogen-) sulfate ions forming a disordered adlayer, (4) an ordered $((\sqrt{3} \times \sqrt{7})R19.1^0)$ adlayer at $E_S > P3$ until the onset of surface oxidation in region (5) at $E > OA1$.

3.2.2 Conductance of Gold Atomic Contacts at Various Potentials

Figure 5 shows representative 1D conductance histograms (upper panel) and the corresponding plateau length distributions (lower panel) for Au–Au nanocontacts formed at various electrode potentials in the double-layer region of Au(111) in 0.1 M H_2SO_4 solution. All histograms show characteristic conductance peaks at integer multiples of G_0 (1 G_0, 2 G_0, and 3 G_0). The following additional features were observed. (1) At the most negative potential (-0.35 V), where hydrogen evolution takes place, fractional conductance peaks evolve at 0.1 G_0, 0.5 G_0, and 1.5 G_0, respectively. (2) The fractional conductance peaks disappear with the onset of sulfate anion adsorption at the positively charged electrode. (3) The plateau length distributions appear to be narrower with higher potentials, where the nanoelectrodes bear positive charges.

The appearance of fractional conductance peaks at the negatively charged electrode are attributed to the presence of hydrogen molecules or atoms (see Sect. 3.2.3), as supported by a study of Csonka et al. [194, 195], and in agreement with recent observations reported by Kiguchi et al. [207]. The decreasing width of the plateau length distribution with more positive potentials, i.e., with the onset of

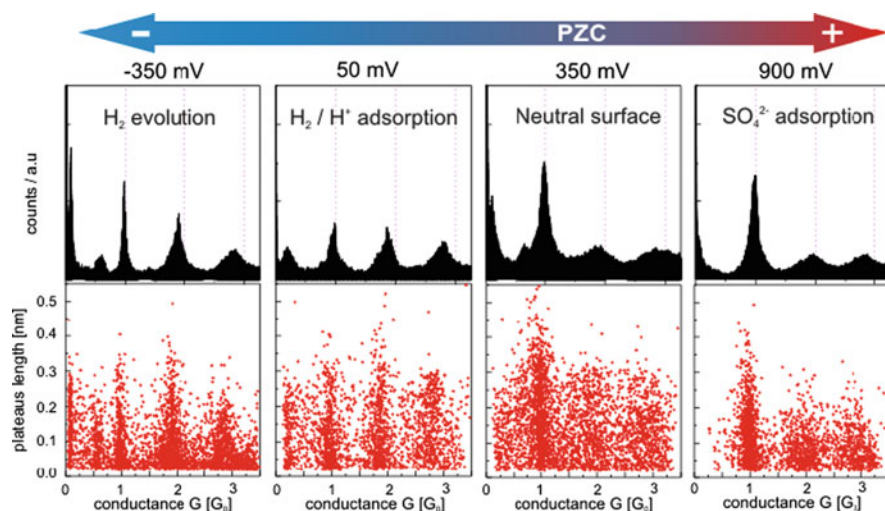**Fig. 5** All data-point conductance histograms (*upper panel*) of gold atomic contacts formed at various electrode potentials in 0.1 M H_2SO_4 solution. The histograms were built from 1,000 single curves without data selection. The corresponding plateau distributions are plotted in the *lower panel*. All measurements were carried out with a bias voltage of 0.10 V. The tip moving rate was 60 nm s^{-1}

sulfate ion adsorption (Fig. 5), is interpreted as an adsorbate-induced stabilization of certain atomic configurations [192, 201, 202, 215].

The exponential tail in the conductance histograms in regions $\ll G_o$ is attributed to an adsorbate-induced decrease in the adhesive interactions between Au atoms, and prevents the occurrence of a "jump-out-of-contact" characteristics. Similar observations were also reported under UHV conditions [195] and in air [216].

3.2.3 Effect of H_2 on Gold Atomic Contacts

Figure 6a illustrates conductance histograms recorded at $E = E_{pzc} - 0.30$ V at various solution pH values. These experiments demonstrate that the fractional conductance is sensitive to the concentration of hydronium ions or hydrogen in
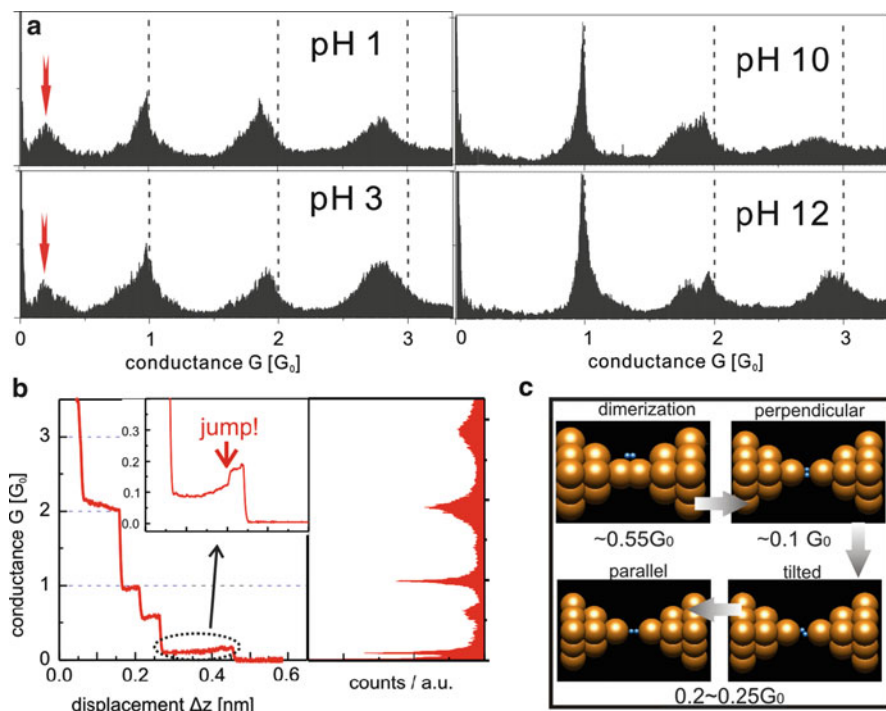
Fig. 6 (**a**) Conductance histograms obtained at a negatively charged electrode surface, in particular at $E = 0.050$ V (vs SCE) at various pH values: pH 1: 0.1 M H_2SO_4; pH 3: 0.1 M K_2SO_4 + 1 mM H_2SO_4; pH 10: 0.1 M K_2SO_4 + 1 mM KOH; pH 12: 0.1 M K_2SO_4 + 0.01 M KOH. The pronounced fractional peaks are marked by *red arrows*. (**b**) A typical single-conductance trace with fractional G_0 conductance plateaus and the respective histogram. The *inset* shows an enlarged trace in the low conductance region. (**c**) Schematic representation displaying the various types of H_2-incorporation into Au–Au atomic contacts [209]

either atomic or molecular forms, i.e., it is modulated chemically and not by the surface charge state.

Figure 6b shows a representative single-conductance trace, as well as the respective histograms. They exhibit well-developed plateaus at 0.1 G_0 and 0.5 G_0. The careful inspection of the low-conductance plateaus around 0.1 G_0 (see inset in Fig. 6b) reveals small jumps from ~0.1 G_0 to ~0.2 G_0, just before the conductance drops to values close to zero.

In an attempt to interpret these observations we refer to a recent ab initio density function theory (DFT) study by Barnett et al. [217]. These authors demonstrated that H_2 molecules form rather stable bridging structures with Au atomic contacts. They also report that a configuration of the H_2 molecules, with the H–H axis perpendicular to the axis of the contacting gold, leads to a conductance of ~0.1 G_0, while the conductances of tilted or parallel H_2 assemblies yield higher values, ranging between 0.20 and 0.25 G_0. We hypothesize that the breaking of Au–Au atomic contacts in the hydrogen evolution region of an electrochemical system might lead to a similar scenario, e.g., the relative positions of H_2 and gold leads are changing from a perpendicular one, via a tilted one, to a parallel one, just before the Au–Au nanocontacts breaks. Our tentative interpretation is supported by Au–Au pulling curves under cryogenic conditions [194].

The conductance peak near half-multiples of G_0 was found under both cryogenic [194, 195] and electrochemical [205, 207] conditions. Theoretical studies revealed that stretched single atomic chains have a strong tendency to form dimers spontaneously [218, 219]. DFT-based calculations suggest that the dimerization-induced conductances range from 0.58 G_0 [220] to 0.4 G_0 [218]. Adopting this result to our experimental observations, and supported by a recent work of Jelinek et al. [204], we suggest that the plateaus around 0.5 G_0 represent H_2-*assisted* dimerized gold atomic contacts (see Fig. 6c).

In consequence, the following scenario is suggested (c.f. Fig. 6c). During the elongation of an atomic contact, an H_2 molecule (which is electrochemically generated at the leads at potentials under consideration) couples weakly with gold atoms in the constriction region, assisting the formation of an Au dimer, which leads to a junction conductance of 0.5 G_0. Further stretching of the contact is followed by the incorporation of H_2 into the contact, initially in a perpendicular and subsequently into a parallel relative orientation of molecular and nanocontact axis, as represented by the small jump in the 0.1 G_0 plateau just before the contact breaks [209].

3.2.4 Statistical Analysis of the Plateau Lengths

The mechanical properties of Au atomic contacts were investigated by analyzing plateau lengths histograms. Figure 7a illustrates the most probable plateau lengths, obtained in a series of experiments with a stretching rate of 40 nm s^{-1}, as a function of the applied electrochemical potential for the first conductance peak developed in the interval between 0.75 G_0 and 1.25 G_0. The graph reveals a distinct maximum,
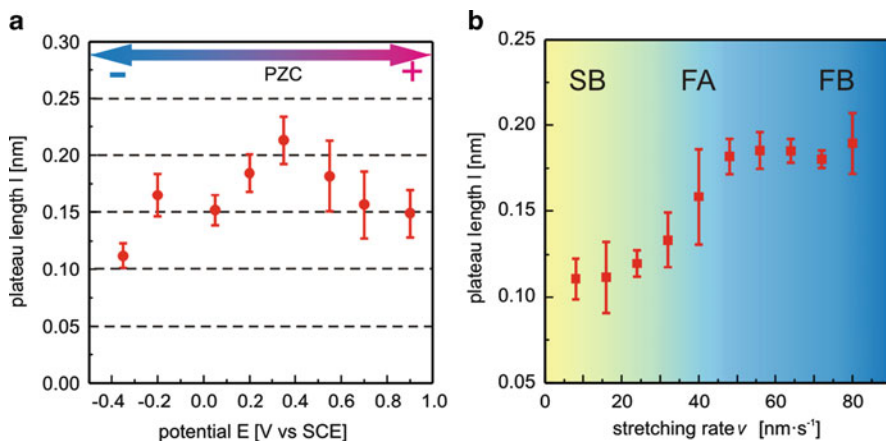
Fig. 7 (**a**) Plateau length of the first Au–Au nanocontact conductance peak (developed between 0.75 G_0 and 1.25 G_0) in function of the electrode potential in 0.1 M H_2SO_4, stretching rate $v = 40$ nm s^{-1}. (**b**) Dependence of the plateau length l of Au atomic contacts on the stretching rate v recorded at $E_S = -0.200$ V (vs SCE). Three characteristic regions are indicated as *SB*, *FA*, and *FB* (see text for more details)

in the vicinity of the PZC $E_{pzc} = 0.25$ V, on the Au(111) electrode under the current experimental conditions, which correlates with the position of the maximum in surface energy [221].

Every atom of the nanocontact constriction represents an active "surface" atom. The tensile force in the plateau region increases upon stretching atomic contacts elastically [188, 189]. The rupture of the gold monatomic contact takes place when the applied tensile force reaches a critical value, sufficient to break a single Au–Au bond. As a consequence, the atomic contact with the most "sticky" atoms at the E_{pzc} is the most difficult one to be break. The stronger adhesion eventually requires a larger load, which seems to be reflected in a longer stretching distance until the contact breaks. This interpretation is supported by the observation, that the plateau length of Au–Au atomic contacts before breaking is longer in the presence of weakly adsorbed ClO_4^- ions, as compared to the much stronger adsorbed SO_4^{2-} ions. The latter enhance the mobility (i.e., weaken adhesion) of surface Au atoms.

We extracted the dependence of the plateau length on the stretching rate in an attempt to explore the mechanical properties of Au–Au nanocontacts under electrochemical conditions. Figure 7b illustrates a typical example, obtained for the main conductance peak around 1 G_0 at $E_S = -0.200$ V. One may distinguish between three regions. At low stretching rates ($v < 16$ nm s^{-1}) the plateau length maintains a constant value of ~0.12 nm. At stretching rates higher than $v \sim 48$ nm s^{-1} the plateau length reaches a maximum of ~0.18 nm and remains rather constant. In the intermediate regions a monotonic increase of the plateau length with the stretching rate is observed. These observations illustrate that the Au–Au bond breaking process depends on the applied stretching rate.

In this context we note those force-dependent experiments with biological molecules [222–226] and the very few case studies reported for non-biological

systems [224, 227, 228] demonstrate that bond rupture forces depend on the applied load. Specifically, barriers in the energy landscape are lowered, and bond lifetimes are shortened under external force. Evans et al. [229, 230] developed a thermodynamic model of the bond-breaking process. The theory predicts the spontaneous dissociation of a chemical bond in the absence of external forces, due to thermal fluctuations (spontaneous breakdown). At faster stretching rates the external force increases quickly enough to lower the dissociation energy barrier E_b before spontaneous breakdown takes place. In this regime, the breakdown force is finite and increases linearly with the logarithm of the force loading rate [229]. Finally, at very fast stretching rates the external force lowers E_b to zero, and a maximum of the breakdown force is reached, which leads to the adiabatic regime.

This approach is adopted to discuss the load-dependence of breaking Au–Au nanocontacts at different stretching rates (Fig. 7b). We benefited from a discovery of Tao et al. [227, 228], who found that the external force is linearly proportional to the plateau length. Thus, the breaking force and the loading rate of force can be replaced by plateau length and stretching rate. Considering the analogy between force and stretching rate in the current experiment, we assign the regions at low ($v < 16$ nm s^{-1}) stretching rate to a self-breaking (SB) regime, the intermediate (16 nm s$^{-1} < v < 48$ nm s^{-1}) stretching rate to a force-assisting (FA) regime, and the high ($v > 48$ nm s^{-1}) stretching rate to a force-breaking (FB) regime [231]. The three regimes observed are also consistent with the theoretical simulations by Leiva et al. [232] and Liu et al. [233].

3.3 Role of Anion Adsorption on Gold Atomic Contacts

3.3.1 Electrochemical Characterization

The adsorption strength of anions on Au electrodes follows the sequence of ClO_4^- < SO_4^{2-} < Cl^- < Br^- < I^-. The strong specific adsorption of halide ions leads to a partial charge transfer between the adsorbate and the metal electrode [234].

The CVs of Au(111) in 0.1 M HClO$_4$, 0.1 M H$_2$SO$_4$, 0.1 M HClO$_4$ + 1 mM KCl, 0.1 M HClO$_4$ + 1 mM KBr, and 0.1 M HClO$_4$ + 1 mM KI are displayed in Fig. 8. All curves, except that for 0.1 M HClO$_4$,, exhibit common features. However, they are located in different potential regions. The most prominent peaks reveal the lifting/formation of reconstruction of the Au(111) surface, coinciding approximately with the respective potentials of zero charge E_{pzc}, followed by a potential region of disordered (mobile) anion adsorption. At the most positive potentials displayed, various ordered overlayers of the specifically adsorbed anions are formed (for a detailed review we refer to [235]). In addition, we would like to emphasize two trends: (1) the potentials of zero charge shift with increasing strength of specific adsorption towards more negative values ($I^- < Br^- < Cl^- < SO_4^{2-} < ClO_4^-$) [234] and (2) the regions of disordered anion adsorption shrink with increasing adsorption strength.

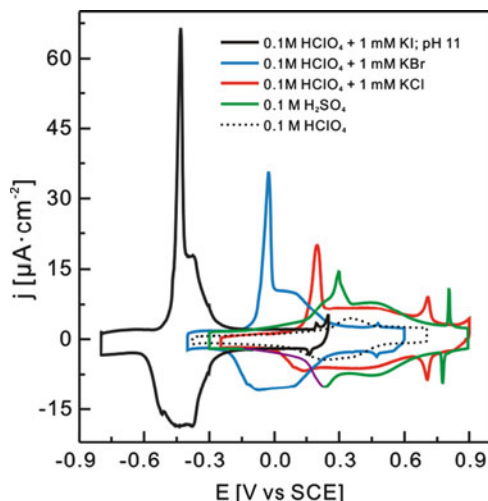**Fig. 8** Cyclic voltammograms of Au(111) in 0.1 M HClO$_4$ (*dotted line*), 0.1 M H$_2$SO$_4$ (*green*), 0.1 M HClO$_4$ + 1 mM KCl (*red*), 0.1 M HClO$_4$ + 1 mM KBr (*blue*), and 0.1 M HClO$_4$ + 1 mM KI (*black*) in the double layer region. Scan rate 50 mV s^{-1}

3.3.2 Single Conductance Traces and Conductance Histograms

Figure 9a displays selected conductance–distance traces and Fig. 9b, c the corresponding conductance histograms of Au atomic contacts formed in the presence of SO$_4^{2-}$ and Cl$^-$ ions at various potentials.

At negative potentials and charge densities, i.e., in the absence of specific anion adsorption, all conductance histograms display distinct maxima, reflecting the well-developed, flat, and long steps at integer multiples of G_0 in the individual conductance–distance traces. Examples are displayed in Fig. 9a as *curves A*. Conductance histograms constructed in the potential regions of the ordered sulfate and halide ion adlayers also exhibit pronounced peaks. However, one observes that the corresponding single traces exhibit rather unstable and fluctuating plateaus (*curves B* in Fig. 9a). In potential regions of the disordered anion adsorption we found mostly individual conductance–distance traces, with rather abrupt steps resulting in a completely broken junction (*curves C* in Fig. 9a). The temporarily created atomic junctions appear to be very fragile, which does not allow a "step-by-step" evolution during the elongation of contacts. This leads to a rather small data base for the quantitative analysis, as reflected in the low number of counts in the histograms at potentials of disordered anion adsorption.

These experimental results demonstrate that the specific adsorption of anions leads to a significant decrease in junction stability, as illustrated in particular in the potential regions of disordered anion adsorption, as well as in the fluctuations in the plateau currents at potentials of the 2D-ordered anion adlayers. The instability of the conductance plateaus were statistically analyzed, by determining the standard
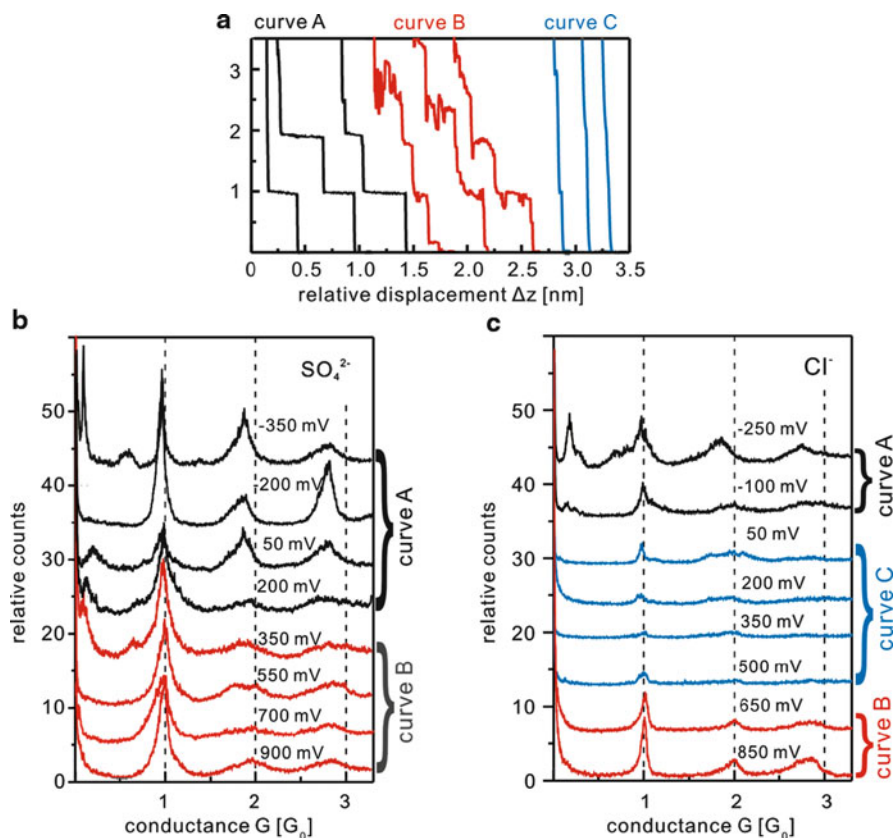
Fig. 9 (**a**) Three types of single conductance traces for Au atomic contacts as observed in the presence of specifically adsorbed anions characterized by well-developed plateaus (*curves A*), noisy plateaus (*curves B*), and abrupt steps with no plateaus (*curves C*), respectively. The stretching rate was 60 nm s^{-1}, and bias voltage applied was 0.100 V. (**b,c**) All data-point conductance histograms at various electrode potentials in the presence of specifically adsorbed SO_4^{2-} (**b**) and Cl^- (**c**), respectively

deviations of the plateau currents in individual traces, and subsequently summing over all families of plateaus, as recorded for a large number of individual traces. The standard deviation basically reflects the population of data points of a specific plateau, and thus provides information on the noise level of the respective plateau.

Figure 10 shows a 2D plot of the plateau position vs scattering level, as constructed from 1,000 single traces at various potentials in the double-layer region for Au atomic contacts in 0.1 M H_2SO_4. The scattering levels ($\pm 0.075\ G_0$) of plateaus formed at a positively-charged surface are larger, approximately by a factor of 3, as compared to those at a negatively charged electrode ($\pm 0.025\ G_0$). This result correlates with the shape of the families of conductance–distance traces displayed in Fig. 9a as *curves A* and *curves B*, respectively. The trend is more pronounced for the more strongly specifically adsorbed halide ions. The strong
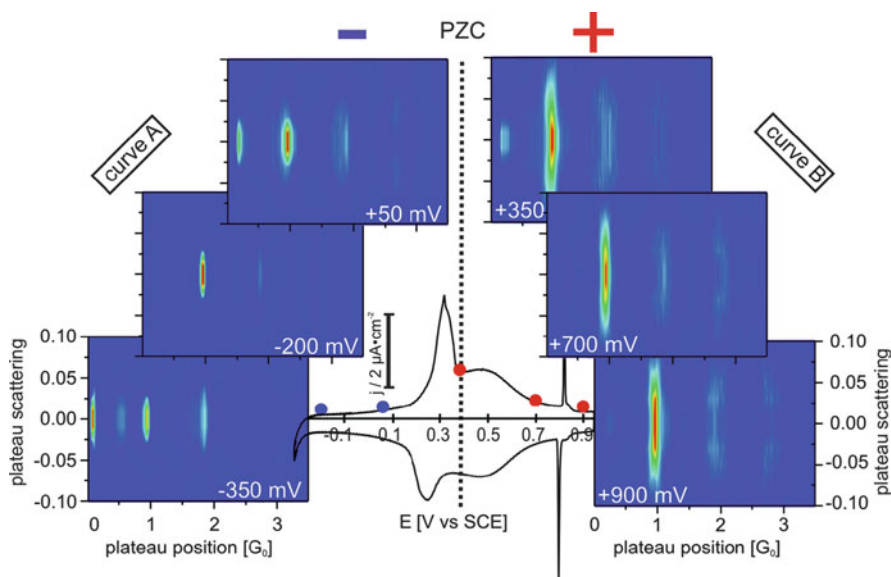
Fig. 10 Two-dimensional (2D) histograms (plateau scattering vs position) at various electrode potentials for Au(111) in 0.1 M H_2SO_4. The statistical analysis is based on 2D bins

binding between adsorbates and Au atoms weakens the bonds between metal atoms. These observations in the presence of specifically adsorbed anions are in agreement with results on the dynamics of metal surfaces, such as step fluctuations and island mobility [192, 201, 215]. In contrast, the generation and adsorption of H_2 at a negatively charged gold surface stabilizes the created Au–Au nanocontacts.

3.3.3 Shift of the 1 G_0 Conductance Peak

A closer inspection of the predominant peak in the conductance histogram at ~ G_0 (=77.5 μS) reveals that its position and magnitude depend on the applied electrode potential, as well as on the strength of anion adsorption (Fig. 11). The peak position shifts in the presence of weakly specifically adsorbed ions (e.g., ClO_4^-, SO_4^{2-}) to value smaller than G_0.

The down-shift of the 1 G_0 peak in the conductance histogram has been observed experimentally and theoretically [236, 237]. In addition, the above study revealed that the down-shifts are larger for higher-order conductance peaks. The down-shift observed for the 1 G_0 peak of the Au atomic contacts cover a range between 100 and 500 Ω. Theoretical model studies suggest that this downshift could be attributed to impurities or lattice defects, disorder or boundary corrugations, which generate backscattering in the atomic contact region [238, 239].
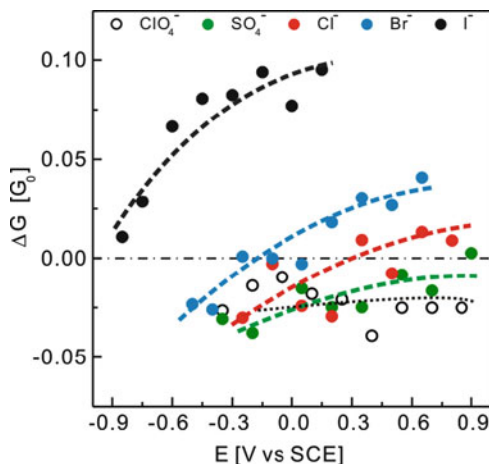
Fig. 11 Dependence of $\Delta G_0 = G_P - G_0$ on the electrode potential upon adsorption of different anions. G_P is defined by a Gaussian fit to the conductance peak closest to G_0 in the respective conductance histograms

In the presence of specifically adsorbed ions, e.g., for halides at potentials $E > E_{pzc}$, the trend changes and the position of the 1 G_0 peaks shifts to higher values than the quantum conductance unit. The up-shifts follow the order of adsorption strength, $Cl^- < Br^- < I^-$.

We note that the measured conductances are the total conductance, which is determined by the number of conducting channels and the transmission probability of the respective channels. The number of channels of monatomic contacts is determined by the number of available valence orbitals [180]. The transmissions of these channels vary from zero to one, and are affected by the atomic configuration and the state of strain [240]. The strong adsorption of halides on the gold surface shows a partially covalent character, which increases in the order $Cl^- < Br^- < I^-$. The mixture (hybridization) of electronic states of absorbed anions and metal atoms may lead to a non-negligible alteration in the electronic state and atomic structures. In other words, the number of conductance channels contributing to the experimentally measured signal might increase upon specific anion adsorption.

The enhancement of the ballistic transmission through atomic wires upon strong chemical adsorption is supported by ab initio DFT-based calculations [220], and was also observed in the presence of molecular adsorbates [201].

4 Charge Transport in "Au–α,ω-Alkanedithiol–Au" Junctions

"Au–α,ω-alkanedithiol–Au" junctions represent one of the simplest molecular junctions which have been studied since 1971 [241]. These alkanedithiol-based junctions were developed as a model system and test bed for various experimental approaches, as well as for theoretical studies for exploring fundamental concepts of charge transport in molecular junctions.

4.1 Introduction

Alkane(di)thiols possess a large energy gap between the HOMO and LUMO of about 7–8 eV and strongly localized σ-orbitals. Thus, these molecules are considered as insulators, and, consequently, the tunneling current is expected to decrease exponentially with increasing molecule length and to be temperature-independent.

Charge transport properties of alkane(di)thiol-based molecular junctions have been extensively studied, employing various techniques (c.f. reviews in [9, 10, 20, 23]). Most transport experiments were carried out under ambient conditions in air and/or in non-polar organic solvents. 1,8-Octanedithiol (ODT) embedded between two gold leads developed as a particularly well-studied system, employing a wide range of experimental techniques. Single-molecule conductance data of ODT have been obtained from STM-BJ experiments in the groups of Tao [32, 59, 242], Venkataraman [61, 116], Haiss [243–245], Fujihira [115], Segalman [117], Chen [55], and us [64, 114], by CP-AFM in the groups of Lindsay [28, 171, 246, 247], Frisbie [29, 248, 249], Xu [250], and Scoles [251], and by MCBJ in the groups of Schoenenberger [40, 252] and Ruitenbeek [253]. Dropping mercury electrode [254, 255], nanopores [256], and crossed wire assemblies [257] have also been used to measure the conductance of alkane(di)thiol molecular junctions composed of a few or a larger number of contacted target molecules.

Apart from the more conventional transport measurements of molecular junctions at constant bias voltage, alkane(di)thiols-based molecular junctions were also characterized by transition voltage spectroscopy [258, 259], AC voltage modulation [260], and inelastic electron tunneling spectroscopies [261].

The conductance values of ODT single-molecular junctions can be categorized in three distinctly different families around $2.5 \times 10^{-4} \, G_0$ (~20 nS), $0.5 \times 10^{-4} \, G_0$ (~4 nS), and $0.1 \times 10^{-4} \, G_0$ (~1 nS). The mid-conductance value was reported by almost all research groups, while the high and the low values were strongly dependent on the chosen experimental conditions, as well as on strategies of data analysis [19, 242, 245, 252]. Systematic studies on the distance respective molecular length dependence have led to decay parameters β_N ranging between 0.5 and 1.2 [9, 10, 28, 32, 40, 64, 242, 244].

The nature of the conductance families reported for single alkanedithiol junctions is still under debate. Current interpretations are based on different contact geometries [64, 115, 242], different molecular conformations [64, 244], substrate roughness [245], or the control of tip movement [252].

The discrepancies in the reported conductance data of "Au–alkanedithiol–Au" junctions attracted our attention, and we decided to carry out an in-depth experimental study of the charge transport properties of "Au–α,ω-alkanedithiol–Au" molecule junctions in a non-conducting solvent. The combination with quantum chemistry ab initio simulations yielded a detailed view of this archetype of molecular junctions, and helped to resolve the puzzle on the role of microscopic geometries at the contacts and in the molecular conformation.

4.2 Single-Molecule Conductance Measurements

Charge transport characteristics in "gold–alkanedithiol–gold" junctions were recorded with an STM-based contact junction approach ("gentle touch") with 0.1 mM of the respective alkanedithiol in 1,3,5-trimethylbenzene [64]. The i-Δz retraction curves were either exponentially decaying (50%), noisy (10%), or showed characteristic plateaus with a typical length of 0.04–0.15 nm, separated by abrupt steps (40%). Figure 12 illustrates a set of representative i-Δz curves of the latter type for the breaking of nonanedithiol (NDT) junctions. The observed currents are three to four orders of magnitude smaller as compared to metal nanocontacts. These conductance steps are ascribed to the breaking of individual respective multi-molecule junctions formed between the gold STM tip and the substrate. Control experiments in the absence of NDT displayed almost exclusively (98%) exponentially decaying traces.

The statistical analysis of the plateau current yields histograms with characteristic peaks (Fig. 13). The careful analysis of these current peaks allows the identification of three distinctly different sequences of equally spaced maxima, which are attributed to low (L), medium (M), and high (H) conductance molecular junctions. The current within each series scales approximately linearly with the number of peaks. The peak of each sequence is attributed to a *single* molecular junction. The corresponding currents also depend linearly on the applied bias voltage up to $\pm$ 0.2 V (see insets in Fig. 13a, b). By fitting the current maxima with a Gaussian function, the following conductance values of the three specific single-molecule "Au-NDT-Au" junctions were obtained: 0.47 $\pm$ 0.03 nS (L), 2.0 $\pm$ 0.2 nS (M) and 9.9 $\pm$ 0.9 nS (H).
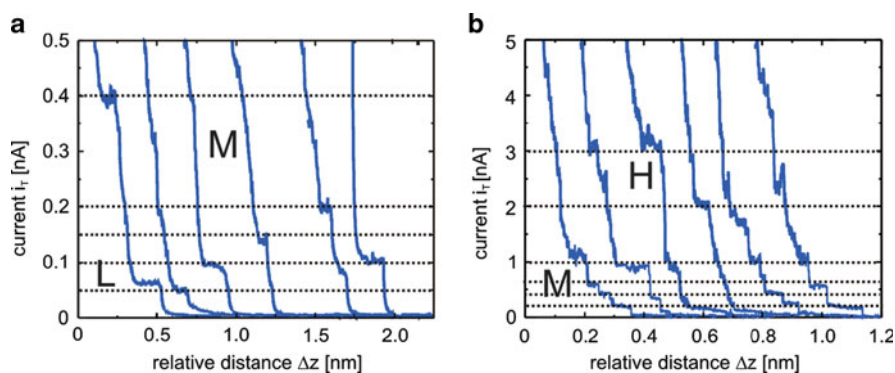
Fig. 12 (**a**) Current–distance retraction traces recorded with a gold STM tip for 1 mM 1,9-nonanedithiol in 1,3,5-trimethylbenzene on Au(111)-(1 × 1), at E_{bias} = 0.10 V. The setpoint current before disabling the feedback was chosen at i_0 = 0.1 nA. The retraction rate was 4 nm s^{-1}. (**b**) Same conditions as in (**a**), except that the preamplifier limit was chosen at 10 nA. The *dotted lines* represent characteristic regions of the low, mid, and high conductances

Fig. 13 Plateau count conductance histograms constructed from the plateaus found in the step-like conductance–distance traces for Au–1,9-nonanedithiol–Au junctions. (**a**) 1,600 selected out of 4,300 traces employing a 1 nA (max) preamplifier; (**b**) 1,100 selected out of 4,300 traces recorded with th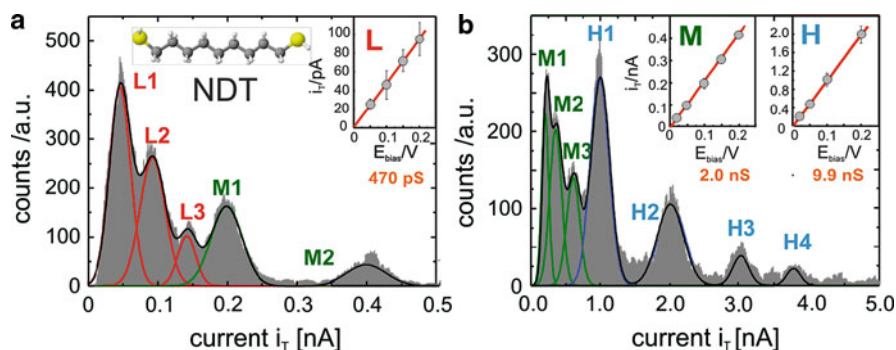e 10 nA (max) preamplifier. All other conditions are identical to those in Fig. 12. The *insets* in (**a**) and (**b**) show that the currents within each series scale approximately linearly with the number of peaks [64]

Table 1 Summary of the conductance values of Au–α,ω-alkanedithiols–Au molecular junctions recorded in 1,3,5-trimethylbenzene [64]

α,ω-Alkanedithiol	Conductance values (nS)		
	L	M	H
PDT ($N = 5$)	1.9 ± 0.05	64 ± 5	–
HDT ($N = 6$)	2.45 ± 0.06	20 ± 2	95 ± 10
ODT ($N = 8$)	0.89 ± 0.08	4.4 ± 0.4	21 ± 2
NDT ($N = 9$)	0.47 ± 0.03	2.0 ± 0.2	9.9 ± 0.9
DDT ($N = 10$)	0.22 ± 0.02	0.45 ± 0.04	1.68 ± 0.03

Following the same experimental protocol and analysis strategy, multiple sets of conductance values for 1,5-pentanedithiol (PDT), 1,6-hexanedithiol (HDT), 1,8-octanedithiol (ODT), and 1,10-decanedithiol (DDT) were measured. The results are summarized in Table 1. Inspection of the data reveals that the high-conductance values (H) are approximately five times larger than the medium-conductance values (M), while the low values (L) do not scale with a constant ratio with respect to the M or L data sets.

The H, M, and L values obtained in the present work are in good agreement with data reported in the literature [9, 23, 32, 40, 117, 242, 243]. However, none of the previous contributions reported all three sets of conductance values simultaneously, i.e., as derived from a single set of experiments. Several groups attempted to discuss this situation. For example, Haiss et al. pointed out recently, based on a case study with ODT, that surface roughness of the substrate, as well as the approach regime, have a pronounced effect on the accessibility of certain families of single molecule conductances [245]. Gonzalez et al. put forward an interpretation based on multimolecular junctions in certain most probable microscopic arrangements of lead-molecule contact geometries [252].
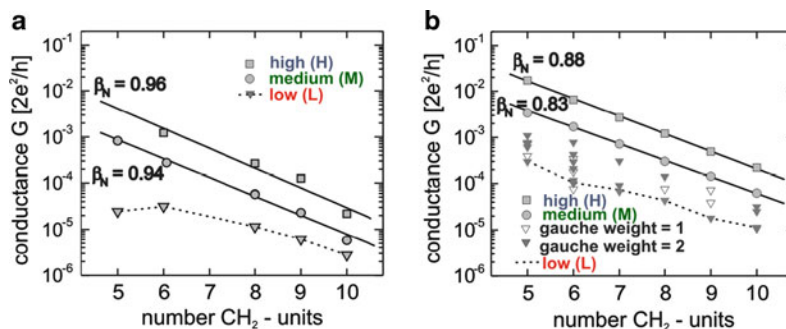
Fig. 14 Experimental (**a**) and calculated (**b**) conductance values of Au–*n*-alkanedithiol–Au junctions vs number *n* of methylene units in a semilogarithmic representation. The three sets of conductance values – high (H), medium (M), and low (L) – are shown as *squares*, *circles*, and *triangles*. The *straight lines* were obtained from a linear regression analysis with decay constants β_N defined per methylene (CH_2) unit. The conductances of many different, nonequivalent gauche isomers cover the window below the medium values in (**b**) [64]

Figure 14 shows the semi-logarithmic plots of the various single junction conductances vs molecular length (Fig. 14a – experimental data; Fig. 14b – calculated conductances). The length is expressed as the number of CH_2 units. The H and M conductance values follow a simple tunneling model given by $G = G_C \exp(-\beta_N N)$ with decay constants β_N of 0.96 ± 0.15 for H and 0.94 ± 0.05 for M. These values of β_N are in a good agreement with the literature on single junctions "Au–alkanedithiol–Au" data [32, 118], as well as the electron transfer through compact and aligned monolayers of alkanethiols using nanopores [262], mercury contacts [254, 263, 264], CP-AFM [247], or redox probes [265, 266].

On the other hand, the low-conductance values (L) give a poor linear correlation of the molecular length with an approximate decay constant $\beta_N \sim 0.45 \pm 0.09$, distinctively different from the H and M sequences. The estimated value of $\beta_N(L)$ is rather close to results reported by Cui [28] and Haiss [243]. Haiss et al. [244] found a pronounced temperature dependence of these L values, which scales logarithmically with T^{-1} in the temperature range 293–353 K, indicating a transport mechanism different from a simple tunneling model.

4.3 Interpretation of Multiple Conduction States

To provide further insight into the nature of multiple conduction states observed experimentally, DFT-based calculations of alkanedithiols coupled to Au electrodes were carried out. Calculations were performed for different configurations of an "extended molecule" composed of an *n*-alkanedithiol with variable chain length (*n* = 4...10) bridged between two pyramids of 45–55 Au atoms (Fig. 15a–c). These clusters mimic the contact region of the gold electrodes. Molecular
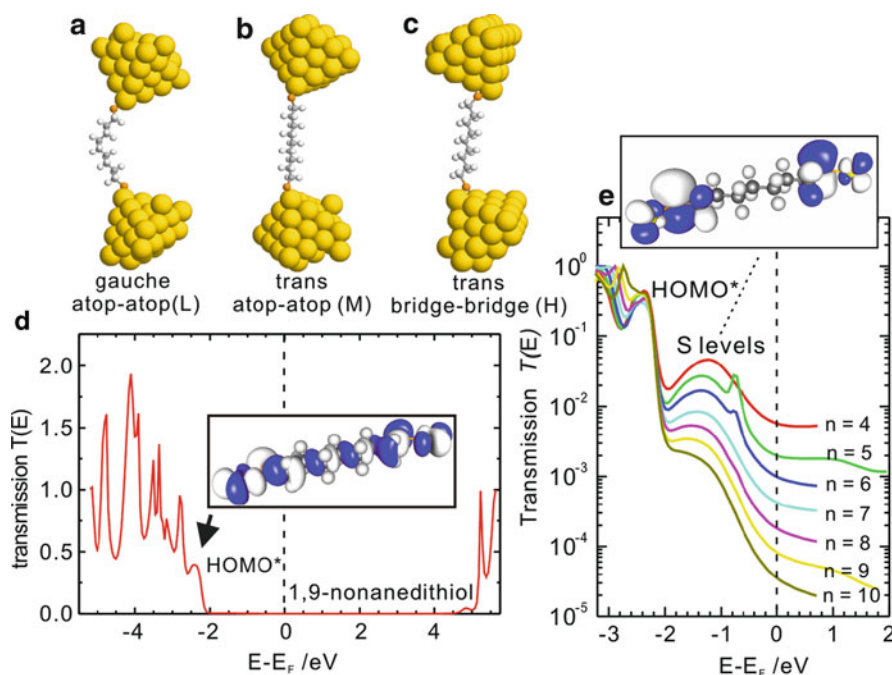
Fig. 15 Three typical arrangements of a single alkanedithiol molecule bridged between Au electrodes as used for the conductance calculations. (**a**) 1,9-Nonanedithiol (NDT) with one gauche defect and both terminal sulfur atoms coordinated in atop position (low, L). (**b**) NDT in all-trans conformation and atop–atop coordination (medium, M). (**c**) All-trans NDT in a bridge–bridge coordination (high, H). (**d**) Calculated energy-dependent transmission T(E) for a single NDT molecule bridged between gold electrodes in an all-trans atop–atop arrangement. The *inset* shows a molecular orbital of the Au–S–$(CH_2)_9$–S–Au cluster, formed by the HOMO of nonane hybridized with the sulfur and the Au electronic levels. This state determines the tunneling barrier. (**e**) Energy-dependent transmissions of n-alkanedithiols of various lengths n around the Fermi level. The *inset* displays the alkanedithiol's HOMO, which is an antisymmetric superposition of atomic wave functions localized on both sulfur atoms. The energy difference within its symmetric part, HOMO-1, is exponentially decaying with n

conformation and contact geometries have been varied. Examples are *gauche* and *trans* conformation of the alkyl chain, with the sulfur atoms bridged to one (*atop*), two (*bridge*) or three (*hollow*) gold atoms and/or combinations of them. The electron charge flow was described within the Landauer approach, formulated in terms of Green's functions, as implemented in a custom-made simulation package [64, 267].

Figure 15d illustrates a typical energy-dependent transmission curve, as calculated for n-nonanedithiol molecular junctions. The transmission represents the probability for electrons injected with the energy E from one electrode to be transmitted through the molecular junction. The conductance is defined by the transmission $T(E_F)$, evaluated at the Fermi energy E_F in units of the quantum of conductance $G_0 = 2e^2/h$. Molecular states of alkanedithiols appear as resonance peaks in the transmission spectrum (see Fig. 15d).

The Fermi energy E_F is situated in the alkane HOMO–LUMO gap (7.5 eV), giving rise to an effective barrier $\Phi_B = E_F - E_{HOMO*} = 2.14$ eV. The current flow involves mainly the HOMO (HOMO* of the alkanedithiol) depicted in the inset of Fig. 15d. Accordingly, the transmission $T(E)$ drops rapidly around -2.2 eV below E_F, and a nearly insulating gap spreads up all the way until 5.3 eV above E_F (alkane-LUMO, Fig. 15d, inset). Furthermore, the conductance through the *n*-alkanedithiol junction of the all-trans isomers with the sulfur coupled to single gold atoms at each electrode (atop–atop geometry) decays exponentially according to $G(N) = G_C \exp(-\beta_N N)$ with a decay constant $\beta_N = 0.83$ per CH_2 unit $G_C = 0.24$, $G = 18.5$ nS as contact conductance (Fig. 14d, circle). We note that the thiol linker-groups introduce two evanescent gap states, built of symmetric and anti-symmetric combination of wave functions, and localized at the sulfur atoms (Fig. 15e, inset). These states appear as broad resonances centered around 1.4 eV below E_F in the transmission spectrum (see Fig. 15e). The tails of such broad peaks, when approaching the Fermi energy (Fig. 6e), define the amplitude of the molecular conductance $G(n) \approx 2G_0 \Gamma_S \gamma_0 \exp[-\beta(E_F)n]/(E_F - E_S)^2$ and, therefore, predict an exponential distance dependence. Γ_S denotes an on-resonance probability amplitude (inverse lifetime) for an electron to hop from the sulfur atom to the nearest electrode. The other probability $\gamma_n(E) \ll \Gamma_S$ reflects tunneling through the molecule and is exponentially small, $\gamma_n(E) = \gamma_0 \exp[-\beta(E)n]$, where $\beta(E) \propto [E - E*_{HOMO}]^{1/2} d_0$ with d_0 as the unit length of the alkane chain, $d_0 = 1.28$ Å. Note that an evanescent state localized close to an Au surface does not change the tunneling asymptotics.

The model calculations revealed that the *bridge* contact geometry increases the conductance twice, as compared to the *atop* one. Due to the increase of the coordination number of the sulfur to the Au atoms (factor 2), the opening angle for the incoming electron wave is enlarged, providing an unchanged conformation of the alkyl chain. In other words, when two Au atoms are placed near one sulfur atom, the hopping probability increases by a factor of 2. On the other hand, this trend does not continue with a threefold *hollow* contact geometry. The contributions of three simultaneously contacted gold atoms to the overall junction conductance are overcompensated by a significant increase of the Au–S bond length.

Independent of the contact geometry, the calculations also demonstrated that the introduction of *gauche* defects resulted in a decrease of the bridge conductance by a factor of 10, as compared to an *all-trans* alkanedithiol chain (see Fig. 14b, triangles). Due to variations in the number and positions of gauche defects, as well as various contact geometries, the molecular junctions can exhibit conductance values up to two orders of magnitude below the conductance values of an *all-trans* conformation of the alkyl chain.

Comparison of the experimental data with the trends predicted from quantum chemistry ab initio simulations demonstrated that the multiple conductance values of "Au–alkanedithiol–Au" junctions could be attributed to different Au–sulfur coordination geometries and to different conformations of the alkyl chain. In particular, the medium conductance corresponds to an *all-trans* conformation of the alkyl chain, with each sulfur atom coordinated in *atop* position to a single

Au atom (see Fig. 15b). The "high" conductance values H represent an all-trans alkyl chain in combination with both sulfurs coordinated to two Au atoms in a *bridge* geometry (Fig. 15c). The theoretically predicted fourfold increase of the conductance, as compared to an *atop–atop* all-trans bridge, is close to the experimentally observed increase by a factor of 5. Other possible configurations with *all-trans* conformations (e.g., *atop–bridg*e, multiple molecular junctions) are assumed to contribute as part of the distribution to the less-dominant peaks in the conductance histograms (e.g., M2, H2, and H3 in Fig. 13).

The sequence of low conductance values L is attributed to isomers of alkanedithiols with *gauche* defects. This interpretation is also supported by the experimentally observed temperature dependence of L conductance values. The alteration of gauche states appears to be an activated process [244].

5 Chemically Controlled Conductance: Torsion-Angle Dependence in Single-Molecule Biphenyl Junctions

5.1 Introduction

Biphenyl derivatives (Fig. 16), consisting of two aromatic rings interconnected by a single C–C bond, gained considerable interest as subunits for single-molecule rectifying or switching systems, as the two π systems can be either in the same plane, or perpendicular to each other, representing "on" and "off" states [74, 268–272]. π–π coupling dominates the electron transport in aromatic bridges, and transport can be manipulated and tailored by controlling the degree of electron delocalization. Examples are the triplet energy transfer in a series of mixed

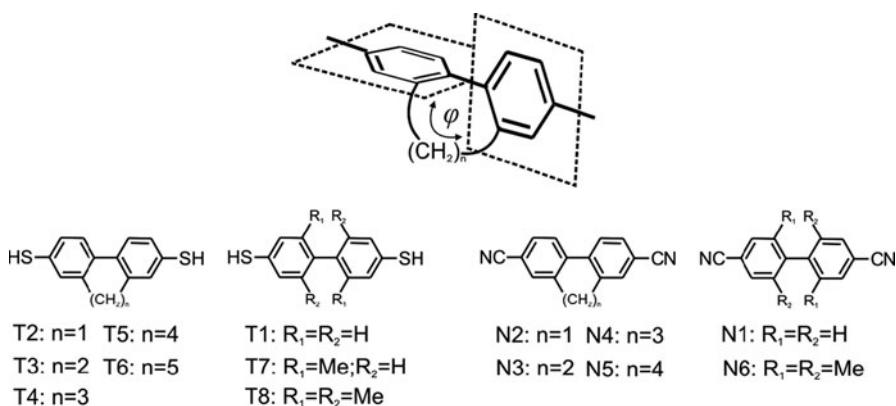**Fig. 16** Molecular structures of the biphenyldithiols T1–T8 and of the biphenyldinitrile N1–N6. The interplanar torsion angle φ of the biphenyl backbone is adjusted by methyl-group substitution or the length of the inter-ring alkyl chain [54, 75]

Ru–Os–bis(2,2 ′:6′,2″) terpyridine complexes attached to biphenyl spacer groups [273] and the electron transport characteristics of ferrocene covalently bound to OPE rods [274] or oligoaniline junctions [275].

The effect of rotating the middle ring of 1,4-bis-phenylethynyl-benzene on the conductance was estimated by Thomfohr and Sankey using the Landauer formalism in combination with a complex band structure analysis [276]. Venkataraman et al. demonstrated, in a series of terminally amine-functionalized biphenyls comprising electron-donating and -withdrawing substituents, that the junction conductances scale approximately linearly with the square of the cosine of the torsion angle φ between the planes of the two rings [48].

Despite the strong interest in the correlation between torsion angle and transport properties, suitable model compounds enabling the systematic variation of the torsion angle in biphenyl systems have not been realized so far, and the role of geometric and electric effects of the substituents is still being actively discussed [48, 72, 74, 271, 277].

As displayed in Fig. 16, an alkyl chain of varying length connected at the 2,2'-positions of the biphenyl system can adjust the resulting torsion angles φ. For both families of compounds, T and N, the length of the inter-ring alkyl chain is the only structural variation, keeping the electronic structure of the biphenyl systems as uniform as possible. Furthermore, the biphenyl conformation is locked by an intra-molecular bridge, with the number of CH_2 units dictating the torsion angle φ, lowering the expected motion and conformational variation of each molecule immobilized in the junction. The torsion angles φ have been estimated, based on crystal structure data and DFT calculations of the isolated molecules in the gas phase [54, 75].

The choice of the thiol anchoring groups ensures a strong chemical bonding to the leads, i.e., a stable junction configuration, with the current flow dominated by the molecular HOMO level [271].

We note that, although the thiol anchoring groups have been used most often, this choice is far from ideal. It shows a large variation in binding geometries, and does not allow an optimal electronic coupling between target molecules and contacting leads [64].

Venkataraman et al. [49] recently introduced the amine group (–NH_2) as a promising alternative, characterized by a more uniform contact geometry [73]. Other anchoring groups that have been explored in (single) molecule conductance studies are pyridine [32, 51], isonitrile (–NC) [49, 52], isothiocyanate (–NdCdS) [55], methyl selenide (–$SeCH_3$) [56], methyl thiol (–SCH_3) [56], dithiocarboxylic acid [–CS–SH] [62], dimethylphosphine [–$P(CH_3)_2$] [56], carboxylic acid (–COOH) [59], nitro (–NO_2) [278], and even fullerene [60]. The search for the "best" anchoring group for the formation of stable and energetically well-aligned metal-molecule contacts still represents a major challenge for fundamental and applied work in molecular-based electronics.

In this paragraph we complement experimental conductance data of a family of structurally well-tuned biphenyldithiols (BPDT) T1 to T8 [75, 76] with a family of biphenyl-dinitriles (BPDN) N1 to N6 [54] having the same molecular backbone,

but different anchoring groups. The electron-withdrawing nitrile group causes a
LUMO-controlled electron transport in BPDN molecular junctions [54], which are
distinctively different from BPDT. Conductance properties of the –CN anchoring
group have been explored in only two previous studies. Kiguchi et al. [53] reported
preliminary data with 1,4-dicyanobenzene, but did not observe any clear molecular
conductance signatures. Zotti et al. [278] performed current–voltage measurements
of 4,4'-dicyanotolane molecules attached to gold leads using an MCBJ technique,
but did not report a statistical analysis of their experimental traces, such as based on
1D or 2D conductance histograms.

5.2   Single-Molecule Junctions of Thiol-Terminated Biphenyls

The conductances of single-molecule "Au–BPDT–Au" junctions were extracted
from STM-BJ experiments based on the repeated formation and breaking of atomic
contacts between a gold STM tip and an Au(111) substrate in 0.25 mM solutions of
the respective BPDT in a 1:4 (v/v) mixture of tetrahydrofuran (THF) and
mesitylene ("hard touch") [75, 76].

Figure 17a shows, as an example, the plateau data-point histograms of T3 at
three bias voltages. Each histogram, constructed from more than 1,000 individual
traces, reveals a distinct maximum. The peak positions from individual experiments
are very reproducible for low bias voltages $|V_{bias} < 0.30\,\text{V}|$. The broad asymmetric
tail region toward higher conductance values is attributed to contributions from
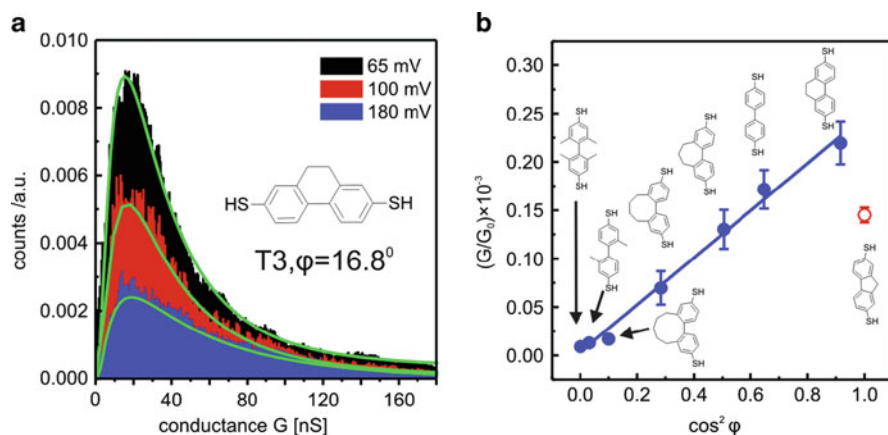
Fig. 17 (**a**) Plateau data-point histograms of the $(CH_2)_2$-bridged biphenyldithiol derivate T3, as
recorded from individual current–distance traces in an STM-based break junction experiment
(gold tip, Au (111) substrate) at three different bias voltages in mesitylene; $E_{bias} = 0.065$ V
(*black*), 0.10 V (*red*), and 0.18 V (*blue*). (**b**) Experimentally determined single-molecule junction
conductances of a series of biphenyldithiol molecules vs $\cos^2\varphi$, where φ is the torsion angle
between the two phenyl rings as given by the X-ray data [76]

minority junctions with multiple molecules, a modification in substrate-adsorbate coordination, atomic rearrangements upon stretching, or local surface roughness [64, 66, 116, 169, 245].

Introducing a bridging alkyl chain $(CH_2)_n$, $n = 0$–5, in the 2,2′-position (T1 to T6) or $-CH_3$ substitution in 2,2′- (T7) and 6,6′- (T8) hinders the free rotation and enables tuning of the torsion angles φ between the two phenyl rings from $0°$ to $90°$. The values of φ were estimated experimentally from the X-ray structure analysis of the acetyl-protected derivatives [75, 279, 280]. As the angle between the two phenyl rings increases, the conductance drops from 2.2×10^{-4} G_0 (T2) to 9.0×10^{-6} G_0 (T8). The lowest conductance was found for 2,2′,6,6′-tetramethyl-biphenyl-4,4′-dithiol (T8) with $\varphi = 89°$.

Figure 17b displays a linear correlation between the experimentally obtained single junction conductances of the eight BPDT derivatives and $\cos^2\varphi$. The fluorine derivative T2 appears to be an exception. Using $G = b + a \cos^2\varphi$ and excluding T2 from the data fit, we estimate the slope and the intersection as $a_{ex} = (2.44 \pm 0.097) \times 10^{-4}$ G_0 and $b_{ex} = (3.4 \pm 4.7) \times 10^{-6}$ G_0, respectively. The residual conductance b_{ex} at $\varphi = 90°$ stems mostly from σ–π couplings [276, 281]. However, this contribution is rather small. Clearly, the π–π overlap between the phenyl rings dominates the junction conductance [48, 271, 272, 277]. We conclude that twisting the BPDT systems from flat ($\varphi = 0°$) to perpendicular ($\varphi = 90°$) decreased the conductance by a factor of 30, following a linear $\cos^2\varphi$ dependence.

A HOMO-controlled transport mechanism and the experimentally observed linear relation between the junction conductance G and the square of the cosine of the torsion angle φ were also predicted by DFT-based model calculations [282–284] as well as by a simple Two-Level Model (TLM) [267, 285]. In these calculations, the molecular junctions were represented by an "extended molecule" composed of the BPDTs bridging two pyramids of 14–120 gold atoms. Figure 18a exhibits the two most probable and optimized structures *atop–atop* and *bridge–bridge*, which have been subsequently employed in the transport calculations. Figure 18b displays the resulting conductances of T1–T8. The fits of $G = a_{DFT} \cos^2\varphi$ to both series of data reveal a nearly linear behavior (Fig. 17b). However, one should note that the slopes $a_{DFT} = 0.094$ G_0 (atop) and $a_{DFT} = 0.13$ G_0 (bridge) are approximately three orders of magnitude higher, as compared to the experimental values: this is attributed to insufficient accuracy in the HOMO–LUMO level alignment and level broadening in DFT, a still unresolved problem [2, 286].

The main result of the transport measurement and DFT calculations is understood in terms of a TLM [76]. The model as parameterized by the DFT calculations demonstrated that the transmission through the molecular junction factorizes under "off-resonance" conditions, which enables the separate treatment of the "ring-to-ring" and "electrode-ring" transmission components. The electron path through the "extended molecule" is shown to be represented by three barriers, two of them representing the coupling to the leads, and the third defined by the torsion angle φ between the two phenyl rings. The theoretical analysis revealed unambiguously that the angular dependence of the overlap of the π-orbitals dominates the junction
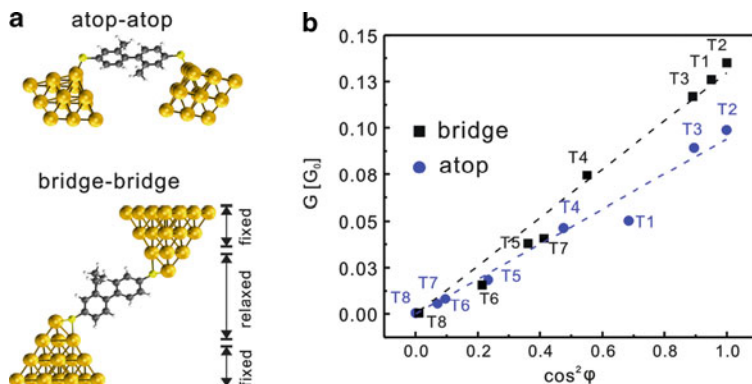
Fig. 18 (**a**) Examples of junction geometries of biphenyldithioles. *Upper panel*: T7 attached to gold pyramids in atop–atop position; *lower panel*: T4 attached in a bridge-bonded position. (**b**) Conductances as obtained from DFT-based transport calculations as a function of $\cos^2\varphi$: The *dashed lines* represent linear fits $G = a_{DFT}\cdot \cos^2\varphi$ with slopes $a_{DFT} = 0.094\ G_0$ (atop–atop) and $a_{DFT} = 0.130\ G_0$ (bridge–bridge) [76]

conductance for torsion angles in the range $0° \leq \varphi < 80°$. Contributions from degenerate σ–π and π–σ channels were only observed for biphenyl derivatives with completely broken conjugation, i.e., for $\varphi = 90°$.

5.3 Single Molecule Junctions with Nitrile-Terminated Biphenyls

Figure 19a shows, as an example, single stretching traces and the 1D histogram of molecular junctions created between the dinitrile derivative N4, torsion angle $\varphi = 44.8°$, and two gold leads. The predominant peak with a maximum at $G_{max} = 4 \times 10^{-5}\ G_0$ is attributed to the most probable conductance [54].

Figure 19b displays the 2D histogram of the experimentally obtained conductance of N4 plotted vs distance [63]. The distance scale z' is normalized with respect to $z' = 0$ at $G = 0.7\ G_0$, to a common point. The chosen procedure is justified, because of the steep decay of the tunneling current after breaking of the last atomic contact. The histogram counts the occurrence of $[\log(G/G_0), z']$ pairs in a 2D field. Figure 19b exhibits the features of gold quantum contacts at $G \geq G_0$, and a second cloud-like pattern in $[10^{-5} \sim 10^{-4}\ G_0, 0 \sim 0.5\ \text{nm}]$. We attribute the latter to the formation of single-molecule junctions of only one type. The center of the cloud is located at $G = 3.5 \sim 4.5 \times 10^{-5}\ G_0$, close to the peak position in the 1D histogram (Fig. 19a). The extension of the cloud along the distance scale is around 0.5 nm, close to the typical length of the plateaus (the inset of Fig. 19a).

The dependence of the single-molecular conductances on the torsion angle φ between the two phenyl rings was addressed by choosing a series of five additional BPDN derivatives (Figs. 16 and 20a) [287]. All conductance histograms exhibited only one dominant single molecular junction-related feature, which is rather sharp
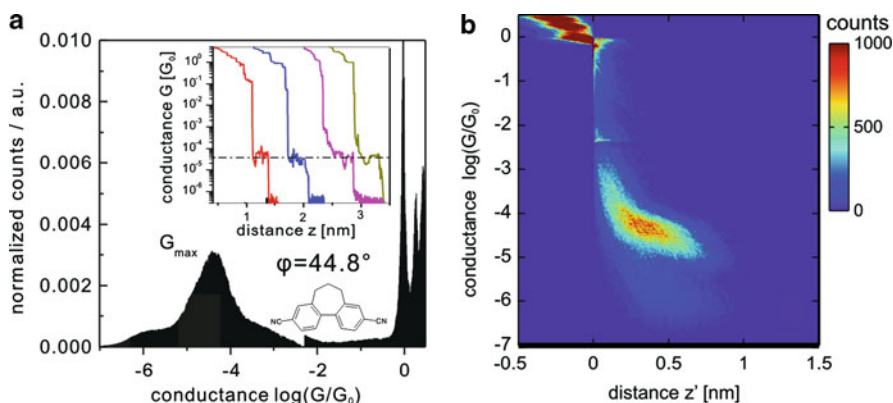
Fig. 19 (**a**) All data-point logarithmic conductance histogram as constructed from ~2,000 individual conductance–distance traces of N4 without any data selection. The experiment was carried out with 0.1 mM N4 solution in mesitylene: THF (4:1, v/v) at $E_{bias} = 0.1$ V. The *inset* shows selected individual stretching traces in a logarithmic conductance scale. (**b**) Two-dimensional (2D) conductance–distance histograms for N4, displaying the range of Au–Au contacts between 1 G_0 and 10 G_0, and a cloud-like feature between $10^{-3} \cdot G_0$ and $10^{-5} \cdot G_0$ representing the region of molecular junctions [54]
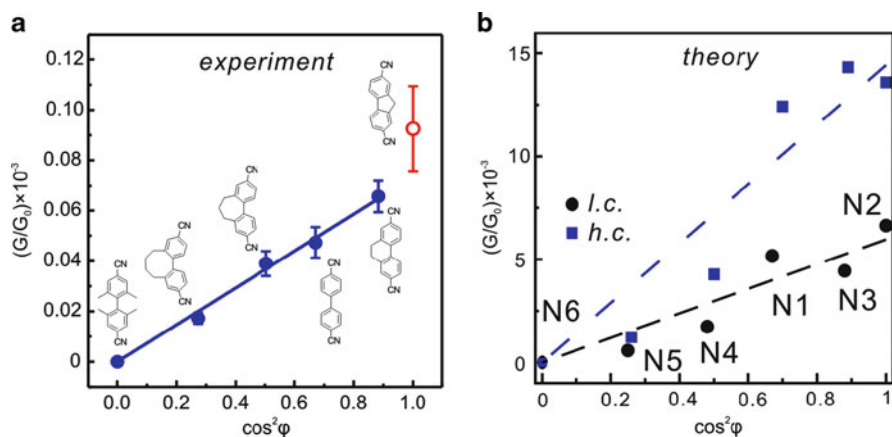
Fig. 20 (**a**) Experimentally measured conductances G/G_0 of the six biphenyl dinitriles N1–N6 as a function of $\cos^2\varphi$. (**b**) Computed conductances of N1–N6 as a function of $\cos^2\varphi$ for the low-coordination (*l.c.*, *circles*) contact geometry and the high-coordination (*h.c.*, *squares*) contact geometry [54]

and well-defined [54]. The result reflects the more uniform nitrile-gold bond, as compared to the family of BPDT derivatives T1 to T8 [64, 76, 242, 243]. The conductance values of all six BPDNs were plotted in Fig. 20a as a function of $\cos^2\varphi$, which demonstrates a linear dependence with the slope of $(7.3 \pm 0.2) \times 10^{-5}$ G_0. This slope, as well as the absolute magnitude of the BPDN molecular

junction conductances, is smaller, as compared to the results for BPDT. Both revealed the stronger electronic coupling of the thiol group to the Au leads, as compared to the nitrile group.

Ab initio transport calculations on electronic structure and zero-bias conductances of the molecular junctions showed a monotonic decrease of the HOMO–LUMO gap with decreasing torsion angle, except for a deviation for the fluorene derivative N2 [285]. The calculations also predicted two stable *atop* binding geometries of the nitrile-gold contact. The target molecules can bind either to a low-coordinated gold adatom (referred to as *l.c.*) or to a "terrace-type" gold atom (referred to as *h.c.*) in *atop* position. *Hollow* and *bridge* binding geometries were demonstrated to be unstable for the BPDN derivatives. The calculated transmission curves at zero bias of N1 to N6 for both *l.c.* and *h.c.* geometries reveal that the transport pathway proceeds by off-resonance tunneling through the tail of the LUMO. This is consistent with the results of previous calculations [278, 288] and with thermopower measurements [289].

The computed conductance values of the BPDN junctions are plotted in Fig. 20b as function of $\cos^2\varphi$. The correlation is linear, with a higher slope for the *h.c.* geometry ($a = 1.44 \times 10^{-2} \, G_0$ and $a = 5.9 \times 10^{-3} \, G_0$, respectively). The higher slope for the *h.c.* geometry reflects the better coupling (broader resonance) between the molecular π-system and the metal states, as caused by the tilt of the molecular backbone and the presence of additional gold atoms on the surface. Experimentally, the two theoretically predicted most probable junction geometries for the BPDN family could not be distinguished, due to the rather broad conductance maxima in the respective histograms [76].

6   Electrochemically Gate-Controlled Conductance of 4,4'- Bipyridine Single-Molecule Junctions

The experiments discussed in the previous sections were carried out in non-conductive organic solvents, with a focus on chemically tuning charge transport characteristics in single-molecule junctions. In the following a gate voltage is applied to tune the orientation of a molecular wire in a nanoscale gap in a polar electrolyte under full electrochemical potential control. The approach will be exemplified by 4,4'-bipyridine attached to two gold contacts in aqueous electrolyte [290].

6.1   Introduction

4,4'-Bipyridine (44-BP) is a bifunctional, non-chelating molecule, which consists of two planar pyridyl rings connected by a C–C bond in 4 and 4' positions. It has been extensively employed as a bridging ligand in coordination chemistry [291].

The binding energy per N-site in 44-BP–metal coordination complexes amounts to 60–120 kJ mol^{-1}, i.e., it ranges between strong covalent bonding and weak bonds in biological systems [292].

The rotation angle between the two planar pyridyl-rings was found to vary between 18.2$^{°}$ (solid-state [293]) and 37.2$^{°}$ (gas-phase [294]). H-NMR experiments in several solvents of different dielectric constants revealed that 4,4'-BP appears either highly twisted, or as a free rotor. The barrier to internal rotation has been estimated to be 17.0 kJ mol^{-1}. The two rings are rotating almost freely in most liquid environments [295–297].

44-BP has two lone electron pairs at each nitrogen atom. These lone pairs enable an effective molecule-substrate coordination, that is, the electronic overlap of molecule and substrate states. The relatively low lying π*-orbitals may act as good acceptors of d-orbital electron density in metal (electrode)-ligand back-bonding. However, the nitrogen lone-pair electrons are not delocalized. They are orthogonal to the molecular π-system, causing the conductance of a 44-BP-based molecular wire to be quite sensitive to the orientation of the Au–N bond, relative to its principal conducting orbital. Theoretical calculations have demonstrated that the LUMO lies relatively close to the FERMI level, i.e., the LUMO π-state provides the dominant contribution to charge transport through the molecule. The HOMO–LUMO gap is around 5 eV [298, 299].

Tao et al. reported the first single-junction conductance data of 44-BP attached to two gold leads in an aqueous environment as ~ 0.01 G_0 [32, 300] by using the STM-BJ technique. Multiple single-conductance values have recently been reported by Zhou et al.: 4.7×10^{-3} G_0 and 0.59×10^{-3} G_0 [301] and Wang et al.: $(1.34 \pm 0.17) \times 10^{-4}$ G_0, $(5.38 \pm 0.64) \times 10^{-4}$ G_0, and $(75.5 \pm 15.3) \times 10^{-4}$ G_0, which were obtained in aqueous electrolyte, as well as in nonconductive organic solvents. These experimental observations were attributed to different contact geometries between the pyridyl anchoring groups and the gold electrodes [50]. Venkataraman et al. demonstrated experimentally, and in combination with DFT calculations, that two conductance states of 44-BP molecular junctions could be rationalized by a tilted (high conductance: ~6×10^{-4} G_0) and an elongated perpendicular orientation (low conductance: ~1.6×10^{-4} G_0) of the molecule between the two gold leads. These authors demonstrated reversible binary switching between the two conducting states in a single molecular junction by mechanical control of the metal-molecule contact geometry [299]. This interpretation was recently shown to be more general, in a conductance study with an extended family of pyridine-terminated derivatives in 1,2,4-trichlorobenzene [51].

In the following we will present results of a single-junction conductance study with 44-BP under electrochemical potential control, enabling the precise tuning of the molecular orientation, relative to the substrate, upon application of an adjustable gate voltage [290] in a well-controlled environment [86, 302].

6.2 Interfacial Electrochemical Characterization of 4,4'- Bipyridine on Au(111)

Figure 21 shows the cyclic voltammogram of 3 mM 44-BP in an aqueous solution of 0.05 M $KClO_4$ on Au(111) [304]. Four different interfacial regions, labeled I to IV, can be distinguished, which are separated by distinct peaks. The double-layer region was limited between the onset of OH^- adsorption or the beginning of gold oxidation, and the desorption/reduction of 44-BP on Au (111).

Excursion of the electrode potential from region I to more negative values triggers two first-order phase transitions, characterized by the loss of the parallel stacking rows, and accompanied by an orientation change of 44-BP from a perpendicular to a more tilted one, simultaneously with the rearrangement of co-adsorbed interfacial water molecules. The adlayer coverage decreases from 6.8×10^{-10} mol cm^{-2} (densely packed phase in region I, Fig. 21a) via 5.7×10^{-10} mol cm^{-2} (striped phase in region II, Fig. 21b) to 3.4×10^{-10} mol cm^{-2} (rhombohedral phase in region III, Fig 20c). The corresponding molecular orientations, as shown in Fig. 21d–f, display a tilt angle, with respect to the normal axis of the electrode surface, changing from zero via ~25° to ~60°. The position of the neighboring molecules are determined by the competition between molecular and substrate coordination sites and intermolecular interactions of the π-systems. The variation of the 44-BP surface structures, upon decreasing the electrode potential, is accompanied by a decrease in surface
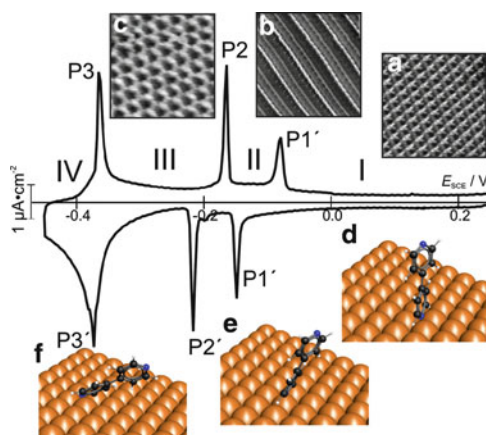

Fig. 21 Cyclic voltammogram and corresponding in situ STM images of 3 mM 4,4'-bipyridine (44-BP) on Au(111) in 0.05 M $KClO_4$, scan rate 10 mV s^{-1}. The sizes of the STM images are 10×10 nm^2. The following 44-BP adlayer structures have been observed in the potential regions I, II, and III: (**a**) high coverage densely packed phase, (**b**) striped structure, and (**c**) rhombohedral phase. The corresponding molecular orientations as derived from in situ IR studies on Au(111) are shown in panels (**d–f**) [303]. The pairs of peaks P1/P1', P2/P2', and P3/P3' indicate first-order phase transitions between the respective adlayers [304]

coverage. Polarization at more negative potentials also leads to a decrease of the Au–N binding strength [303–306].

6.3 Single-Molecule Junction Conductance

STM-BJ experiments were performed to extract single-junction conductances of 44-BP bridged between a gold STM tip and an Au (111) substrate in non-polar solvents, such as mesitylene, isopropanol, and 1,2,4-trichlorobenzene, as well as under full electrochemical potential control in aqueous solutions of $HClO_4$ and $LiClO_4$ at various pH.

Figure 22 shows typical individual conductance traces of 44-BP molecular junctions, recorded over seven orders of magnitude with an STM-BJ technique, and the corresponding conductance histograms. The experiment started with the breaking of metal atomic contacts ("hard contact"), as indicated by the region labeled with G_0 in Fig. 22a. Several groups reported that, immediately after breaking an atomic Au–Au contact, the gap relaxes due to adhesion between Au atoms leading to an immediate separation between the leads of 3–5 Å [307, 192, 308]). Therefore, one can expect a large drop in conductance, which is observed experimentally. Simultaneously, adsorbed solution-based 44-BP molecules with a molecular length of ~7.2 Å will bridge the gap. The subsequent breaking of these (single) molecular junctions leads to plateaus and steps in the conductance–distance traces below 10^{-3} G_0 (c.f. Fig. 22a).

The statistical analysis of these conductance traces (an example is given in Fig. 22b for $E_S = 0.25$ V, which is close to the PZC [304]) reveals three distinct conductance peaks (high H, medium M, and low L) in the region between $10^{-2.5}$ G_0 and $10^{-4.5}$ G_0, with the most probable conductances evaluated by Gaussian fits as 14 nS (L), 38 nS (M), and 78 nS (H). The high conductance value H is twice as large as the medium one M, and the M value is three to four times larger than L. Similar
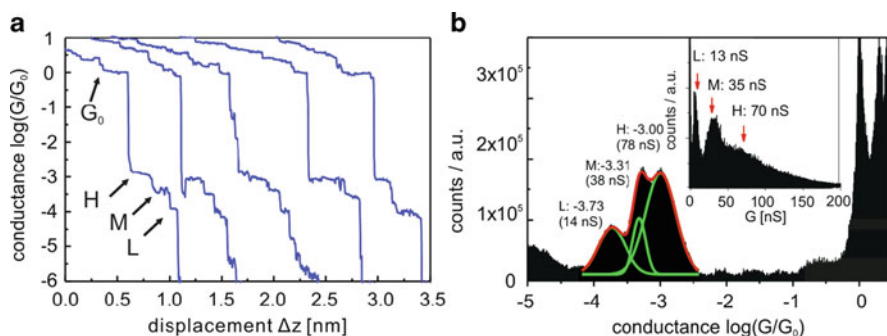

Fig. 22 (**a**) Conductance–distance traces for 3 mM 44-BP in 0.1 M $HClO_4$ at $E_S = 0.25$ V (vs SCE), stretching rate 60 nm s^{-1}. (**b**) Conductance histogram in logarithmic and linear (*inset*) scales built from ~2,000 single traces, created without any data selection
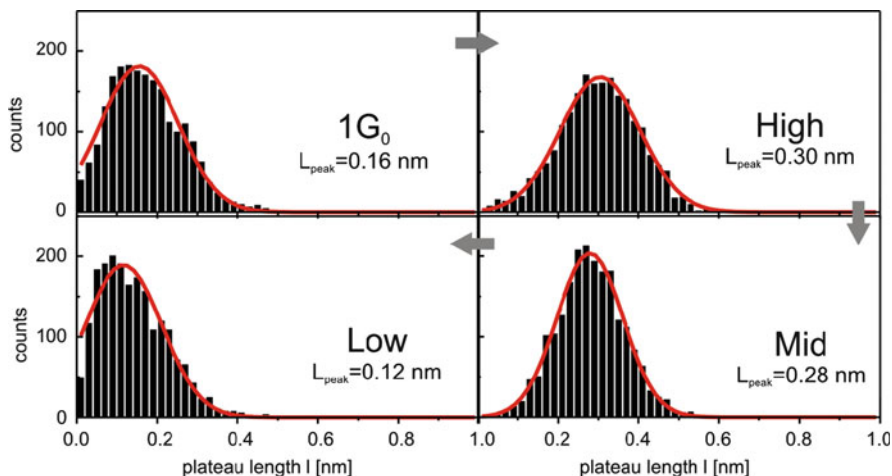
Fig. 23 Plateau length histograms [54] of the breaking of Au–Au nanocontacts in the presence of 44-BP, i.e., around 1 G_0, as well as of the molecular junctions labeled H, M, and L in Fig. 22. Gaussian fits (*solid red line*) revealed the most frequently observed plateau length in the individual conductance–distance curves

values of the three conductance states, as just reported for electrochemical conditions at the PZC ($E_S \sim 0.25$ V), were also found in non-conducting organic solvents, such as 1,3,5-trimethylbenzene, 1,2,4-trichlorobenzene, or isopropanol [290]. The M and L values are also in good agreement with results previously reported by Quek et al. [299] and Wang et al. [305].

The statistical analysis of the plateau-length histograms, c.f. Fig. 23, revealed that the most probable plateau length of an Au–Au atomic contact junction in the presence of 44-BP amounts to $l_{Au} \sim 0.16$ nm, which is slightly shorter than data obtained for Au nanocontacts in aqueous electrolytes containing weakly specifically adsorbed ions but no organic molecules (see also Sect. 3). The values for the 44-BP-related single-molecule junctions H and M, $l_H = 0.30$ nm and $l_M = 0.28$ nm, are significantly higher, while the low-conductance molecular junctions exhibit a rather short most probable plateau length $l_L = 0.12$ nm. These qualitative differences point to distinct differences in the respective single-molecule junctions. Kamenetska et al. pointed out that plateaus in the conductance–distance traces are usually caused by the stretching of gold electrodes and molecular contacts, the rearrangement of gold atoms, "molecular sliding" on the electrodes, as well as by orientation changes of molecules in the gap [66].

The combination of experimental observations on most probable single-junction conductances and plateau lengths with electronic and transport calculations employing the SMEAGOL code [309] suggests the following scenario [290]. A monatomic contact is initially formed, and subsequently elongated upon stretching, which leads to the plateaus in the conductance–distance traces around 1 G_0. Since the gap between the "pulled" electrodes formed immediately after relaxation of the
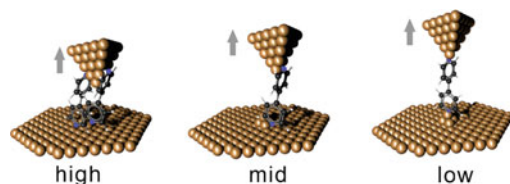
Fig. 24 (**a**) Suggested junction geometries representing a typical stretching trace: High (H) – two 44-BP molecules with the π-system of the pyridyl rings coupled to the gold electrodes; Mid (M) – single 44-BP coupled to sides of Au tip and substrate via adatom assemblies; Low (L) – single 44-BP molecule bound in upright orientation to two lower-coordinated gold adatoms [290]

Au atom positions ("snap back" [299]) is shorter than the molecular length of 44-BP, one or more 44-BP molecules can only bind sideways (c.f. Fig. 24a) with the conducting π-system being inclined with respect to the N–Au bond of the pyridyl nitrogen to an under-coordinated gold surface atom. This gives rise to an H-type high-conductance junction. As the junction is elongated, only one molecule is allowed to slide on the surface, due to the limited binding site near the apex of the electrode, causing the M plateaus. The further elongation leads finally to a binding geometry with the pyridyl nitrogen–gold bond to an under-coordinated Au atom being perpendicular to the molecular π-system, until the junction breaks, causing the L-type plateaus. Ideally, these four events are expected to take place sequentially. Figure 24 shows cartoons illustrating the various suggested junction geometries during the evolution of a "most probable" stretching trace [290].

6.4 Electrochemical Gate Effect

The conductance experiments with 44-BP junctions were extended to an electrochemical environment. This approach enables the application of an "electrolyte gate field" for tuning the 44-BP surface orientation on the Au(111) electrode between upright (in the potential region I) and strongly inclined with the π-system facing the substrate (in region III). The electrochemical experiments were performed in $LiClO_4$ or $HClO_4$ solutions containing 3 mM 44-BP. The solution pH was also varied to address the influence of 44-BP protonation, i.e., 44-BPH$^+$ and 44-BPH$_2^{2+}$, on the junction conductance characteristics ($pK_{a1} = 2.69$; $pK_{a2} = 4.77$) [310].

Figure 25a, as an example, shows the potential dependence of the single-junction conductances of 44-BP measured in 0.1 M $HClO_4$ solution (pH 1) in -0.10 V $<$ E < 0.90 V in a semi-logarithmic representation. The values of L, M, and H decrease with more positive electrode potentials, and follow nearly the same trend for each family. The single-junction conductances decrease by a factor of 3–5 upon potential excursion towards positive values in the accessible potential region. A similar trend is also observed for electrolytes with variable pH ranging between 1 and 10, as
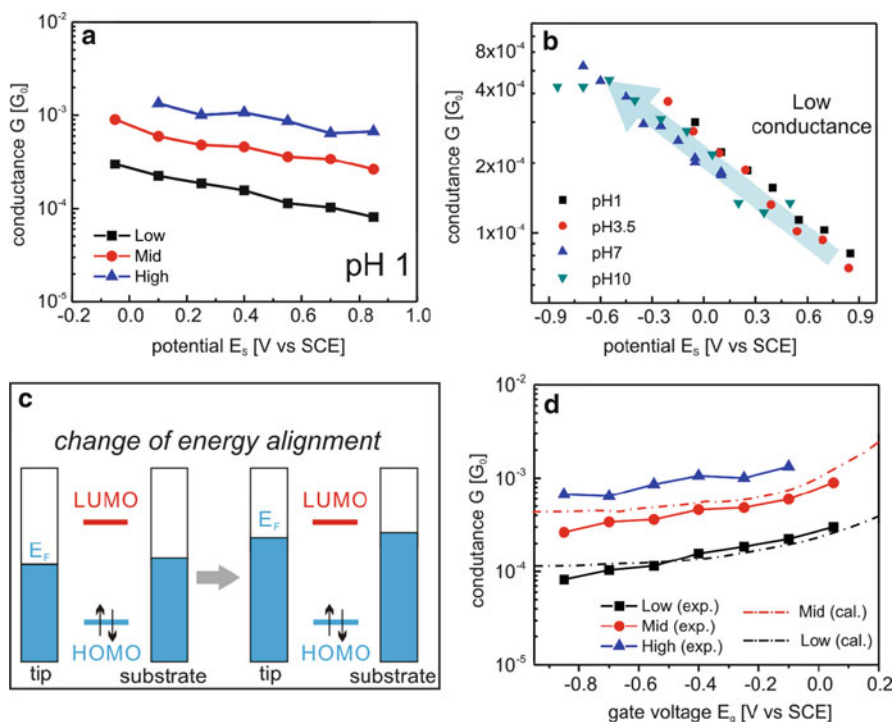
Fig. 25 (**a**) Potential dependence (E_S) of the single molecular junction conductances of 3 mM 44-BP in 0.1 M HClO$_4$. E_{bias} = 0.10 V; tip retraction rate 60 nm s^{-1} (see also Fig. 22). (**b**) Low conductance L plotted as a function of the applied electrode potential for different values of the solution pH. The pH was adjusted by HClO$_4$ or NaOH. (**c**) Schematic representation of the energy level alignment between the electrode's Fermi levels E_{tip} and E_S and the molecular frontier level upon sweeping the electrode potentials to more negative values. (**d**) Comparison between the experimentally measured conductances shown in (**a**) and computed conductances log $(G(E_g)/G_0)$ = log $[T (E_F(E_G))]$ + A at various gate voltages [290]

exemplified for the case of low conductance values L in Fig. 25b. The L conductances increase monotonously with a decrease of the electrode potential, and do not depend on the solution pH. A deprotonation process seems to precede the formation of the molecule–metal contacts. We also note that the electrochemically-induced tuning of the junction conductance ("electrolyte gating") is fully reversible.

We attribute the enhancement of the junction conductance driven by an electrochemical potential to the alignment of the molecular frontier level with the Fermi levels of the gold leads. As illustrated in Fig. 25c, upon sweeping the electrode potential towards more negative values, the Fermi levels of the electrodes shift upwards and align better with the LUMO of 44-BP. We note that charge transport through 44-BP single-molecule junctions is dominated by the LUMO of the 44-BP extended molecule. Due to the relatively small HOMO–LUMO gap of 44-BP, the alignment of the 44-BP LUMO and the Au Fermi levels changes from off-resonance to a "partially" resonant state, leading to an increase in the transmission

through the 44-BP single-molecule junctions. This trend is corroborated by a simultaneous change in orientation of the adsorbed 44-BP molecules on Au(111) from upright to tilted upon negative polarization of the electrode [303].

The above qualitative reasoning is supported by a theoretical study of the effect of electrochemical gating in molecular transport. The gate potential $E_G = -(E_S - E_{SCE})$ produces a shift in the Fermi energy, relative to the non-gated value. The gate-shifted Fermi level is expressed as $E_F(E_G) = \beta E_G + E_F(0)$, where $E_F(0)$ is the value of E_F in the absence of gating, and β is the gate control parameter [311]. Figure 25d shows the calculated gated conductances $\log(G/G_0) = \log T (E_F(E_G)) + A$, obtained from the tails of the LUMO resonance, where the optimum fit is obtained by choosing $\beta = 0.5$ and $E_F(0) = E_F^0 - 0.35$ V (E_F^0 is the bare Fermi energy predicted by DFT) [290]. The correction factor $A = -0.74$ is chosen to account for the slight discrepancies between the measured and the computed conductances, which arise from a range of factors, including the statistical distribution of atomic configurations and the choice of the basis set. Figure 25d shows that, over a wide range of gate potentials, the ratio G_{Mid}/G_{Low} is approximately 3.8, which is in good agreement with the experimentally observed ratio of M and L conductance values.

Finally, we note that the present observation is different from tunneling enhancement mediated by an oxidation/reduction process, which is accompanied by electronic structure changes of the junction ("inner-sphere reorganization energy") as well as reorientation of dipolar solvent molecules ("outer-sphere reorganization energy"). 44-BP keeps its neutral state, and therefore represents a universal case study, which will have analogs in many junctions of organic molecules exhibiting a relatively small HOMO–LUMO gap.

7 Electrochemically Gate-Controlled Charge Transport in Redox-Active Molecular Junctions

Redox-active molecular junctions represent a particularly unique class of systems for "electrolyte gating" and beyond. The electrochemical approach and a summary of systems explored have already been introduced in Sect. 2. In an attempt to contribute to a more advanced understanding of the phenomena involved, we have recently carried out several systematic experimental and theoretical studies with three families of molecules, i.e., derivatives of viologens [34, 110, 114], perylene bisimides [170], and ferrocenes [150]. In the following, several results as obtained with perylene bisimide derivatives (PBI) will be presented, to illustrate the uniqueness of the electrochemical approach in single-junction charge-transport experiments. In particular, the influence of anchoring group, chemical substitution at "bay positions", and electrochemical gating will be addressed.

7.1 Introduction

As a class of n-type organic semiconductors, PBI derivatives have received considerable attention for a variety of applications [312, 313], for example, for organic or polymer light-emitting diodes (OLEDs and PLEDs) [314, 315], thin-film organic field-effect transistors (OFETs) [316, 317], solar cells [318, 319], and liquid crystals [320]. They are also interesting candidates for single-molecule device applications, such as sensors [321], molecular wires [322], or transistors [141].

The PBI core exhibits a flat π-system, composed of two naphthalene half units, each of which is attached to an imide unit, and connected to the other naphthalene unit by two C sp^2–C sp^2 single bonds (Fig. 26a). The HOMO and LUMO exhibit nodes at the positions of the imide nitrogens, which provide unique opportunities for modifying the structure of the linker groups, without alterations of the electronic properties of the core π-system. On the other hand, the introduction of substituents at the 1,6,7,12 "bay positions" may significantly alter the electronic and optical properties (c.f. inset of Fig. 26a), from electron-poor to electron-rich, without changing the dimensions in the direction of the long molecular axis, which determines the length of a molecular junction. In addition, these substituents create steric strain in the bay area, leading to a propeller-like twisting of the two naphthalene half units [312, 323], which prevents π–π stacking between adjacent molecules, and therefore promotes the formation of single-molecule junctions. The twist angle of the π-system can be tuned from 0° (no substituent) up to 37° (tetra-chloro substitution). Voltammetric and spectro-electrochemical studies with PBI dissolved in organic solvents revealed two reversible one-electron reductions (formation of the stable radical anion PBI$^{•-}$ and the dianion PBI^{2-}) and a single one-electron oxidation [324].
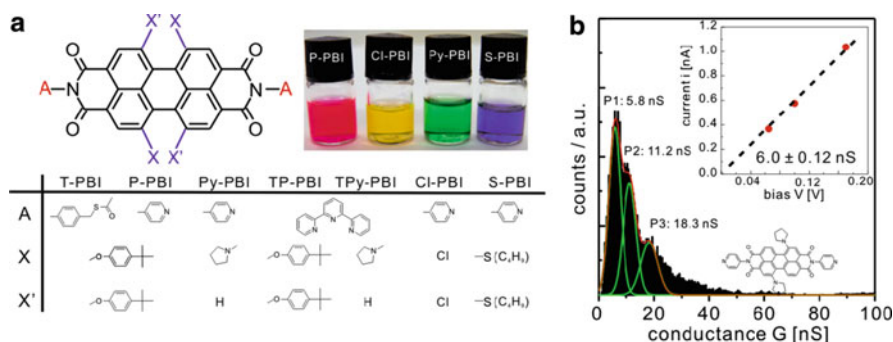
Fig. 26 (**a**) Structures of pyridine-, terpyridine-, and thiol-terminated PBI derivatives with different substituents at the "bay positions" X and X'. The *inset* illustrates the alternation of optical properties of the PBIs with different bay-area substituents. (**b**) Plateau data-point histogram of Py-PBI in a mixture of mesitylene/THF (4:1). E_{bias} = 0.1 V, tip retraction rate was 60 nm s^{-1}. The *inset* show the bias voltage dependence of the current through a molecular junction

Li et al. [169] reported that the single-junction conductance of PBI-type molecules can be modulated by two to three orders of magnitude by varying the electrode potential. These authors also found a temperature-dependent junction conductance, indicating a thermally activated process. Sun et al. predicted a LUMO-mediated electron transport process [325]. The experimentally observed temperature dependence was related to a modulation of hydrogen bonding between the four oxygen atoms of PBI and the surrounding water molecules [326].

The following section reports the charge-transport characteristics of symmetric PBI single-molecule junctions (where PBI is attached with two anchoring groups to two contacting leads) and also asymmetric PBI-mediated tunneling junctions (where the PBI derivative is bound only to one electrode), as a function of the anchoring groups and the bay-area substitution in two different environments, in non-conducting organic solvents, as well as under electrochemical conditions. Basic relationships between electron transport properties and molecular structure will be addressed [170].

7.2 Chemically Controlled Conductance of Perylene Bisimide Derivatives

The PBI molecules studied include pyridyl-(P-PBI), terpyridyl (TP-PBI), and thiol-terminated (T-PBI) perylene-3,4:9,10-tetra-carboxylic acid bisimides, that contain bulky *tert*-butylphenoxy substituents at 1,6,7,12 bay positions, and pyridyl-(Py-PBI) and terpyridyl- (TPy-PBI) terminated perylene-3,4:9,10-tetra-carboxylic acid bisimides, that contain bulky pyrrolidinyl substituents at 1,7 bay positions (Fig. 26a) [327–329].

Figure 26b shows, as an example, a plateau data-point histogram obtained for 0.1 mM Py-PBI at 0.1 V bias voltage in mesitylene/THF. The graph reveals three equally spaced maxima, separated by integer values of the conductance of the most prominent first peak at 6.0 ± 0.1 nS, which is assigned to the single-molecule conductance. The other peaks are interpreted as multi-molecule junctions. The conductance histograms were constructed from 10–25% of the experimentally recorded traces because of the low yield of successfully formed molecular junctions. Table 2 summarizes the results.

The low conductance of the π-conjugated system is due to the nodes at the imide nitrogen positions. Several additional trends have been observed. The conductance of pyridine-terminated PBI derivatives (P-PBI) is typically a factor of 2 larger than the thiol-terminated ones (T-PBI). Although the Au–S bond provides a stronger electronic coupling than the Au–N bond, the T-PBI has two extra methylene

Table 2 Summary of measured conductances of single PBI-type molecular junctions

Molecule	T-PBI	P-PBI	Py-PBI	TP-PBI	TPy-PBI
Conductance[nS]	2.5 ± 0.1	5.0 ± 0.2	6.0 ± 0.1	4.8 ± 0.3	3.8 ± 0.2

spacers at each side, which act as insulating units. The conductance of TP-PBI is slightly smaller than that of P-PBI, possibly caused by the less efficient bonding geometry (steric hindrance) and the longer bonding distance of the terpyridine group, as compared to pyridine.

The conductance of 1,7-pyrrolidinyl-substituted PBI (Py-PBI) is slightly larger than that of 1,6,7,12-butyl-phenoxy-substituted PBI (P-PBI). The bay-area substituents affect the transport properties of PBI molecular junctions in two ways: (1) the substituents alter the twist angle of the PBI core and (2) electron-withdrawing or -donating substituents shift the molecular frontier orbital relative to the electrode Fermi levels. According to a semiempirical AM1 calculation, the twist angles of the bay area unit for P-PBI and Py-PBI are 27° and 25°, respectively [330]. It is evident that a smaller twist angle leads to a higher degree of π-conjugation, and consequently also to a larger conductance. On the other hand, electron-donating substituents of the PBI core could confine the HOMO level. Oxygen or nitrogen lone-pair electrons delocalize into the PBI π-space, and thereby raise the HOMO level. The pyrrolidine has a stronger electron-donating effect, compared to butyl-phenoxy substituentens, causing a larger increase of the molecular frontier orbital energies. In conclusion, the changes of both the conformation and the energy levels of the frontier orbitals lead to the differences in single-junction conductances, as observed between P-PBI and Py-PBI.

Finally, we note that the idea of manipulating transport properties of molecular junctions by the modification of a "master rod" with electron-withdrawing or -donating groups was demonstrated before, experimentally [49] and theoretically [331–333].

7.3   Electrochemical Characterizations

Figure 27a shows a typical CV of 1 mM P-PBI in dicholoromethane (DCM) with 0.1 M tetrabutylammonium hexafluorophosphate (TBAPF$_6$) as the supporting electrolyte. One may distinguish three characteristic pairs of current peaks labeled as O^c/O^a, R_1^c/R_1^a, and R_2^c/R_2^a. The positions of the corresponding potentials are independent of scan rate v in the range 0.01 V s^{-1} $< v <$ 1.00 V s^{-1}. The peak heights scale linearly with the square root of the scan rate v. These observations indicate a reversible, bulk-diffusion-controlled process. O^c/O^a is assigned to a reversible one-electron oxidation process PBI/PBI$^+$, R_1^c/R_1^a and R_2^c/R_2^a to two one-electron reduction processes PBI/PBI$^{\bullet-}$ and PBI$^{\bullet-}$/PBI^{2-}, respectively [312, 329]. The reduction of Py-PBI with the electron donating dipyrrolidinyl-bay-area substituents requires more negative potentials. One also observes two reversible one-electron reduction peaks [328].

Figure 27b shows typical voltammograms of monolayers of three PBI derivatives on Au (111). The two reduction peaks merge into a single broad peak, due to specific solvent-PBI interactions, as well as the possibility of incorporating cations of the supporting electrolyte into the charged PBI adlayers. The peak-to-peak
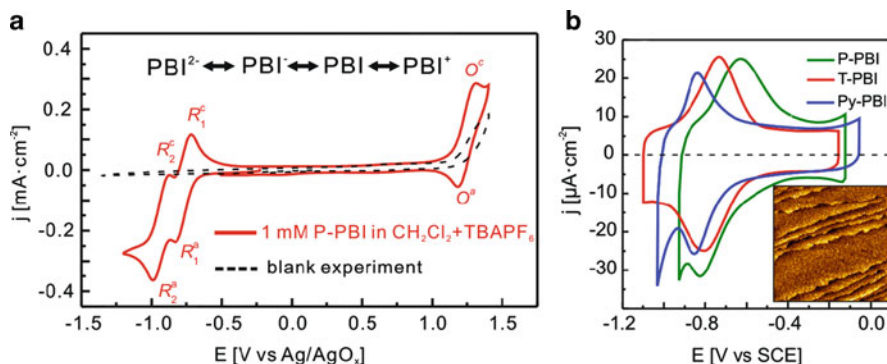
Fig. 27 (**a**) Cyclic voltammograms with (*red line*) and without (*dotted black line*) 1 mM P-PBI in CH_2Cl_2 + 0.1 M $TBAPF_6$ on Au (111), scan rate 0.1 V s^{-1}. (**b**) Cyclic voltammograms of monolayers of P-PBI (*green*), T-PBI (*red*), and Py-PBI (*blue*) immobilized on Au (111)-(1 × 1) in 0.05 M $LiClO_4$, pH ~ 12, scan rate 0.2 V s^{-1}. The *inset* shows a typical STM image of the disordered high coverage T-PBI adlayer on Au(111)-(1 × 1) in 0.05 M $LiClO_4$, pH ~ 12 (200 × 200 nm, i_T = 0.1 nA; E_S = −0.02 V(vs SCE), E_{bias} = 0.1 V) as recorded before or during the transport measurements [170]

separations are 0.07 ± 0.02 V for T-PBI, 0.15 ± 0.03 V for P-PBI, and 0.03 ± 0.01 V for Py-PBI. The peak positions are independent of scan rate v, and their heights scale linearly with v in the range of 0.01 V s^{-1} < v < 1.00 V s^{-1}, indicating a reversible surface-confined redox process. The corresponding formal potentials were estimated as E_{T-PBI}^0 = 0.790 ± 0.035 V, E_{P-PBI}^0 = 0.725 ± 0.095 V, and E_{Py-PBI}^0 = 0.820 ± 0.010 V. Current integration, after correction of the double-layer contribution and assuming a two-electron transfer process, yields charges of ~20 μC cm^{-2} for all derivatives, which correspond to surface coverage and cross sectional areas of Γ ~ 1.03 × 10^{-10} mol cm^{-2} and A ~ 1.6 nm^2, respectively. These cross-section areas represent densely packed monolayers of the respective PBI derivatives, with the long molecular axis through the two imide nitrogens slightly tilted with respect to the surface normal. A parallel orientation could be ruled out, due to packing reasons.

7.4 Electrochemically Gate-Controlled Conductance of Perylene Bisimide Derivatives

Figure 28a shows a set of typical current–distance traces (i_T-Δz) recorded upon retracting a coated-gold STM tip away from a T-PBI covered Au(111) surface in 0.05 M $LiClO_4$ solution (pH 12). These curves exhibit characteristic single plateaus (dominant) or a series of plateaus separated by current steps. The steps are assigned to the breaking of individual (respectively multi-molecular) junctions of the PBI derivatives previously formed between the Au STM tip and the substrate surface.
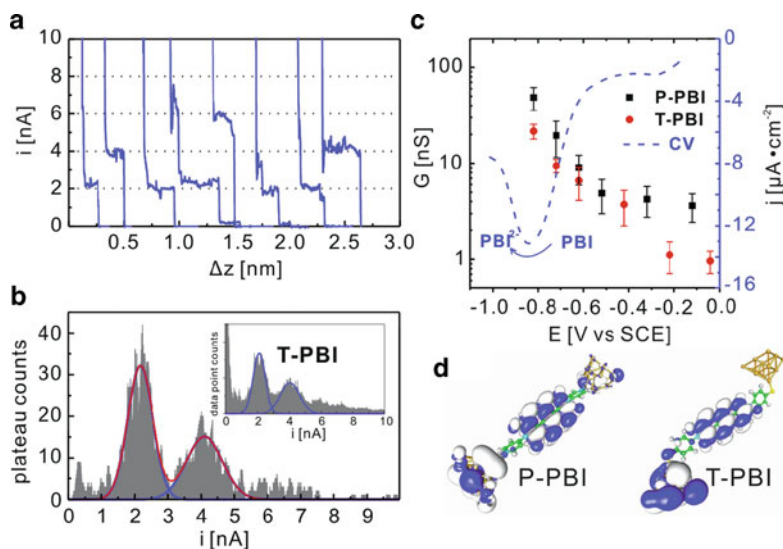
Fig. 28 (**a**) Typical current-distance (i-Δz) retraction curves for T-PBI molecules immobilized on Au(111)-(1 × 1) in 0.05 M LiClO$_4$, pH ~ 12, at E_{bias} = 0.10 V; E_S = 0.82 V (vs SCE). (**b**) Plateau count conductance histogram constructed from individual current–distance curves of T-PBI, 500 selected out of 2,500. The *inset* shows the corresponding all-data-point conductance histogram. (**c**) Single junction conductances of P-PBI and T-PBI in dependence on the substrate potential E_s. The *dashed line* corresponds to the single scan voltammogram recorded for a monolayer of immobilized T-PBI on Au(111)-(1 × 1) in 0.05 M LiClO$_4$, pH ~ 12, scan rate 0.1 V s^{-1}. (**d**) LUMO orbitals of P-PBI and T-PBI molecules attached to Au$_{14}$ clusters (without the bulky *tert*-butyl-phenoxy groups in the bay area) [170]

The statistical analysis of these traces revealed all-data-point and plateau-counting histograms with a series of uniformly spaced current peaks (Fig. 28b). The first peak of each sequence could be identified as the single-junction conductance current. The data set of T-PBI plotted in Fig. 28b leads to 21.7 ± 3.8 nS at E_S = −0.820 V.

The potential dependence of the "Au–P-PBI(T-PBI)–Au" single-junction conductances was obtained at variable substrate (E_S) and tip (E_T) potentials in −0.90 V < E_S (E_T) < 0.00 V, while keeping the bias voltage E_{bias} constant. Figure 28c shows semi-logarithmic plots of the single junctions conductances "Au–P-PBI(T-PBI)–Au" vs the substrate potential E_S. The conductances of P-PBI junctions are typically, i.e., within the entire potential range studied, a factor of 3 larger than those of T-PBI. We also observed that the conductances of both systems are rather independent of the electrode potential in the stability range of the neutral PBI species. Decreasing the substrate and tip potentials toward negative values, and approaching the potential regions of the reduction processes P-PBI|P-PBI$^{\bullet-}$, relative to P-PBI$^{\bullet-}$|P-PBI^{2-} (as for T-PBI), leads to a rapid increase of the junction conductance (up to two orders of magnitude). No plateaus or peaks were observed at $E < -0.90$ V. The recording of reliable data at $E < -0.90$ V is hampered due to the onset of adlayer desorption.

Transport calculations revealed a LUMO-controlled mechanism, with the current flowing through the π-orbitals of the connecting pyridyl/phenyl-units (Fig. 28d). The LUMO hybridization is controlled entirely by how this π-system is connected to the electrodes. With the pyridine coupling there is a direct overlap with the Au-surface states, while in the case of a thiol coupling a mediating S-atom has been introduced. Since the S-levels mix with the benzene π-orbitals only at energies more than 0.5 eV below the Fermi energy, the S-atom constitutes a barrier for the current flow through the LUMO, which expresses itself as a reduced coupling. The coupling of P-PBI to the adjacent electrodes is larger, as compared to T-PBI by ~ 2.6, which scales nicely with the experimentally observed threefold higher junction conductance of the pyridyl-terminated PBI derivative.

7.5 Redox-Mediated Tunneling Current

The above *transport* experiments in a *symmetric* "Au–T-PBI(P-PBI)–Au" junction are complemented by single-molecule *tunneling* experiments [170]. Here, a redox-molecule modified tunneling junction is created, with an *asymmetric* PBI derivative bound chemically either to the Au tip or to the Au(111) substrate surface. After establishing a stable tunneling junction, the STM feedback was switched off, and subsequently the tunneling current i_T was recorded at constant *xyz-* position as a function of the applied voltage, while keeping constant the voltage difference between tip and substrate (bias voltage). In other words, the Fermi levels of tip and substrate were shifted relative to the discrete molecular levels.

Figure 29a shows a typical i_T vs E_S tunneling curve for an "Au–T-PBI–Au" junction, constructed by averaging ten individual traces, $E_{bias} = 0.10$ V. The curve exhibits a pronounced maximum at $E_{max} = -0.740 \pm 0.075$ V, which is close to the formal potential of the surface-confined molecule, $E^0 = -0.790 \pm 0.075$ V, and does not scale with the scan rate v. The full-width-at-half-maximum (FWHM) is estimated as 0.27 ± 0.02 V. The current at the maximum is two orders of magnitude higher than the values at the two turning points $E_S = 0.00$ V and -1.200 V, which represent the stability regions of the neutral T-PBI species or its dianion T-PBI^{2-}, respectively. The large current of the maximum is also significantly higher than the electrochemical background signal (faradaic current, recorded upon retracting the tip in the *z*-direction out of the tunneling regime) and convincingly demonstrates an enhanced tunneling response modulated by the presence of the redox-active T-PBI molecule. The position of the current maximum depends linearly on the applied bias voltage, according to $E_{max} = -0.668$ V$- 0.704 \times E_{bias}$ (Fig. 29b). The FWHM of the tunneling resonance broadens with increasing bias voltage. Clearly the enhanced tunneling current represents the "opening" or "gating" of an additional molecular tunneling channel, which resembles a transistor-like behavior. Due to the sharpness of the tip and the exponential distance dependence of the tunneling signal, the main contribution to the enhanced tunneling signal in
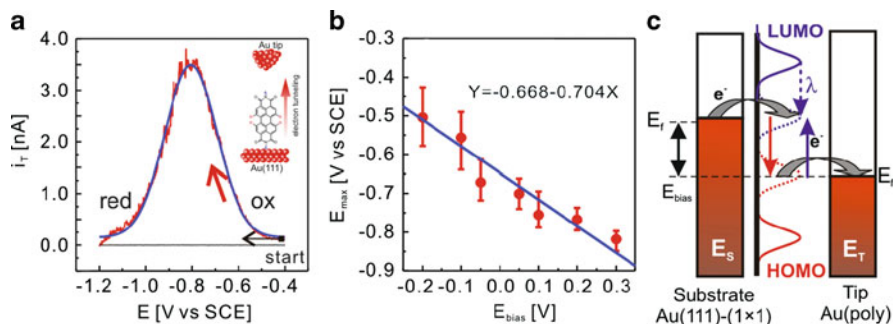
Fig. 29 (**a**) Tunneling current (i_T) vs substrate potential (E_S) trace (*red curve*) recorded in 0.05 M LiClO$_4$ at pH ~ 12 for a monolayer of T-PBI immobilized on Au (111)-(1 × 1). The bias voltage was fixed to 0.10 V. The scan started at $E_S = -0.42$ V, after switching off the tunneling feedback ($i_T = 0.1$ nA), sweep rate 1 V s^{-1}. The *solid blue trace* represents the fitted curve based on (4) with the following parameters: $\lambda_R = 0.22$ eV; $\eta = 0.55$ and $\xi = 0.38$. The *black curve* shows the tip voltammogram when the tip was retracted out of the tunneling regime. (**b**) Bias voltage, E_{bias}, dependence of the position of the maximum in the tunneling current, E_{max}, (**c**) Schematic energy level diagram of a sequential two-step electron transfer process mediated by a redox-active molecule [144, 145, 170]

the asymmetric junction is assumed to originate from a rather small number of redox-active molecules.

A maximum in the tunneling current is predicted by resonance tunneling, a mechanism based on a coherent two-step electron transfer, or a sequential two-(multi-) step electron transfer process (Fig. 29c) [144–147, 265, 266]. The former two regimes imply a shift of the maximum in the tunneling current by the reorganization Gibbs free energy λ_R with respect to the formal potential E^0. A maximum, located close to the formal potential, as observed in the present study, is predicted by the third mechanism. Additional support for this scenario is given by the linear dependence of E_{max} vs E_{bias} (Fig. 29b). Within the limits of low bias voltages E_{bias} and overvoltages $\eta = (E-E^0)$, as well as sufficiently strong molecule-electrode coupling (adiabatic limit), Ulstrup et al. proposed the following theoretical formalism [144–147]:

$$i_T = e\kappa\rho(eE_{bias})\frac{\omega_{eff}}{4\pi}\exp\left(-\frac{e(\lambda_R+E_{bias})}{4k_BT}\right)\left\{\cosh\left[\frac{e}{2k_BT}\left(\xi\eta+\left(\gamma-\frac{1}{2}\right)E_{bias}\right)\right]\right\}^{-1}$$

(4)

with

$$i_T(\eta) = \frac{i_{T\,max}}{\cosh[a(\eta-\eta_{max})]},$$

(5)

$$a = \frac{e\xi}{2k_{\mathrm{B}}T} = 19.4\xi, \qquad (6)$$

and

$$\eta_{\max} = \frac{1}{\xi}\left(\frac{1}{2} - \gamma\right)E_{\mathrm{bias}}. \qquad (7)$$

The reorganization free energy λ_{R} represents the electronic–vibrational coupling, ξ and γ are fractions of the overpotential η and of the bias voltage E_{bias} at the site of the redox center, e is the elementary charge, k_{B} the Boltzmann constant, and ω_{eff} a characteristic nuclear vibration frequency. κ and ρ represent, respectively, the microscopic transmission coefficient and the density of electronic levels in the metal leads, which are assumed to be identical for both the reduction and the oxidation of the intermediate redox group. i_{Tmax} and $\eta_{\max}$ are the current and the overvoltage at the maximum.

The fits of (4)–(7) to the experimental curves plotted in Fig. 29a, b lead to $\lambda_{\mathrm{R}} = 0.22$ eV, $\xi = 0.38$, and $\gamma = 0.55$ [170]. The fits of more than 30 negative and positive going half-cycles yield average parameters $\lambda_{\mathrm{R}} = (0.17 \pm 0.08)$ eV, $\xi = (0.32 \pm 0.08)$, and $\gamma = (0.45 \pm 0.15)$, indicating a substantial potential drop at the position of the redox site. The value of the reorganization energy λ_{R} is reasonable, and strengthens the mechanism proposed. The good coincidence between the fitted and the measured trace provides additional support. A detailed analysis of the theoretical formalism expressed by (4) is given in [110].

The asymmetric tunneling configuration is distinctly different from the symmetric "Au–molecule–Au" configuration. The latter exhibits modifications of the junction conductance with the molecules bound to both leads, due to electronic structure changes of the redox-active unit ("inner-sphere reorganization energy"), while the former exhibits a maximum of the tunneling current due to the coexistence of the oxidized and the reduced forms, with dominant contributions of the dynamics of the solvent molecules in the gap ("outer-sphere reorganization energy"). The observed enhancement of the tunneling current in an electrochemical environment is not restricted to perylene-type junctions. It has also been observed for other redox systems, such as viologens [34, 110, 155], ferrocene [150], redox-proteins [109, 172, 174], and very recently for a hydroquinone derivative chemically bound to a gold electrode [175].

8 Quantized Charging of Nanometer-Sized Gold Clusters

Metal nanoparticles (NPs), which represent an important family of nanoscale objects with unique electronic, optical, catalytic, and magnetic properties, are distinctly different from both molecular and bulk materials. In the following we

address recent studies on quantized charging of individual (local approach) and larger numbers of gold nanoclusters (macroscopic approach), in particular monolayer protected nanoclusters (MPC), in both ionic liquid and aqueous electrolyte.

8.1 Introduction

The electronic and electrochemical properties of metal nanoparticles (NP) can be tuned through the metal core and the ligand shell. Depending on the core size of the NPs [or monolayer-protected clusters (MPC), see Fig. 30a], one may distinguish between bulk continuum (core diameter$\gg$ 3–4 nm), quantized double-layer charging, and molecule-like charging (<1.5 nm) [336, 337]. In addition, the energetics of electron uptake to an MPC is determined by three different energy scales [338]. Quantum confinement is manifested in the spacing of electron levels ΔE, such as between HOMO and LUMO energy levels. Furthermore, in small crystals,
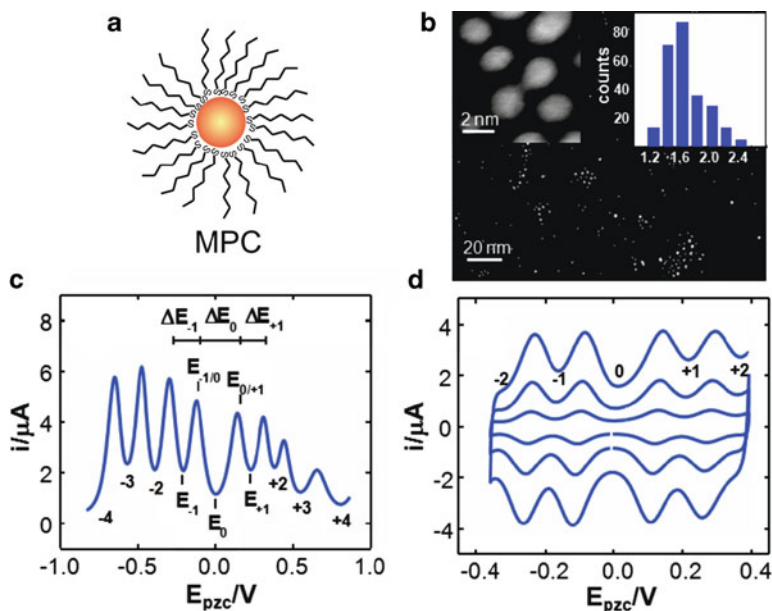

Fig. 30 (**a**) Schematic representation of an alkanedithiol monolayer protected cluster, MPC. (**b**) High resolution TEM image together with a core diameter distribution histogram for the $Au_{144}C6S$ MPC used. (**c**) Differential pulse voltammogram of a drop-cast $Au_{144}C6S$ film formed on a Pt electrode in ionic liquid (HMImFET). Pulse width 60 ms, pulse height 50 mV, period 200 ms, scan rate 20 mV s^{-1}, scan direction negative to positive. For the zero and plus/minus one charge states, relevant potentials, E, and stability regions, ΔE, have been indicated. For conciseness, all other regions are indentified by the assigned charge states z only. (**d**) Cyclic voltammograms of a drop-cast $Au_{145}C6S$ film formed on a Pt electrode in BMPyFSI, for charge states $|z| < 2$ as indicated. Scan rate 20, 50, 100 mV s^{-1} (inner to outer traces) [334, 335]

Coulomb repulsion between the added electrons results in a considerable energy cost E_C. The third relevant energy scale is $k_B T$. If ΔE and E_C are both smaller than $k_B T$, the behavior is bulk continuum-like. In metal nanocrystals with core-size diameters ranging between 1.5 nm and 3 ~ 4 nm, E_C is often considerably larger than either ΔE or $k_B T$. Their charging state response is then determined by the Coulomb blockade. In very small metal clusters and semiconductor NPs, both ΔE and E_C are smaller than $k_B T$. In consequence, discrete and molecule-like electronic energy levels are accessible upon charging. We notice that metal particles do not show quantum confinement effects comparable to semiconductor quantum dots, unless their core diameter is smaller than 1.5 nm. However, due to the sub-attofarad capacitance (aF $= 10^{-18}$ F) of MPCs (C_{MPC}), the electrostatic energy required to add an electron, E_C, substantially exceeds the thermal energy at room temperature (RT). This means that the charge of the core can be controlled, and discrete electron transfer is observed. In the presence of a sufficiently concentrated electrolyte, to neglect diffuse-layer contributions, the classical concentric spheres capacitor formula provides a good first approximation of the MPC capacitance [339, 340]:

$$C_{MPC} = 4\pi\varepsilon\varepsilon_0 \frac{r(r+d)}{d},$$ (8)

where ε_0 is the permittivity in vacuum, ε the static dielectric constant of the ligand shell, d its thickness, and r the radius of the gold core.

For perfect monodisperse MPC, a succession of regularly spaced charging peaks is expected as the potential is varied:

$$\Delta E_z = \frac{e}{C_{MPC}}.$$ (9)

The subscript z refers to the charge state of the cluster, i.e., the sign and the number of one-electron charges stored on the MPC core; ΔE_z is then the potential range where the charge state z is stable.

In conclusion, for larger core diameters, electron addition/removal is a purely capacitive phenomenon, while for sub-nanometer core diameters, the energies are determined both by the spacing of the molecular energy levels and the capacitive charging. C_{MPC}, which is typically in the sub-attofarad range, determines the charging energy, and can be estimated from electrochemical measurements, such as differential pulse voltammetry (DPV), from the potential spacing between successive electron transfers ΔE_z. [341]

8.2   Quantized Charging on Macroscopic Electrodes

Murray et al. demonstrated in two seminal contributions that freely diffusing, monodisperse hexanethiol-capped 1.6-nm Au-NPs (~Au_{145}) exhibit sequential

charging in electrochemical experiments at room temperature, employing cyclic voltammetry or DPV [341, 342]. Quinn et al. [343] and Mertens et al. [334, 335] improved the monodispersity in terms of size and composition. Both groups observed 15 separated charging peaks, each corresponding to single-electron transfers between diffusing MPC and a metal electrode. The peaks can be rationalized by quantized double-layer charging of the MPC in the electrolyte solution near the electrode surface, with the MPC viewed as a multivalent "redox species" [344, 345]. Murray et al. demonstrated that the charge state of the NPs can be tuned by varying the electrode potential, and that the charged NPs retained most of their charge upon removal from the solution and re-dissolution [346]. A number of studies have investigated the influence of capping ligand (layer thickness, chemical structure), electrolyte, and temperature [123, 347]. Hicks et al. demonstrated that the NPs capacitance can be modeled as the capacitance of two concentric conducting spheres separated by a dielectric [348]. The model was extended by Quinn et al. [337] and Su et al. [349], both taking medium effects into account.

Summarizing, the energetics of MPC (with a core size ranging between ~1 nm and 3–4 nm) charging in solution are determined by the capacitance. It is primarily a function of core size and the nature of the protecting monolayer. However, the capacitance can be significantly altered by medium effects, such as solvent and electrolyte ions.

Quantized double-layer charging was also observed with immobilized mono- [350] and multi-layer [351] assemblies of NPs on solid substrates, employing covalent or electrostatic linking procedures ([336, 347] and literature cited therein). Potential spacing ΔE_z and the NP capacitance in low-polarity electrolytes were found to be similar to the data from bulk-solution experiments. The charging response in high-polarity solvents, such as aqueous electrolytes, was distinctly different: ΔE_z was smaller and an ion-induced rectification was observed. This phenomenon was tentatively attributed to a coupled ion-transfer and electron-transfer process [337]. However, this hypothesis is still not yet proven. Redox- or otherwise active groups could be introduced, upon modification of the particles ligand shell, by kinetically controlled place-exchange reactions. [352].

We have recently synthesized monodisperse hexanethiolate-protected gold clusters, Au_{144}-C6S, and determined an average core diameter of 1.7 ± 0.3 nm, in support of the estimated molecular formula Au_{144}-$(C_6H_{11}S)_{52}$ (Fig. 30b) [334].

Solution-phase DPV of Au_{144}-C_6S dispersed in 10 mM [bis(triphenylpho-sphoranylidene)-ammoniumtetrakis-(pentafluorophenyl)-borate (BTPPATPFB)/ toluene]:[acetonitrile] 2:1 revealed well-behaved, equally spaced and symmetric quantized double-layer charging peaks with $\Delta E \sim 0.270 \pm 0.010$ V. Applying the classical concentric spheres capacitor model (8) reveals an individual cluster capacitance of ~0.6 aF [334, 335].

Immobilization of these clusters on Pt(hkl) surfaces, employing bifunctional linkers with one pyridyl- and one thiol-based anchoring group, was achieved [334, 335]. The terminal pyridyl anchor ensures a strong chemical bond to the

Pt(hkl) substrate, while the thiol is attached to the NP via ligand exchange [353], which could be characterized in aqueous and organic electrolytes.

We have also demonstrated that well-behaved quantized charging of gold MPCs is possible in air- and water-stable room-temperature ionic liquids, such as 1-hexyl-3-methylimidazolium tris(penta-fluoroethyl)-trifluorophosphate (HMImFEP), Fig. 30c, d [334, 335]. As ionic liquids have very attractive features, including near-zero vapor pressure, considerable thermal stability, and an electrochemical stability window that often exceeds 4 V, this demonstration is particularly significant from a technological point of view.

8.3 Quantized Charging of Individual Nanoclusters

Single-electron Coulomb charging was observed for different types and sizes of individual metal NPs in vacuum or in air, employing specifically STM and STS [24, 39, 353–355]. Albrecht et al. showed in a proof-of-principle experiment the possibility of intrinsic multi-state switching of Au nanoclusters through electrochemical gating [123]. Motivated by this pioneering report, we created a ferrocenethiol-based self-assembled template monolayer on Au(111) electrodes with immobilized and uniformly-distributed gold clusters of 2.4 ± 0.5 nm diameter and a rather narrow size distribution (Fig. 31a) [150].

We carried out a series of systematic constant-bias-mode in situ STS experiments, with the gold tip positioned above a single gold cluster. We observed for the cluster-modified junctions up to seven clearly resolved narrow peaks in the tunneling current i_T plotted vs the substrate potential E_S (I_T versus E_S characteristics, Fig. 31b [150]). These data were analyzed by fitting a series of Gaussians to distinguish individual peaks, and to determine their positions, heights, and widths. An example is presented in Fig. 31b. The peak-to-peak spacing in the current–voltage curves, based on a statistical analysis of 73 individual traces, was found to be very regular (Fig. 31d) and equal to $\Delta E = 0.11 \pm 0.02$ V. The FWHM is also rather uniform, and amounts to 0.07 ± 0.03 V. On the other hand, we observed that the measured heights of the individual peaks vary by two orders of magnitude, and are distributed exponentially with a decay factor of ~0.5 nA. We noted that these regularly-spaced peaks were positioned on both sides of the formal potential of the ferrocene-driven redox process, e.g., at $E \approx E^0 = 0.51$ V. The heights of these peaks typically decrease with distance from E^0. In an attempt to generalize these observations, we constructed two-dimensional peak-position vs peak-height distributions based on all experimental data accessible. The plot in Fig. 31c clearly supports the trend formulated above. On the basis of the distribution of peak spacings and peak heights, we attribute our observations to a modulation of the tunneling current enhancement in the redox-active tunneling junction by a sequential capacitive charging of single gold nanoclusters. Following this hypothesis, we estimate [336, 339, 340, 344] the average single-particle capacitance as $C \approx e/\Delta E = 1.5 \pm 0.2$ aF.
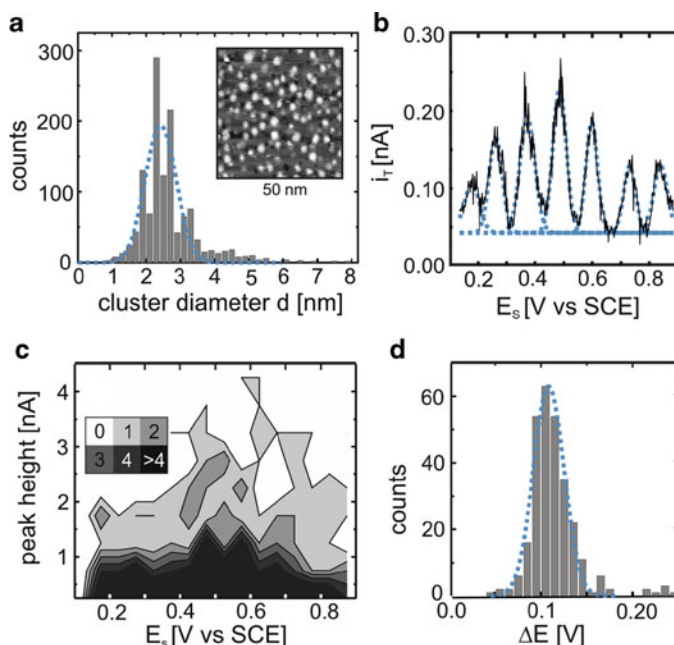
Fig. 31 (**a**) STM image ($i_T = 0.05$ nA, $E_S = 0.7$ V, $E_T = 0.1$ V; vertical scale 0.4 nm) and size distribution histogram of gold nanoclusters formed with a self-assembled template monolayer on Au (111) in 1.0 M $HClO_4$. The *dotted line* represents the Gaussian fit. The corresponding parameters are the average cluster diameter of 2.4 nm and the standard deviation $\sigma = 0.45$ nm. (**b**) Example of a constant bias current–voltage response of a single gold cluster as triggered by "electrolyte gating", $E_{bias} = 0.10$ V, $i_T = 0.05$ nA. The *dotted traces* represent its fit by a series of Gaussians. (**c**) Contour map of peak position vs peak height distribution for 361 peaks. The various shadings indicate areas with different amounts of counts per cell (0.05 V × 0.5 nA) inside. (**d**) Peak spacing histogram and Gaussian fit for a data set 361 individual traces, such as shown in (**c**). The corresponding parameter are the average spacing $\Delta E = 0.11$ V and $\sigma = 0.017$ V [150]

Our study and the work of Albrecht et al. [123] reported, as a unique result, peak-shaped modulations of the tunneling current. The peaks are equally spaced, as well as rather close and narrow. This offers new perspectives on multistate electronic switching in condensed media at room temperature. The observed feature of sequential capacitive charging is reminiscent of a successive charging of multi-valent redox molecules through several oxidation/reduction states. However, the latter are usually much wider than the former, and limited to a rather small number of individual states. The interplay of this redox resonance with the sequential charging of Au NPs in an individual electrochemical tunneling junction has not yet been treated theoretically, although the Coulomb charging effect under electro-chemical conditions in a multistate redox molecule was recently addressed. The results seem to be in agreement with our observations. However, we believe that an appropriate model will need to consider the successive charging of the particle Coulomb levels in combination with the solvent activation and relaxation, as modified by the redox-active host lattice [150, 334, 335].

9 Conclusions and Outlook

Employing an STM-BJ technique in various condensed phases, charge transport properties through nanoscale objects at an electrified solid–liquid interface were addressed. In particular, the following representative systems were discussed in more detail: gold atomic contacts, alkanedithiols, biphenyl derivatives, 4,4'-bipyridine, redox-active perylene bisimides, and surface-immobilized gold clusters. The experimental investigation of these examples, together with quantum chemistry and transport calculations, provide a detailed understanding of selected fundamental relationships between molecular structure and conductance properties of nanostructures upon polarization in a confined space. The uniqueness of the concept of "electrolyte gating" to modulate charge transport at the nanoscale in condensed media and at room temperature was demonstrated. In particular, the addressing of the intrinsic electronic properties of single redox-active molecules and gold clusters was presented. These conceptual studies open up fascinating perspectives toward novel applications, such as multistate electronic switching, current amplification, rectification, and other electronics functions at the nanoscale.

Further development, beyond the current state of the art, relies on a higher diversity and reliability of experimental techniques and functionalized systems, as well as on the identification of nanoscale signatures, which will continuously inspire many physicists, chemists, biologists, and engineers. Examples include the construction of functional 3D architectures based on 2D templates, the combination of local spectroscopy (IR, Raman) with transport problems, the creation of organic–inorganic hybrid structures by rational combination of organic synthesis with inorganic platforms, such as carbon- and/or silicon-based materials, and the implementation of soft electronics (molecular basis and condensed medium) into hard electronics (conventional semiconductor-based micro-fabrication). It is our belief that the field of nano- and molecular-based electronics will continue growing as a highly innovative interdisciplinary science, which has a significant influence on various other scientific and engineering areas.

References

1. Aviram A, Ratner MA (1974) Chem Phys Lett 29:277
2. Cuevas JC, Scheer E (2010) Molecular electronics: an introduction to theory and experiment. World Scientific, Singapore
3. Tour JM (2003) Molecular electronics: commercial insights, chemistry, architecture and programming. World Scientific, Singapore
4. Joachim C, Gimzewski JK, Aviram A (2000) Nature 408:541

5. Nitzan A, Ratner MA (2003) Science 300:1384
6. Heath JR, Ratner MA (2003) Phys Today 56:43
7. Joachim C, Ratner MA (2005) Proc Natl Acad Sci USA 102:8801
8. Carroll RL, Gorman CB (2002) Angew Chem Int Ed 41:4379
9. Lindsay SM, Ratner MA (2007) Adv Mater 19:23
10. Salomon A, Cahen D, Lindsay S, Tomfohr J, Engelkes VB, Frisbie CD (2003) Adv Mater 15:1881
11. Tao NJ (2006) Nat Nanotechnol 1:173
12. Ulgut B, Abruna HD (2008) Chem Rev 108:2721
13. Metzger RM (2008) J Mater Chem 18:4364
14. Selzer Y, Allara DL (2006) Annu Rev Phys Chem 57:593
15. Heath JR (2009) Annu Rev Mater Res 39:1
16. van der Molen SJ, Liljeroth P (2010) J Phys Condens Matter 22:133001
17. James DK, Tour JM (2004) Chem Mater 16:4423
18. McCreery RL (2004) Chem Mater 16:4477
19. Chen F, Hihath J, Huang ZF, Li XL, Tao NJ (2007) Annu Rev Phys Chem 58:535
20. Akkerman HB, de Boer B (2008) J Phys Condens Matter 20:013001
21. Kroger J, Neel N, Limot L (2008) J Phys Condens Matter 20:22301
22. Haick H, Cahen D (2008) Prog Surf Sci 83:217
23. Nichols RJ, Haiss W, Higgins SJ, Leary E, Martin S, Bethell D (2010) Phys Chem Chem Phys 12:2801
24. Andres RP, Bein T, Dorogi M, Feng S, Henderson JI, Kubiak CP, Mahoney W, Osifchin RG, Reifenberger R (1996) Science 272:1323
25. Gimzewski JK, Joachim C (1999) Science 283:1683
26. Donhauser ZJ, Mantooth BA, Kelly KF, Bumm LA, Monnell JD, Stapleton JJ, Price DW, Rawlett AM, Allara DL, Tour JM, Weiss PS (2001) Science 292:2303
27. Repp A, Meyer G, Paavilainen S, Olsson FE, Persson M (2006) Science 312:1196
28. Cui XD, Primak A, Zarate X, Tomfohr J, Sankey OF, Moore AL, Moore TA, Gust D, Harris G, Lindsay SM (2001) Science 294:571
29. Wold DJ, Haag R, Rampi MA, Frisbie CD (2002) J Phys Chem B 106:2813
30. Fan FRF, Yang JP, Cai LT, Price DW, Dirk SM, Kosynkin DV, Yao YX, Rawlett AM, Tour JM, Bard AJ (2002) J Am Chem Soc 124:5550
31. Tao NJ (1996) Phys Rev Lett 76:4066
32. Xu BQ, Tao NJJ (2003) Science 301:1221
33. Haiss W, van Zalinge H, Higgins SJ, Bethell D, Hobenreich H, Schiffrin DJ, Nichols RJ (2003) J Am Chem Soc 125:15294
34. Li Z, Han B, Meszaros G, Pobelov I, Wandlowski T, Blaszczyk A, Mayor M (2006) Faraday Discuss 131:121
35. Dadosh T, Gordin Y, Krahne R, Khivrich I, Mahalu D, Frydman V, Sperling J, Yacoby A, Bar-Joseph I (2005) Nature 436:677
36. Liao JH, Bernard L, Langer M, Schonenberger C, Calame M (2006) Adv Mater 18:2803
37. Reed MA, Zhou C, Muller CJ, Burgin TP, Tour JM (1997) Science 278:252
38. Kergueris C, Bourgoin JP, Palacin S, Esteve D, Urbina C, Magoga M, Joachim C (1999) Phys Rev B 59:12505
39. Reichert J, Ochs R, Beckmann D, Weber HB, Mayor M, Lohneysen HV (2002) Phys Rev Lett 88:176804
40. Gonzalez MT, Wu SM, Huber R, van der Molen SJ, Schonenberger C, Calame M (2006) Nano Lett 6:2238
41. Lortscher E, Ciszek JW, Tour J, Riel H (2006) Small 2:973
42. Park J, Pasupathy AN, Goldsmith JI, Chang C, Yaish Y, Petta JR, Rinkoski M, Sethna JP, Abruna HD, McEuen PL, Ralph DC (2002) Nature 417:722
43. Osorio EA, Bjornholm T, Lehn JM, Ruben M, van der Zant HSJ (2008) J Phys Condens Matter 20:374121

44. Seferos DS, Trammell SA, Bazan GC, Kushmerick JG (2005) Proc Natl Acad Sci USA 102:8821
45. Chen J, Reed MA, Rawlett AM, Tour JM (1999) Science 286:1550
46. Tran E, Duati M, Whitesides GM, Rampi MA (2006) Faraday Discuss 131:197
47. Seminario JM, Zacarias AG, Tour JM (1999) J Am Chem Soc 121:411
48. Venkataraman L, Klare JE, Nuckolls C, Hybertsen MS, Steigerwald ML (2006) Nature 442:904
49. Venkataraman L, Klare JE, Tam IW, Nuckolls C, Hybertsen MS, Steigerwald ML (2006) Nano Lett 6:458
50. Wang CS, Batsanov AS, Bryce MR, Martin S, Nichols RJ, Higgins SJ, Garcia-Suarez VM, Lambert CJ (2009) J Am Chem Soc 131:15647
51. Kamenetska M, Quek SY, Whalley AC, Steigerwald ML, Choi HJ, Louie SG, Nuckolls C, Hybertsen MS, Neaton JB, Venkataraman L (2010) J Am Chem Soc 132:6817
52. Kim B, Beebe JM, Jun Y, Zhu XY, Frisbie CD (2006) J Am Chem Soc 128:4970
53. Kiguchi M, Miura S, Hara K, Sawamura M, Murakoshi K (2006) Appl Phys Lett:89
54. Mishchenko A, Zotti L, Vonlathen D, Bürkle M, Pauly F, Cuevas JC, Mayor M, Wandlowski Th (2010) J Am Chem Soc 133:184
55. Ko CH, Huang MJ, Fu MD, Chen CH (2010) J Am Chem Soc 132:756
56. Park YS, Widawsky JR, Kamenetska M, Steigerwald ML, Hybertsen MS, Nuckolls C, Venkataraman L (2009) J Am Chem Soc 131:10820
57. Taniguchi M, Tsutsui M, Shoji K, Fujiwara H, Kawai T (2009) J Am Chem Soc 131:14146
58. Yasuda S, Yoshida S, Sasaki J, Okutsu Y, Nakamura T, Taninaka A, Takeuchi O, Shigekawa H (2006) J Am Chem Soc 128:7746
59. Chen F, Li XL, Hihath J, Huang ZF, Tao NJ (2006) J Am Chem Soc 128:15874
60. Martin S, Haiss W, Higgins S, Cea P, Lopez MC, Nichols RJ (2008) J Phys Chem C 112:3941
61. Park YS, Whalley AC, Kamenetska M, Steigerwald ML, Hybertsen MS, Nuckolls C, Venkataraman L (2007) J Am Chem Soc 129:15768
62. Xing YJ, Park TH, Venkatramani R, Keinan S, Beratan DN, Therien MJ, Borguet E (2010) J Am Chem Soc 132:7946
63. Martin CA, Ding D, Sorensen JK, Bjornholm T, van Ruitenbeek JM, van der Zant HSJ (2008) J Am Chem Soc 130:13198
64. Li C, Pobelov I, Wandlowski T, Bagrets A, Arnold A, Evers F (2008) J Am Chem Soc 130:318
65. Haiss W, Wang CS, Grace I, Batsanov AS, Schiffrin DJ, Higgins SJ, Bryce MR, Lambert CJ, Nichols RJ (2006) Nat Mater 5:995
66. Kamenetska M, Koentopp M, Whalley AC, Park YS, Steigerwald ML, Nuckolls C, Hybertsen MS, Venkataraman L (2009) Phys Rev Lett 102:126803
67. Wu SM, Gonzalez MT, Huber R, Grunder S, Mayor M, Schonenberger C, Calame M (2008) Nat Nanotechnol 3:569
68. Chang S, He J, Kibel A, Lee M, Sankey O, Zhang P, Lindsay S (2009) Nat Nanotechnol 4:297
69. Huber R, Gonzalez MT, Wu S, Langer M, Grunder S, Horhoiu V, Mayor M, Bryce MR, Wang CS, Jitchati R, Schonenberger C, Calame M (2008) J Am Chem Soc 130:1080
70. Choi SH, Kim B, Frisbie CD (2008) Science 320:1482
71. Leary E, Higgins SJ, van Zalinge H, Haiss W, Nichols RJ (2007) Chem Commun 38:3939
72. Venkataraman L, Park YS, Whalley AC, Nuckolls C, Hybertsen MS, Steigerwald ML (2007) Nano Lett 7:502
73. Hybertsen MS, Venkataraman L, Klare JE, Whalley CA, Steigerwald ML, Nuckolls C (2008) J Phys Condens Matter 20:374115
74. Haiss W, Wang CS, Jitchati R, Grace I, Martin S, Batsanov AS, Higgins SJ, Bryce MR, Lambert CJ, Jensen PS, Nichols RJ (2008) J Phys Condens Matter 20:374119
75. Vonlanthen D, Mishchenko A, Elbing M, Neuburger M, Wandlowski T, Mayor M (2009) Angew Chem Int Ed 48:8886

76. Mishchenko A, Vonlanthen D, Meded V, Burkle M, Li C, Pobelov IV, Bagrets A, Viljas JK, Pauly F, Evers F, Mayor M, Wandlowski T (2010) Nano Lett 10:156
77. Diez-Perez I, Hihath J, Lee Y, Yu LP, Adamska L, Kozhushner MA, Oleynik II, Tao NJ (2009) Nat Chem 1:635
78. Ashwell GJ, Sujka M, Green A (2006) Faraday Discuss 131:23
79. Elbing M, Ochs R, Koentopp M, Fischer M, von Hanisch C, Weigend F, Evers F, Weber HB, Mayor M (2005) Proc Natl Acad Sci USA 102:8815
80. Salomon A, Arad-Yellin R, Shanzer A, Karton A, Cahen D (2004) J Am Chem Soc 126:11648
81. Guisinger NP, Greene ME, Basu R, Baluch AS, Hersam MC (2004) Nano Lett 4:55
82. Collier CP, Wong EW, Belohradsky M, Raymo FM, Stoddart JF, Kuekes PJ, Williams RS, Heath JR (1999) Science 285:391
83. Luo Y, Collier CP, Jeppesen JO, Nielsen KA, DeIonno E, Ho G, Perkins J, Tseng HR, Yamamoto T, Stoddart JF, Heath JR (2002) ChemPhysChem 3:519
84. Duan XF, Huang Y, Lieber CM (2002) Nano Lett 2:487
85. Blum AS, Kushmerick JG, Long DP, Patterson CH, Yang JC, Henderson JC, Yao YX, Tour JM, Shashidhar R, Ratna BR (2005) Nat Mater 4:167
86. Liao JH, Agustsson JS, Wu SM, Schonenberger C, Calame M, Leroux Y, Mayor M, Jeannin O, Ran YF, Liu SX, Decurtins S (2010) Nano Lett 10:759
87. Song H, Kim Y, Jang YH, Jeong H, Reed MA, Lee T (2009) Nature 462:1039
88. Reddy P, Jang SY, Segalman RA, Majumdar A (2007) Science 315:1568
89. Kubatkin S, Danilov A, Hjort M, Cornil J, Bredas JL, Stuhr-Hansen N, Hedegard P, Bjornholm T (2003) Nature 425:698
90. White HS, Kittlesen GP, Wrighton MS (1984) J Am Chem Soc 106:5375
91. Meulenkamp EA (1999) J Phys Chem B 103:7831
92. Kruger M, Buitelaar MR, Nussbaumer T, Schonenberger C, Forro L (2001) Appl Phys Lett 78:1291
93. Rosenblatt S, Yaish Y, Park J, Gore J, Sazonova V, McEuen PL (2002) Nano Lett 2:869
94. Repp J, Meyer G, Stojkovic SM, Gourdon A, Joachim C (2005) Phys Rev Lett 94:026803
95. Stipe BC, Rezaei MA, Ho W (1998) Science 280:1732
96. Heinrich AJ, Lutz CP, Gupta JA, Eigler DM (2002) Science 298:1381
97. Liljeroth P, Repp J, Meyer G (2007) Science 317:1203
98. Bumm LA, Arnold JJ, Cygan MT, Dunbar TD, Burgin TP, Jones L, Allara DL, Tour JM, Weiss PS (1996) Science 271:1705
99. Mantooth BA, Weiss PS (2003) Proc IEEE 91:1785
100. Weiss PS (2008) Acc Chem Res 41:1772
101. Love JC, Estroff LA, Kriebel JK, Nuzzo RG, Whitesides GM (2005) Chem Rev 105:1103
102. Jackel F, Watson MD, Mullen K, Rabe JP (2004) Phys Rev Lett 92:188303
103. Puigmarti-Luis J, Minoia A, Uji-i H, Rovira C, Cornil J, De Feyter S, Lazzaroni R, Amabilino DB (2006) J Am Chem Soc 128:12602
104. Stabel A, Herwig P, Mullen K, Rabe JP (1995) Angew Chem Int Ed 34:1609
105. Gesquiere A, De Feyter S, De Schryver FC, Schoonbeek F, van Esch J, Kellogg RM, Feringa BL (2001) Nano Lett 1:20
106. Poirier GE (1997) Chem Rev 97:1117
107. Fabre B (2010) Acc Chem Res 43:1509
108. Della Pia A, Chi Q, Jones DD, Macdonald JE, Ulstrup J, Eliott M (2010) Nano Lett. doi: 10.1021/nl10333aq
109. Chi QJ, Farver O, Ulstrup J (2005) Proc Natl Acad Sci USA 102:16203
110. Pobelov IV, Li ZH, Wandlowski T (2008) J Am Chem Soc 130:16045
111. Ye T, Kumar AS, Saha S, Takami T, Huang TJ, Stoddart JF, Weiss PS (2010) ACS Nano 4:3697
112. Moore AM, Dameron AA, Mantooth BA, Smith RK, Fuchs DJ, Ciszek JW, Maya F, Yao YX, Tour JM, Weiss PS (2006) J Am Chem Soc 128:1959

113. Chen F, He J, Nuckolls C, Roberts T, Klare JE, Lindsay S (2005) Nano Lett 5:503
114. Li ZH, Pobelov I, Han B, Wandlowski T, Blaszczyk A, Mayor M (2007) Nanotechnology 18:044018
115. Fujihira M, Suzuki M, Fujii S, Nishikawa A (2006) Phys Chem Chem Phys 8:3876
116. Ulrich J, Esrail D, Pontius W, Venkataraman L, Millar D, Doerrer LH (2006) J Phys Chem B 110:2462
117. Jang SY, Reddy P, Majumdar A, Segalman RA (2006) Nano Lett 6:2362
118. Wierzbinski E, Slowinski K (2006) Langmuir 22:5205
119. Sek S, Misicka A, Swiatek K, Maicka E (2006) J Phys Chem B 110:19671
120. Wold DJ, Frisbie CD (2001) J Am Chem Soc 123:5549
121. Morita T, Lindsay S (2007) J Am Chem Soc 129:7262
122. Cervera J, Mafe S (2010) ChemPhysChem 11:1654
123. Albrecht T, Mertens SFL, Ulstrup J (2007) J Am Chem Soc 129:9162
124. Meszaros G, Kronholz S, Karthauser S, Mayer D, Wandlowski T (2007) Appl Phys A 87:569
125. Li CZ, Bogozi A, Huang W, Tao NJ (1999) Nanotechnology 10:221
126. Holliday BJ, Mirkin CA (2001) Angew Chem Int Ed 40:2022
127. Park SJ, Taton TA, Mirkin CA (2002) Science 295:1503
128. Yi ZW, Trellenkamp S, Offenhausser A, Mayer D (2010) Chem Commun 46:8014
129. Guo XF, Small JP, Klare JE, Wang YL, Purewal MS, Tam IW, Hong BH, Caldwell R, Huang LM, O'Brien S, Yan JM, Breslow R, Wind SJ, Hone J, Kim P, Nuckolls C (2006) Science 311:356
130. Feldman AK, Steigerwald ML, Guo XF, Nuckolls C (2008) Acc Chem Res 41:1731
131. Amlani I, Rawlett AM, Nagahara LA, Tsui RK (2002) Appl Phys Lett 80:2761
132. van der Molen SJ, Liao JH, Kudernac T, Agustsson JS, Bernard L, Calame M, van Wees BJ, Feringa BL, Schonenberger C (2009) Nano Lett 9:76
133. He J, Forzani ES, Nagahara LA, Tao NJ, Lindsay S (2008) J Phys Condens Matter 20:374120
134. Agrait N, Yeyati AL, van Ruitenbeek JM (2003) Phys Rep 377:81
135. van Ruitenbeek JM, Alvarez A, Pineyro I, Grahmann C, Joyez P, Devoret MH, Esteve D, Urbina C (1996) Rev Sci Instrum 67:108
136. Moreland J, Ekin JW (1985) J Appl Phys 58:3888
137. Muller CJ, Vanruitenbeek JM, Dejongh LJ (1992) Phys Rev Lett 69:140
138. Gruter L, Gonzalez MT, Huber R, Calame M, Schonenberger C (2005) Small 1:1067
139. Grunder S, Huber R, Wu SM, Schonenberger C, Calame M, Mayor M (2010) Chimia 64:140
140. Gimzewski JK, Moller R (1987) Phys Rev B 36:1284
141. Xu BQ, Xiao XY, Yang XM, Zang L, Tao NJ (2005) J Am Chem Soc 127:2386
142. Mishchenko A, Li C, Hong W (2011) Small (in preparation)
143. Halbritter A, Makk P, Mackowiak S, Csonka S, Wawrzynizk M, Martinek J (2010) arXiv/1006.1811:1
144. Zhang J, Chi Q, Kuznetsov AM, Hansen AG, Wackerbarth H, Christensen HEM, Andersen JET, Ulstrup J (2002) J Phys Chem B 106:1131
145. Zhang JD, Kuznetsov AM, Medvedev IG, Chi QJ, Albrecht T, Jensen PS, Ulstrup J (2008) Chem Rev 108:2737
146. He HX, Zhu JS, Tao NJ, Nagahara LA, Amlani I, Tsui R (2001) J Am Chem Soc 123:7730
147. Kuznetsov AM, Medvedev IG, Ulstrup J (2007) J Chem Phys 127:104708
148. Hulea IN, Brom HB, Houtepen AJ, Vanmaekelbergh D, Kelly JJ, Meulenkamp EA (2004) Phys Rev Lett 93:166601
149. Tian JH, Yang Y, Zhou XS, Schollhorn B, Maisonhaute E, Chen ZB, Yang FZ, Chen Y, Amatore C, Mao BW, Tian ZQ (2010) ChemPhysChem 11:2745
150. Li ZH, Liu YQ, Mertens SFL, Pobelov IV, Wandlowski T (2010) J Am Chem Soc 132:8187
151. Di Ventra M, Pantelides ST, Lang ND (2000) Appl Phys Lett 76:3448
152. Di Ventra A, Lang ND, Pantelides ST (2002) Chem Phys 281:189
153. Han WH, Durantini EN, Moore TA, Moore AL, Gust D, Rez P, Leatherman G, Seely GR, Tao NJ, Lindsay SM (1997) J Phys Chem B 101:10719

154. Haiss W, Albrecht T, van Zalinge H, Higgins SJ, Bethell D, Hobenreich H, Schiffrin DJ, Nichols RJ, Kuznetsov AM, Zhang J, Chi Q, Ulstrup J (2007) J Phys Chem B 111:6703
155. Leary E, Higgins SJ, van Zalinge H, Haiss W, Nichols RJ, Nygaard S, Jeppesen JO, Ulstrup J (2008) J Am Chem Soc 130:12204
156. He J, Chen F, Lindsay S, Nuckolls C (2007) Appl Phys Lett 90:072112
157. Xu BQQ, Li XLL, Xiao XYY, Sakaguchi H, Tao NJJ (2005) Nano Lett 5:1491
158. Albrecht T, Guckian A, Ulstrup J, Vos JG (2005) Nano Lett 5:1451
159. Albrecht T, Moth-Poulsen K, Christensen JB, Guckian A, Bjornholm T, Vos JG, Ulstrup J (2005) Faraday Discuss:265
160. Albrecht T, Moth-Poulsen K, Christensen JB, Hjelm J, Bjornholm T, Ulstrup J (2006) J Am Chem Soc 128:6574
161. Albrecht T, Guckian A, Kuznetsov AM, Vos JG, Ulstrup J (2006) J Am Chem Soc 128:17132
162. Seo K, Konchenko AV, Lee J, Bang GS, Lee H (2008) J Am Chem Soc 130:2553
163. Ricci AM, Calvo EJ, Martin S, Nichols RJ (2010) J Am Chem Soc 132:2494
164. Visoly-Fisher I, Daie K, Terazono Y, Herrero C, Fungo F, Otero L, Durantini E, Silber JJ, Sereno L, Gust D, Moore TA, Moore AL, Lindsay SM (2006) Proc Natl Acad Sci USA 103:8686
165. Xiao XY, Nagahara LA, Rawlett AM, Tao NJ (2005) J Am Chem Soc 127:9235
166. He J, Fu Q, Lindsay S, Ciszek JW, Tour JM (2006) J Am Chem Soc 128:14828
167. Wassel RA, Credo GM, Fuierer RR, Feldheim DL, Gorman CB (2004) J Am Chem Soc 126:295
168. Xiao XY, Brune D, He J, Lindsay S, Gorman CB, Tao NJ (2006) Chem Phys 326:138
169. Li XL, Hihath J, Chen F, Masuda T, Zang L, Tao NJ (2007) J Am Chem Soc 129:11535
170. Li C, Mishchenko A, Li Z, Pobelov I, Wandlowski T, Li XQ, Wurthner F, Bagrets A, Evers F (2008) J Phys Condens Matter 20:374122
171. Morita T, Lindsay S (2008) J Phys Chem B 112:10563
172. Alessandrini A, Salerno M, Frabboni S, Facci P (2005) Appl Phys Lett 86:133902
173. Alessandrini A, Corni S, Facci P (2006) Phys Chem Chem Phys 8:4383
174. Chi QJ, Zhang JD, Jensen PS, Christensen HEM, Ulstrup J (2006) Faraday Discuss 131:181
175. Petrangolini P, Alessandrini A, Berti L, Facci P (2010) J Am Chem Soc 132:7445
176. Landauer R (1957) IBM J Res Dev 1:223
177. Imry Y (1986) Physics of mesoscopic systems. In: Grinstein G, Mazenko G (ed) Directions in condensed matter physics. World Scientific, Singapore
178. Scheer E, Joyez P, Esteve D, Urbina C, Devoret MH (1997) Phys Rev Lett 78:3535
179. Cuevas JC, Yeyati AL, Martin-Rodero A (1998) Phys Rev Lett 80:1066
180. Scheer E, Agrait N, Cuevas JC, Yeyati AL, Ludoph B, Martin-Rodero A, Bollinger GR, van Ruitenbeek JM, Urbina C (1998) Nature 394:154
181. Krans JM, Muller CJ, Yanson IK, Govaert TCM, Hesper R, Vanruitenbeek JM (1993) Phys Rev B 48:14721
182. Li CZ, Tao NJ (1998) Appl Phys Lett 72:894
183. Krans JM, Vanruitenbeek JM, Fisun VV, Yanson IK, Dejongh LJ (1995) Nature 375:767
184. Yanson AI, vanRuitenbeek JM (1997) Phys Rev Lett 79:2157
185. Sirvent C, Rodrigo JG, Vieira S, Jurczyszyn L, Mingo N, Flores F (1996) Phys Rev B 53:16086
186. Smit RHM, Untiedt C, Yanson AI, van Ruitenbeek JM (2001) Phys Rev Lett 87:266102
187. Calvo MR, Fernandez-Rossier J, Palacios JJ, Jacob D, Natelson D, Untiedt C (2009) Nature 458:1150
188. Rubio G, Agrait N, Vieira S (1996) Phys Rev Lett 76:2302
189. Rubio-Bollinger G, Bahn SR, Agrait N, Jacobsen KW, Vieira S (2001) Phys Rev Lett 87:026101
190. Torres JA, Saenz JJ (1996) Phys Rev Lett 77:2245
191. Sanchez-Portal D, Artacho E, Junquera J, Ordejon P, Garcia A, Soler JM (1999) Phys Rev Lett 83:3884

192. Huisman EH, Trouwborst ML, Bakker FL, de Boer B, van Wees BJ, van der Molen SJ (2008) Nano Lett 8:3381
193. Smit RHM, Noat Y, Untiedt C, Lang ND, van Hemert MC, van Ruitenbeek JM (2002) Nature 419:906
194. Csonka S, Halbritter A, Mihaly G (2006) Phys Rev B 73:075405
195. Csonka S, Halbritter A, Mihaly G, Shklyarevskii OI, Speller S, van Kempen H (2004) Phys Rev Lett 93:016802
196. Kiguchi M, Stadler R, Kristensen IS, Djukic D, van Ruitenbeek JM (2007) Phys Rev Lett 98:146802
197. Novaes FD, da Silva AJR, da Silva EZ, Fazzio A (2006) Phys Rev Lett 96:016104
198. Thijssen WHA, Marjenburgh D, Bremmer RH, van Ruitenbeek JM (2006) Phys Rev Lett 96:026806
199. Kiguchi M, Djukic D, van Ruitenbeek JM (2007) Nanotechnology 18:035205
200. Tal O, Krieger M, Leerink B, van Ruitenbeek JM (2008) Phys Rev Lett 100:196804
201. Li CZ, Sha H, Tao NJ (1998) Phys Rev B 58:6775
202. He HX, Tao NJ (2002) Adv Mater 14:161
203. Xu BQ, He HX, Tao NJ (2002) J Am Chem Soc 124:13568
204. Jelinek P, Perez R, Ortega J, Flores F (2006) Phys Rev Lett 96:046803
205. Shu C, Li CZ, He HX, Bogozi A, Bunch JS, Tao NJ (2000) Phys Rev Lett 84:5196
206. Xu BQ, He HX, Boussaad S, Tao NJ (2003) Electrochim Acta 48:3085
207. Kiguchi M, Konishi T, Miura S, Murakoshi K (2007) Nanotechnology 18:424011
208. Zhou XS, Wei YM, Liu L, Chen ZB, Tang J, Mao BW (2008) J Am Chem Soc 130:13228
209. Li C, Wandlowswki Th (2011), Electrochim. Acta, in preparation
210. Li C, Wandlowski Th (2011) Small, in preparation
211. Dakkouri A, Kolb DM (1999) Reconstruction of gold surface. In: Wieckowski A (ed) Interfacial electrochemistry: theory, experiment and application. Marcel Dekker, New York
212. Kolb DM, Schneider J (1986) Electrochim Acta 31:929
213. Dretschkow T, Wandlowski T (1997) Ber Der Bunsenges Phys Chem Chem Phys 101:749
214. Wandlowski T, Ataka K, Pronkin S, Diesing D (2004) Electrochimica Acta 49:1233
215. He HX, Shu C, Li CZ, Tao NJ (2002) J Electroanal Chem 522:26
216. Abellan J, Chicon R, Arenas A (1998) Surf Sci 418:493
217. Barnett RN, Hakkinen H, Scherbakov AG, Landman U (2004) Nano Lett 4:1845
218. Okamoto M, Takayanagi K (1999) Phys Rev B 60:7808
219. De Maria L, Springborg M (2000) Chem Phys Lett 323:293
220. Hakkinen H, Barnett RN, Landman U (1999) J Phys Chem B 103:8814
221. Lang G, Heusler KE (1995) J Electroanal Chem 391:169
222. Clausen-Schaumann H, Seitz M, Krautbauer R, Gaub HE (2000) Curr Opinion Chem Bio 4:524
223. Janshoff A, Neitzert M, Oberdorfer Y, Fuchs H (2000) Angew Chem Int Ed 39:3213
224. Hugel T, Seitz M (2001) Macromol Rapid Comm 22:989
225. Rief M, Grubmuller H (2002) ChemPhysChem 3:255
226. Engel A, Gaub HE (2008) Ann Rev Biochem 77:127
227. Huang ZF, Chen F, Bennett PA, Tao NJ (2007) J Am Chem Soc 129:13225
228. Huang ZF, Xu BQ, Chen YC, Di Ventra M, Tao NJ (2006) Nano Lett 6:1240
229. Evans E (1998) Faraday Discuss 111:1
230. Evans E (2001) Annu Rev Biophys Biomol Struct 30:105
231. Tsutsui M, Shoji K, Taniguchi M, Kawai T (2008) Nano Lett 8:345
232. Velez P, Dassie SA, Leiva EPM (2008) Chem Phys Lett 460:261
233. Zhao JW, Murakoshi K, Yin X, Kiguchi M, Guo Y, Wang N, Liang S, Liu H (2008) J Phys Chem C 112:20088
234. Lipkowski J, Shi ZC, Chen AC, Pettinger B, Bilger C (1998) Electrochim Acta 43:2875
235. Magnussen OM (2002) Chem Rev 102:679
236. Pascual JI, Mendez J, Gomezherrero J, Baro AM, Garcia N, Landman U, Luedtke WD, Bogachek EN, Cheng HP (1995) Science 267:1793

237. Untiedt C, Bollinger GR, Vieira S, Agrait N (2000) Phys Rev B 62:9962
238. Garcia-Mochales P, Serena PA, Garcia N, CostaKramer JL (1996) Phys Rev B 53:10268
239. Garcia-Mochales P, Serena PA (1997) Phys Rev Lett 79:2316
240. Cuevas JC, Yeyati AL, Martin-Rodero A, Bollinger GR, Untiedt C, Agrait N (1998) Phys Rev Lett 81:2990
241. Mann B, Kuhn H (1971) J Appl Phys 42:4398
242. Li XL, He J, Hihath J, Xu BQ, Lindsay SM, Tao NJ (2006) J Am Chem Soc 128:2135
243. Haiss W, Nichols RJ, van Zalinge H, Higgins SJ, Bethell D, Schiffrin DJ (2004) Phys Chem Chem Phys 6:4330
244. Haiss W, van Zalinge H, Bethell D, Ulstrup J, Schiffrin DJ, Nichols RJ (2006) Faraday Discuss 131:253
245. Haiss W, Martin S, Leary E, van Zalinge H, Higgins SJ, Bouffier L, Nichols RJ (2009) J Phys Chem C 113:5823
246. Cui XD, Primak A, Zarate X, Tomfohr J, Sankey OF, Moore AL, Moore TA, Gust D, Nagahara LA, Lindsay SM (2002) J Phys Chem B 106:8609
247. Cui XD, Zarate X, Tomfohr J, Sankey OF, Primak A, Moore AL, Moore TA, Gust D, Harris G, Lindsay SM (2002) Nanotechnology 13:5
248. Beebe JM, Engelkes VB, Miller LL, Frisbie CD (2002) J Am Chem Soc 124:11268
249. Engelkes VB, Beebe JM, Frisbie CD (2004) J Am Chem Soc 126:14287
250. Zhou JF, Chen F, Xu BQ (2009) J Am Chem Soc 131:10439
251. Scaini D, Castronovo M, Casalis L, Scoles G (2008) ACS Nano 2:507
252. Gonzalez MT, Brunner J, Huber R, Wu SM, Schonenberger C, Calame M (2008) New J Phys 10:065018
253. Martin CA, Ding D, van der Zant HSJ, van Ruitenbeek JM (2008) New J Phys 10:065008
254. York RL, Nguyen PT, Slowinski K (2003) J Am Chem Soc 125:5948
255. Weiss EA, Chiechi RC, Kaufman GK, Kriebel JK, Li ZF, Duati M, Rampi MA, Whitesides GM (2007) J Am Chem Soc 129:4336
256. Lee T, Wang WY, Klemic JF, Zhang JJ, Su J, Reed MA (2004) J Phys Chem B 108:8742
257. Kushmerick JG, Holt DB, Pollack SK, Ratner MA, Yang JC, Schull TL, Naciri J, Moore MH, Shashidhar R (2002) J Am Chem Soc 124:10654
258. Beebe JM, Kim B, Frisbie CD, Kushmerick JG (2008) ACS Nano 2:827
259. Huisman EH, Guedon CM, van Wees BJ, van der Molen SJ (2009) Nano Lett 9:3909
260. Xia JL, Diez-Perez I, Tao NJ (2008) Nano Lett 8:1960
261. Hihath J, Arroyo CR, Rubio-Bollinger G, Tao NJ, Agrait N (2008) Nano Lett 8:1673
262. Wang WY, Lee T, Reed MA (2003) Phys Rev B 68:035416
263. Holmlin RE, Haag R, Chabinyc ML, Ismagilov RF, Cohen AE, Terfort A, Rampi MA, Whitesides GM (2001) J Am Chem Soc 123:5075
264. Slowinski K, Chamberlain RV, Miller CJ, Majda M (1997) J Am Chem Soc 119:11910
265. Chidsey CED (1991) Science 251:919
266. Smalley JF, Feldberg SW, Chidsey CED, Linford MR, Newton MD, Liu YP (1995) J Phys Chem 99:13141
267. Arnold A, Weigend F, Evers F (2007) J Chem Phys 126:174101
268. Im HS, Bernstein ER (1988) J Chem Phys 88:7337
269. Ando S, Hironaka T, Kurosu H, Ando I (2000) Magn Reson Chem 38:241
270. Wang J, Cooper G, Tulumello D, Hitchcock AP (2005) J Phys Chem A 109:10886
271. Pauly F, Viljas JK, Cuevas JC, Schon G (2008) Phys Rev B 77:155312
272. Kondo H, Nara J, Kino H, Ohno T (2008) J Chem Phys 128:064701
273. Benniston AC, Harriman A, Li P, Patel PV, Sams CA (2008) Chem Eur J 14:1710
274. Smalley JF, Sachs SB, Chidsey CED, Dudek SP, Sikes HD, Creager SE, Yu CJ, Feldberg SW, Newton MD (2004) J Am Chem Soc 126:14620
275. Lee MH, Speyer G, Sankey OF (2007) J Phys Condens Matter 19:215204
276. Tomfohr J, Sankey OF (2004) J Chem Phys 120:1542
277. Finch CM, Sirichantaropass S, Bailey SW, Grace IM, Garcia-Suarez VM, Lambert CJ (2008) J Phys Condens Matter 20:022203

278. Zotti LA, Kirchner T, Cuevas JC, Pauly F, Huhn T, Scheer E, Erbe A (2010) Small 6:1529
279. Vonlanthen D, Rotzler J, Neuburger M, Mayor M (2010) Eur J Org Chem 1:120
280. Rotzler J, Vonlanthen D, Barsella A, Boeglin A, Fort A, Mayor M (2010) Eur J Org Chem 6:1096
281. Pauly F, Viljas JK, Cuevas JC (2008) Phys Rev B 78:035315
282. Perdew JP (1986) Phys Rev B 33:8822
283. Ahlrichs R, Bar M, Haser M, Horn H, Kolmel C (1989) Chem Phys Lett 162:165
284. Eichkorn K, Treutler O, Ohm H, Haser M, Ahlrichs R (1995) Chem Phys Lett 242:652
285. Pauly F, Viljas JK, Huniar U, Hafner M, Wohlthat S, Burkle M, Cuevas JC, Schon G (2008) New J Phys 10:125019
286. Schmitteckert P, Evers F (2008) Phys Rev Lett 100:086401
287. Vonlathen D, Rudnev A, Mishchenko A, Käslin A, Rotzler J, Neuburger M, Wandlowski Th, Mayor M (2011) Europ J Chem. 17:7236–7250 doi:10.1002/chem.201003763
288. Xue YQ, Ratner MA (2004) Phys Rev B 69:085403
289. Baheti K, Malen JA, Doak P, Reddy P, Jang SY, Tilley TD, Majumdar A, Segalman RA (2008) Nano Lett 8:715
290. Li C, Manrique DZ, Lambert CJ, Wandlowski Th (2011) ACS Nano, in preparation 2011
291. Steel PJ (1990) Coordin Chem Rev 106:227
292. Stang PJ, Olenyub B (2000) In: Nalwa HS (ed) Handbook of nanostructured materials, vol 15. New York, Academic Press
293. Boag NM, Coward KM, Jones AC, Pemble ME, Thompson JR (1999) Acta Cryst Sec C 55:672
294. Almennigen A, Bastiansen O (1958) K Nor Vidensk Selesk Skr 4:1
295. Spotswood T, Tanzer CI (1967) Austr J Chem 20:1227
296. Manutova YS, Maltseva LS, Kamaaev FG, Leontév B, Mikhamedkhanova S, Otroshchenko OS, Sadykov AS (1973) Izv Akad Nauk SSSR Ser Khim 7:1510
297. Ould-Moussa L, Poizat O, Castella-Ventura M, Buntinx G, Kassab E (1996) J Phys Chem 100:2072
298. Bagrets A, Arnold A, Evers F (2008) J Am Chem Soc 130:9013
299. Quek SY, Kamenetska M, Steigerwald ML, Choi HJ, Louie SG, Hybertsen MS, Neaton JB, Venkataraman L (2009) Nat Nanotechnol 4:230
300. Li XL, Xu BQ, Xiao XY, Yang XM, Zang L, Tao NJ (2006) Faraday Discuss 131:111
301. Zhou XS, Chen ZB, Liu SH, Jin S, Liu L, Zhang HM, Xie ZX, Jiang YB, Mao BW (2008) J Phys Chem C 112:3935
302. Leary E, Hobenreich H, Higgins SJ, van Zalinge H, Haiss W, Nichols RJ, Finch CM, Grace I, Lambert CJ, McGrath R, Smerdon J (2009) Phys Rev Lett 102:086801
303. Wandlowski T, Ataka K, Mayer D (2002) Langmuir 18:4331
304. Mayer D, Dretschkow T, Ataka K, Wandlowski T (2002) J Electroanal Chem 524:20
305. Wang X, Liu Z, Zhuang MD, Zhang HM, Xie ZX, Wu DY, Ren B, Tian ZQ (2007) Appl Phys Lett 91:101105
306. Liu Z, Wang X, Dai K, Jin S, Zeng ZC, Zhuang MD, Yang ZL, Wu DY, Ren B, Tian ZQ (2009) J Raman Spectrosc 40:1400
307. Yanson AI, Bollinger GR, van den Brom HE, Agrait N, van Ruitenbeek JM (1998) Nature 395:783
308. Trouwborst ML, Huisman EH, Bakker FL, van der Molen SJ, van Wees BJ (2008) Phys Rev Lett 100:175502
309. Stadler R, Thygesen KS, Jacobsen KW (2005) Phys Rev B 72:241401
310. Futamata M (2001) J Phys Chem B 105:6933
311. Corni S (2007) IEEE Trans Nanotechnol 6:561
312. Wurthner F (2004) Chem Commun 14:1564
313. Grimsdale AC, Mullen K (2005) Angew Chem Int Ed 44:5592
314. Ranke P, Bleyl I, Simmerer J, Haarer D, Bacher A, Schmidt HW (1997) Appl Phys Lett 71:1332

315. Ego C, Marsitzky D, Becker S, Zhang JY, Grimsdale AC, Mullen K, MacKenzie JD, Silva C, Friend RH (2003) J Am Chem Soc 125:437
316. Horowitz G, Kouki F, Spearman P, Fichou D, Nogues C, Pan X, Garnier F (1996) Adv Mater 8:242
317. Briseno AL, Mannsfeld SCB, Reese C, Hancock JM, Xiong Y, Jenekhe SA, Bao Z, Xia Y (2007) Nano Lett 7:2847
318. Tamizhmani G, Dodelet JP, Cote R, Gravel D (1991) Chem Mater 3:1046
319. Schmidt-Mende L, Fechtenkotter A, Mullen K, Moons E, Friend RH, MacKenzie JD (2001) Science 293:1119
320. Goltner C, Pressner D, Mullen K, Spiess HW (1993) Angew Chem Int Ed 32:1660
321. Sauer M (2003) Angew Chem Int Ed 42:1790
322. Wilson TM, Tauber MJ, Wasielewski MR (2009) J Am Chem Soc 131:8952
323. Osswald P, Wurthner F (2007) J Am Chem Soc 129:14319
324. Salbeck J, Kunkely H, Langhals H, Saalfrank RW, Daub J (1989) Chimia 43:6
325. Su W, Jiang J, Lu W, Luo Y (2006) Nano Lett 6:2091
326. Cao H, Jiang J, Ma J, Luo Y (2008) J Am Chem Soc 130:6674
327. Wurthner F, Sautter A, Schmid D, Weber PJA (2001) Chem Eur J 7:894
328. Wurthner F, Stepanenko V, Chen ZJ, Saha-Moller CR, Kocher N, Stalke D (2004) J Org Chem 69:7933
329. Baggerman J, Jagesar DC, Vallee RAL, Hofkens J, De Schryver FC, Schelhase F, Vogtle F, Brouwer AM (2007) Chem Eur J 13:1291
330. Chen ZJ, Baumeister U, Tschierske C, Wurthner F (2007) Chem Eur J 13:450
331. Taylor J, Brandbyge M, Stokbro K (2003) Phys Rev B 68:121101
332. Mowbray DJ, Jones G, Thygesen KS (2008) J Chem Phys 128:111103
333. Palma JL, Cao C, Zhang XG, Krstic PS, Krause JL, Cheng HP (2010) J Phys Chem C 114:1655
334. Mertens SFL, Blech K, Sologubenko AS, Mayer J, Simon U, Wandlowski T (2009) Electrochim Acta 54:5006
335. Mertens SFL, Meszaros G, Wandlowski T (2010) Phys Chem Chem Phys 12:5417
336. Murray RW (2008) Chem Rev 108:2688
337. Laaksonen T, Ruiz V, Liljeroth P, Quinn BM (2008) Chem Soc Rev 37:1836
338. Grabert H, Devoret MH (1972) Single electron tunneling. Plenum, New York
339. Chen SW, Murray RW, Feldberg SW (1998) J Phys Chem B 102:9898
340. Chen SW, Murray RW (1999) J Phys Chem B 103:9996
341. Chen SW, Ingram RS, Hostetler MJ, Pietron JJ, Murray RW, Schaaff TG, Khoury JT, Alvarez MM, Whetten RL (1998) Science 280:2098
342. Ingram RS, Hostetler MJ, Murray RW, Schaaff TG, Khoury JT, Whetten RL, Bigioni TP, Guthrie DK, First PN (1997) J Am Chem Soc 119:9279
343. Quinn BM, Liljeroth P, Ruiz V, Laaksonen T, Kontturi K (2003) J Am Chem Soc 125:6644
344. Templeton AC, Wuelfing MP, Murray RW (2000) Acc Chem Res 33:27
345. Hicks JF, Miles DT, Murray RW (2002) J Am Chem Soc 124:13322
346. Pietron JJ, Hicks JF, Murray RW (1999) J Am Chem Soc 121:5565
347. Zabet-Khosousi A, Dhirani AA (2008) Chem Rev 108:4072
348. Hicks JF, Templeton AC, Chen SW, Sheran KM, Jasti R, Murray RW, Debord J, Schaaf TG, Whetten RL (1999) Anal Chem 71:3703
349. Su B, Zhang MQ, Shao YH, Girault HH (2006) J Phys Chem B 110:21460
350. Chen SW (2000) J Phys Chem B 104:663
351. Deng FJ, Chen SW (2005) Phys Chem Chem Phys 7:3375
352. Aguila A, Murray RW (2000) Langmuir 16:5949
353. Dubois JGA, Gerritsen JW, Schmid G, van Kempen H (1996) Physica B 218:262
354. Nijhuis CA, Oncel N, Huskens J, Zandvliet HJW, Ravoo BJ, Poelsema B, Reinhoudt DN (2006) Small 2:1422
355. Homberger M, Simon U (2010) Philos Trans R Soc A 368:1405